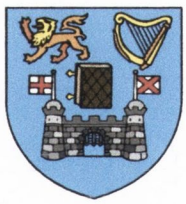

Polymer Crystallisation as a Reinforcement Mechanism for Polymer-Carbon Nanotube Composites.

By

Kevin Ryan

A thesis submitted for the degree of

Doctor of Philosophy

at the

University of Dublin

Department of Physics,

Trinity College Dublin.

2005

Declaration

I declare that the work in this dissertation has not been previously submitted as an exercise for a degree to this or any other university.

The work described herein is entirely my own work, except for the assistance mentioned in the acknowledgements and the collaborative work mentioned in the list of publications.

I agree that Trinity College Library may lend or copy this thesis on request.

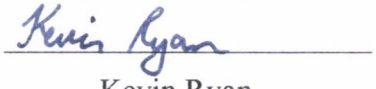

Kevin Ryan

"It is a capital mistake to theorise before one has data. Insensibly one begins to twist facts to suit theories, instead of theories to suit facts."

(Sir Arthur Conan Doyle)

"There is nothing, Sir, too little for so little a creature as man. It is by studying the little things that we attain the great art of having as little misery and as much happiness as possible"

(Samuel Johnson)

"It is a cursed evil to any man to become absorbed in any subject as I am in mine"

(Charles Darwin)

Acknowledgements

As Prof. Werner Blau's group celebrated 21 years of research in September 2004, it is fitting to acknowledge that many of the group, past and present, have contributed ideas and shared their expertise to support my work. I would like to thank Prof. Blau for the financial support and opportunities to travel during the past few years – these have been invaluable experiences. I would also like to thank my supervisor Dr. Jonathan Coleman for excellent direction of the research project and his time for discussions and ideas even when the queue of visitors stretched beyond his office door.

The help of Dr. Leslie Carpenter, Dr. Stephen Lipson and Adam Strevens was invaluable for structuring and correcting the early stages of this thesis. Thanks to Dr. Martin Cadek for passing on his knowledge of PVOH/Carbon nanotube research and always making himself available to answer questions. David Blond and Sonya Walker also contributed time to develop the PVOH project while Rowan Blake shared his valuable chemistry expertise.

Thanks to Dr. Manuel Rüther who so willingly shared his extensive knowledge of thermal analysis experiments, Dr. Valerie Barron for help in the initial stages of the crystallisation experiments and Anna Drury who kindly synthesised the PmPV material. Dr. Stefanie Maier provided important information on synthesis routes for PmPV.

Dr. Andrew Minett carried out preliminary AFM microscopy while Valeria Nicolosi took the essential TEM and SEM images that appear throughout the thesis. Thanks to Rory Leahy for annealing nanotubes with his CVD system and Dr. Gordon Armstrong for his time and expertise during the XRD studies.

Thanks to Rakel Sainz, Dr. W.K. Maser and Dr. Silvia Giordani for collaborative work on PANI/MWNT composites, Roberto Massa for Hyperchem Modelling, Dr. Sean O' Flaherty and Rob Murphy for help on the PmPV/MWNT composite experiments. Dr. Hugh Byrne of the Focas group at DIT Kevin St. arranged unlimited use of a DSC machine prior to the arrival of our own. Liam Brennan at NUI Galway provided technical support for the tensile measurements. Jeanette Cummins deserves a special mention for sorting out the mountain of administrative paperwork whenever necessary. Mick, Dave, John, Jemmer, Michelle, Susan, Ken and Joe are all acknowledged for their prompt technical support whenever they were called upon.

Last, but not least, thanks to all members of Group BU and Materials Ireland for their patience, humour, science and energy that have made the last three and a half years an education in life.

Table of Contents

List of Tables

List of Figures and Illustrations

Abstract

Two semi-crystalline polymers, poly(m-phenylenevinylene-co-2,5-dioctyloxy-p-phenylenevinylene) (PmPV) and poly(vinyl alcohol) (PVOH), have been doped with carbon nanotubes. In the case of PmPV, well-graphitised arc discharge multi-walled nanotubes were used as the filler material. While attempts to detect the changes in polymer morphology using X-Ray diffraction had limited success, dynamic differential scanning calorimetry of thin films has verified a 35 % increase in polymer crystallinity with the addition of 3 vol% of arc produced multiwalled carbon nanotubes. A basic model of the system fitted to the crystallinity data yielded a thickness of 23 nm for the crystalline region adjacent to the nanotube. Furthermore, photoluminescence measurements have shown that the photoluminescence quantum yield in the composites decreases with increasing nanotube content. The crystallinity model was further developed to assume a decrease in polymer photoluminescence as distance from the nanotube surface decreases with total extinction at the polymer/nanotube interface. A coating thickness of 32 nm was calculated from the fit in reasonable agreement with the values calculated by calorimetry (23 nm) and TEM (25 nm). FTIR data is used to provide additional evidence for nanotube-induced alteration of polymer conformation.

Poly (vinyl alcohol) was subsequently doped with nanotubes of various diameters produced using both the arc and chemical vapour deposition techniques. 120 W sonic energy over a period of 15 min was found to break carbon nanotubes to lengths of approximately 1 μm. Nanotube isolation and diameter were found to be more important than nanotube length for effective reinforcement. Thus, composites with low nanotube concentrations were found to have the best mechanical properties. Furthermore, the samples that exhibit the most impressive increase in Young's modulus and tensile strength values are also the most crystalline. As in the case of PmPV, crystallinity data was consistent with a crystalline coating at the PVOH/nanotube interface. Analysis showed that the thickness of the crystalline layer increases as a function of nanotube diameter.

CHAPTER ONE: INTRODUCTION

1.1 A demand for innovation

Materials science has been a subject of intense interest for thousands of years. Evidence shows that in 3750 BC the Egyptians and Sumerians used charcoal for the reduction of copper, zinc and tin ores in the manufacture of bronze. The primary driving forces behind materials research today are identical to those of thousands of years ago as we strive for stronger, tougher lighter and efficient materials that aim to raise the comfort level of life in general, all at the lowest possible price. Wood and clay have been replaced by materials such as steel and concrete, both of which are composites. It is in this context that the research presented here has been undertaken to investigate carbon nanotube reinforced plastics as candidates for the next generation of materials.

The development of these future materials, and subsequent incorporation into devices, is a continuous process and the current changeover to flat panel displays is a prime example of advances in science and engineering. Active research on conductive and luminescent conjugated polymers has yielded efficient, cheap displays based on organic materials while the incorporation of carbon nanotubes into non-conjugated materials is producing new composites with significantly improved mechanical[1,2,3,4] and electrical properties[5,6]. The progress of organic composites, with particular emphasis on recent years, will be discussed in later chapters to relate the project aims to that of similar research groups in the carbon nanotube field. More importantly, actual device applications will be identified along with the more speculative applications of the future.

It is not difficult to list the industries that would economically benefit from lighter, stronger materials – NASA Ames Research Center for Nanotechnology in Moffett Field, CA. strives to produce efficient spacecraft. The multi-billion dollar plastic industry provides a huge market for functional fillers – strength and conductivity are two of the primary goals for an automotive industry that constantly seeks innovative materials that can cut cost and increase efficiency on the production line and on the road. The global automotive cockpit market alone was valued at $16.7 billion for 2003[7] while the automotive composites market was reported at $384.3 Million for 2002[8]. It will be shown that carbon nanotubes are proven fillers and therefore any commercially viable application in the plastics industry has huge market potential given the volumes produced

annually. Production techniques such as injection moulding are rate limited by the speed of polymer curing. For this reason nucleating agents are constantly sought to accelerate the process[9]. This thesis will present the science behind proposals suggesting there is a bright future for carbon nanotube composites as the next generation of high performance materials[10].

1.2 Discovery of Carbon Nanotubes

The discovery of carbon nanotubes is attributed to Iijima after the use of Transmission Electron Microscopy (TEM) to image arc discharge produced carbonaceous material at NEC Japan in 1991[11]. However, the work of Endo in 1975[12] and Hyperion Catalysis International in 1983 had produced similar structures but the significance of these carbon structures was not realised until after the Iijima paper. The first nanotubes were multi-walled nanotubes (MWNT) consisting of several concentric carbon tubes nested inside each other. Iijima was also the first to isolate single wall nanotubes (SWNT) with a diameter of just 1-2nm in 1993[13]. Since then theoretical modelling in conjunction with mechanical and electrical characterisation experiments have shown great potential and unique properties of carbon nanotubes as outlined in a review by Baughman et al[14]. Yet while they can be great conductors of heat and electricity, and are one of the strongest materials known, they still have few commercial applications due to the problem of processability. The cost of large-scale high quality nanotube production must also be reduced before many of the commercial applications can be realised. At present, many nanotube producers offer industrial and research grades of their material. Industrial grades are often un-purified bulk quantities that cost approximately $6 per gram[15] and can be used as a filler material to achieve an increase in host conductivity. Research grade material is significantly more expensive and price varies with the diameter of nanotube required. Purified SWNT produced by the company CNI via the high-pressure decomposition of carbon monoxide (HiPco) were advertised on the company website at $500 per gram in August 2005. Research grades of larger diameter MWNT can be purchased for less than $50 per gram from the companies Carbolex and Nanocyl via their websites. Recent improvement in production techniques has ensured a significant drop in nanotube production costs – of course there is always a quality/quantity trade-off in these situations. Fortunately, low-grade material can be sufficient for most conductivity enhancement applications, examples of which will be outlined in the next section.

1.3 Applications in production/prototype phase

Products already on the market include carbon nanotube-filled plastics that are being used in several commercial automotive applications in North America, Europe and Japan. One application area is fuel line production where Nylon 12 is frequently the resin of choice because of its chemical resistance to gasoline. Moving fuel can build up a static charge and as a result the fuel line needs to be conductive enough to bleed off the charge. Nanotubes are the preferred additive for this application due to the low loading necessary to achieve increases in conductivity[14]. Electrostatic spray painting is a technique used in the automotive industry with benefits such as minimal wasteful overspray, minimal emissions of solvents and high quality appearance. Unlike steel components that are already conductive and suitable for the technique, plastic components are not. Having a conductive plastic is much preferred to spraying a conductive primer on before the topcoats therefore thermoplastic bumpers are doped with carbon nanotubes which raise their conductivity. Nanotube-filled polycarbonate (PC), polyetherimide (PEI) and polyetheretherketone (PEEK) are also used in the electronic industry for their ability to provide a very smooth, hard, surface to minimise "sloughing" or "rub off" of particles from the surface of a molded part. Conductivity is particularly important in the manufacture of semiconductor chips where the least static discharge can obliterate the small features. Similar concerns regarding static control and sloughing have led to the widespread use of nanotube filled polycarbonate in transport trays, as well as actual components, for the manufacture of computer hard disc drives[16,17].

Some prototype devices using the excellent field emission properties of CNT have been reviewed by Ajayan and Zhou[18]. Carbon nanotubes have the right combination of properties – nanometer size diameter, structural integrity, high electrical conductivity, and chemical stability that make good electron emitters. Electron field emission from carbon nanotubes was first demonstrated in 1995[19], and has since been studied intensively on various carbon nanotube materials. Compared to conventional emitters, carbon nanotubes exhibit a lower threshold electric field[18]. Figure 1-2 shows a prototype field emission light source using carbon nanotubes as the cathode[20]. However, the current-carrying capability and emission stability of the various carbon nanotubes vary considerably depending on the fabrication process and synthesis conditions.

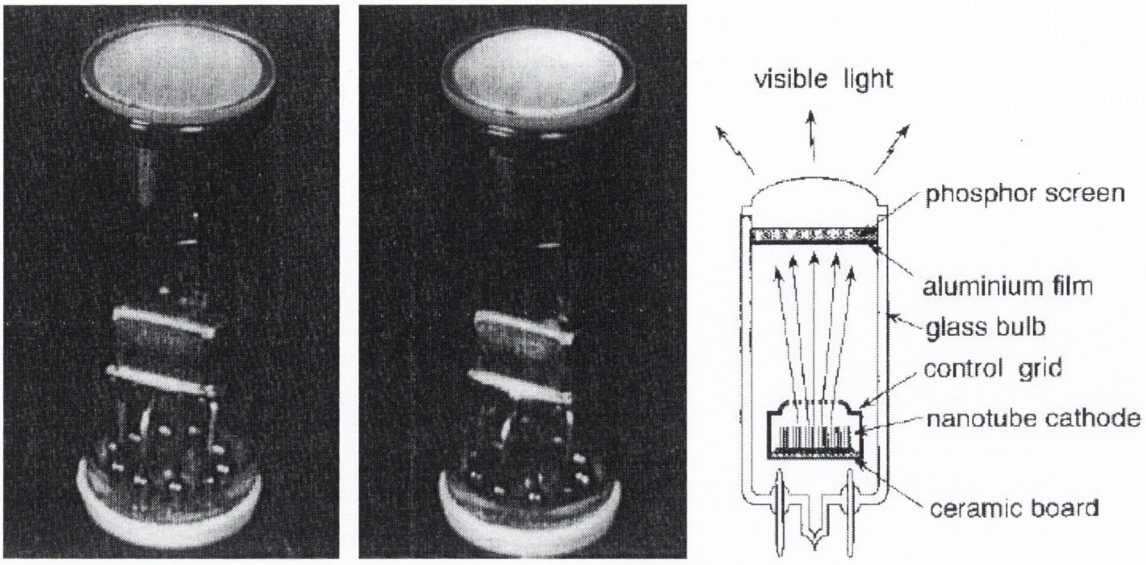

Figure 1-2: *Prototype field emission light source using carbon nanotubes as the cathode.*

Gas discharge tube (GDT) protectors, usually consisting of two electrodes parallel to each other in a sealed ceramic case filled with a mixture of noble gases, is one of the oldest methods used to protect against transient over-voltages in a circuit. They are widely used in telecom network interface device boxes and central office switching equipment to provide protection from lightning and ac power cross faults on the telecom network. Prototype GDT devices using carbon nanotube coated electrodes have recently been fabricated and tested by a group from UNC and Raychem. Molybdenum electrodes with various interlayer materials were coated with single-walled carbon nanotubes and analysed for both electron field emission and discharge properties. A mean dc breakdown voltage of 448.5V and a standard deviation of 4.8V over 100 surges were observed in nanotube-based GDTs with 1 mm gap spacing between the electrodes. The breakdown reliability is a factor of 4–20 better and the breakdown voltage is ~30% lower than the two commercial products measured. The enhanced performance shows that nanotube-based GDTs are attractive over-voltage protection units.

Aside from these existing products, there are many potential applications for CNT including use as efficient electrodes in Lithium batteries, nano-sensors[21], petroleum filters[22] and hydrogen storage[23,24] which remains a contentious issue. The final potential application, and the one that appears to be the closest to the market, is the use of CNT as reinforcing agents. It is these improvements in mechanical properties of polymer matrices that are addressed in the second part of this thesis while the first section focuses on

changes in the optical and thermal properties of a luminescent polymer upon introduction of carbon nanotubes.

1.4 Relevant literature

A great deal of literature has been published, particularly over the last decade, regarding the properties of carbon nanotubes and their composites. The papers regarding the mechanical properties of carbon nanotube/polymer composites will be discussed in detail in the next section and compared to carbon fibre based composite technology which has been utilized in polymer reinforcement applications since the 1940's[25]. In addition, the most impressive and instructive publications regarding carbon nanotube composites have been summarised in table format and are included as Appendix A. This format has been chosen to group publications according to the materials involved facilitating comparison of the performance of one polymer/nanotube combination over another. The year of publication is included to chart the chronological development of the field alongside the experimental techniques used to assess the properties of the material. Publications that have reported wrapping of carbon nanotubes by polymers and proteins are introduced first. Particular emphasis is given to methods identifying this polymer coating. Following this, theoretical papers predicting the strength of carbon nanotubes and their composites are listed before proceeding to the experimental papers reporting mechanical enhancement in carbon nanotube composites. In many cases these papers confirm and complement each other and are grouped accordingly. A number of excellent review papers outlining the properties and applications of carbon nanotubes are also highly recommended[26,27,28,29]. Detailed analysis of relevant papers will accompany the experimental analysis chapters.

1.4.1 Carbon Nano-Fibre and Carbon Nanotubes

In recent times fibres made from materials such as alumina, glass, boron, silicon carbide and especially carbon have been used as fillers in composites. These conventional fibres are typically on the meso-scale with diameters of tens of microns and lengths of order of millimetres. Their mechanical properties are impressive with carbon fibres typically displaying stiffness and strength in the ranges 230-725 GPa and 1.5-4.8 GPa respectively[30,31]. Carbon fibres were originally made by pyrolysis from pitch and polymers[32] but in recent years carbon nano-fibres have been grown from the vapour phase

with diameters of order of 100 nm and lengths between 20 and 100 microns. These small dimensions mean they have much higher surface area per unit mass than conventional carbon fibres allowing much greater interaction with composite matrices. They also tend to have excellent mechanical properties with Young's modulus in the range 100-1000 GPa and strengths between 2.5 and 3.5 GPa[33].

Carbon nanotubes have smaller diameters than carbon nano-fibres ranging from 1-100 nm while lengths can be several millimetres[34]. Their densities can be as low as ~1.3 g/cm^3 and their Young's moduli are superior to all carbon fibres with values greater than 1TPa[35]. However, their strength is what really sets them apart. The highest measured strength for a carbon nanotube was 63 GPa[36]. This is an order of magnitude stronger than high strength carbon fibres. Even the weakest type of carbon nanotubes have strengths of several GPa[37]. In contrast to the solid structure of a carbon nano-fibre, carbon nanotubes are hollow.

The mechanical properties of both nano-fibres and nanotubes can best be utilized by forming composite materials. Polymeric hosts will be discussed here but other matrix materials such as ceramics and concrete have also been successfully reinforced with carbon-nanofibre[38]. The most direct way to compare the performance of carbon nanotubes against nano-fibres is to assess the results reported for polymer matrices doped with each. However, the literature does not present many cases where a comparison of the two filler types is performed by a single researcher using the same matrix polymer. One such experiment was reported by Frogley et al[39] who doped a silicone based elastomer with both SWNT and carbon nano-fibre. The increase in Young's modulus relative to a neat elastomer film was approximately linear with a slope of 200%/wt% and 120%/wt% for the SWNT and nano-fibre composites, respectively. This implies that at a SWNT loading of 1 wt% the composite was three times as stiff as an unfilled matrix film. The nano-fibre composite performs less effectively with stiffness a little over double that of the neat elastomer at a loading of 1 wt%. So in that experiment SWNT performed better than carbon nano-fibre. In both cases the increase in modulus occurs at the expensive of toughness.

A paper by Sandler et al[40], in collaboration with a number of universities including our group at Trinity, measured polyamide-12 (PA-12) fibres doped with carbon nanotubes and nanofibres. The composite fibre doped with 10 wt% of entangled catalytically grown carbon nanotubes exhibited over a 100% increase in tensile modulus, the highest of all the fillers tested. The second best performer was the carbon nanofibre composite followed closely by the aligned catalytically grown carbon nanotube sample. An arc produced carbon nanotube composite exhibited the worst mechanical properties with little increase over those of the pure PA-12 matrix.

Interesting research has been performed on polyamide (PA) – carbon nanotube polymer composites by Gao et al.[41] who reported a chemical processing technology that allows the continuous spinning of SWNTs-nylon 6 (PA6) fibers by the in-situ polymerization of caprolactam in the presence of SWNTs. The process leads to a uniform dispersion of the SWNTs, and the incorporation of 1.5 wt % SWNTs into nylon resulted in an increase of the tensile modulus and strength of about 170% and 90%, respectively. A similar experiment was summarised in a report by the Zoltek carbon fibre company[42] where carbon nanofibre/nylon 6,6 (PA6,6) composites were injection moulded. Note that the polymer matrix is the longer monomer nylon so that the comparison is not identical but the matrix properties are almost the same[42]. The tensile strength was found to increase 222% at a loading of 50 wt% relative to the neat polymer sample. This implies the carbon nano-fibre composite performance is marginally better than the nanotube composite. In another work[43] polyamide 6 (PA6)/MWNTs composites have been prepared by in situ polymerization of epsilon-caprolactam in the presence of pristine and carboxylated MWNTs. Compared with pure PA6, the yield strength of PA6/CNTs composites loaded with 0.5 wt% CNTs is almost unchanged, and the tensile strength is increased slightly. However, dynamic mechanical analysis (DMA) demonstrates that both the storage modulus (E') and glass transition temperature (T-g) of the PA6/CNTs composites increase, particularly for carboxylated MWNTs, indicating there is some chemical bonding between PA6 and MWNTs. Park et al[44] reported synthesis of SWNT reinforced polyimide nanocomposites by in situ polymerization of diamine and dianhydride using sonication. This process enabled uniform dispersion of SWNT bundles in the polymer matrix. Dynamic mechanical tests showed that Young modulus gradually increased with increasing nanotube concentration reaching up to a 60% increase at 1.0 vol% SWNT loading level.

Given the limited number of experiments that directly compare the performance of carbon nanotubes against nano-fibres, it is useful to compare experiments where the same matrix has been independently filled with either of the two species. Of course the myriad of processing techniques used by researchers to form composites will influence the mechanical properties of the composite to varying degrees so these comparisons should be considered only as a rough guide to filler performance. Polypropylene (PP) is one of the polymers that features often in the literature. Kumar et al[45] found that 5 wt% of carbon nano-fibres added to a PP matrix produced a 54% increase in Young's modulus, 92% increase in compressive strength and 16% increase in tensile strength relative to a neat polymer film. This result compares well to that of Lozano et al[46] where a 60% increase was observed in the room temperature storage modulus of a PP film doped with 2 wt% of 100 nm diameter carbon fibres. Similar experiments were carried out by Grady et al[47] using carbon nanotubes as the filler material. They doped a PP film with 1.8 wt% of SWNT but only observed a 15% increase in the storage modulus. In contrast to the Frogley experiment introduced above, SWNT appear here to be less effective reinforcing elements relative to carbon fibre. Given the theoretical advantages in stiffness that nanotubes possess over nano-fibre it is most likely that filler dispersion is the limiting factor in this case. Nanotube dispersion is difficult to achieve, even in solution processing, so that conventional injection moulding techniques used to form composites are often unsuitable to produce well-mixed materials thus limiting the efficacy of the filler. Solution processing will be discussed in detail throughout this thesis since this method must be mastered prior to developing the other and often more difficult techniques for mixing composites.

Several papers have been published on in situ polymerization synthesis of poly (methyl methacrylate) (PMMA) – nanotube composites. For instance, Jia et al[48] prepared of MWNT - PMMA composites by an in situ polymerization process using radical initiator 2,2′-azobisisobutyronitrile (AIBN). Authors believe that pi-bonds in carbon nanotubes can be initiated by AIBN and therefore nanotubes may participate in PMMA polymerization to form a strong interface between the MWNTs and the PMMA matrix. The mechanical properties and the heat deflection temperatures of composites improved reasonably with the increase of nanotubes content. For example, for composites with 5 wt% nanotube content tensile strength increased by ~ 30 %, toughness by ~ 11 % and hardness by ~ 42% compared to pure PMMA samples. However, when the amount of

nanotubes in composites exceeded 7 wt.%, the mechanical properties of the composites decreased due to the residual stress in the polymer matrix. Authors also noticed that when nanotube content reached 10 wt.%, the composite became very brittle.

Putz et al.[49] reported dynamic mechanical analysis of pure PMMA and on in situ polymerized SWNT - PMMA composites. The addition of less than 0.1 wt % SWNT to PMMA led to an increase in the low-temperature elastic modulus of approximately 10% beyond that of pure PMMA. Velasco-Santos[50] et al have incorporated carboxyl functionalized MWNTs into PMMA matrix by in situ polymerization to improve the transfer of mechanical load through a chemical bond. The resulting composite with only 1wt % of functionalized MWNTs demonstrated 66% increase in storage modulus at 40 °C as compared to 50% in the composite with unfunctionalized -MWNTs; all increases were measured with respect to the pristine PMMA polymer. In addition, storage modulus for functionalized MWNT composites increases by an astonishing factor of 11-fold at 90 °C and the glass transition temperature is raised by congruent to 40 °C. These composites also showed much higher plasticity than unfunctionalised -MWNT composites in stress-strain curves.

Finally, Kumar et al.[51] have synthesized new ultra-strong poly(*p*-phenylene benzobisoxazole) (PBO) composites in the presence of single-wall carbon nanotubes (SWNTs) in poly(phosphoric acid) (PPA) by in situ PBO polymerization. The tensile strength of the PBO/SWNT fiber containing 10 wt % SWNTs was found to be 4.2 GPa which is about 50% higher than that of the control PBO fibers without nanotubes. Given the exceptional performance of carbon fibre based composites the increase in tensile strength of 50% achieved for the PBO/SWNT fibres is the order of magnitude required to make carbon nanotubes viable contenders for reinforcement applications in place of more conventional fillers such as carbon fibre, nanoclay and glass fibre[40]. The papers outlined in this review have shown that in-situ polymerisation or functionalisation is required to achieve increases in excess of 50% for tensile modulus and strength in carbon nanotube/polymer composites. These approaches have been shown to be two of the best routes to controlling carbon nanotube dispersion thus realising their exceptional mechanical properties. However, an alternative solution based processing method uses semi-crystalline polymers to disperse and crystallise around carbon nanotubes. A stable

solution is formed from which composite films are cast. The challenges and future potential of this technique are the focus of this thesis.

1.5 Thesis Outline

The interaction between carbon nanotubes and semi-crystalline polymers is addressed with view to maximising the properties of both elements of the composites. All of the processing procedures that ultimately influence the characteristics of the composite are investigated. This includes the initial mixing of the raw materials right through to testing and analysis of the free-standing plastic strips. Chapter 2 introduces the raw materials, discusses the inherent properties of carbon nanotubes and explains the choice of polymers. The basic theory and motivation is outlined for each experimental technique used to assess the materials.

Chapter 3 discusses the sample preparation methods including spin-casting, drop-casting and finally the detailed free-standing film preparation that is necessary to eliminate bubble formation. Specific details regarding instrumentation and associated sample configuration will be noted. Environmental issues such as water absorption and thermal annealing are introduced.

Chapter 4 analyses the data obtained for the PmPV/ArcMWNT composites. Thermogravimetric Analysis (TGA) is used to determine the nanotube content before discussing measurement of polymer crystallinity using X-Ray diffraction (XRD) and Differential Scanning Calorimetry (DSC). Since PmPV is a luminescent polymer, Photoluminescence (PL) and Ultra-Violet/Visible (UV-Vis) absorption measurements compliment the crystallinity study in conjunction with Fourier-Transform Infrared Spectroscopy (FTIR). Tensile tests and Dynamic Mechanical and Thermal Analysis (DMTA) results measure a marginal increase in mechanical properties with the presence of nanotubes. Models are fitted to the DSC and PL data suggesting the crystalline domains exist at the polymer/nanotube interface in the form of a circumferential coating in excellent agreement with TEM images of PmPV coated arc produced multi-walled nanotubes.

Chapter 5 studies issues related to the dispersion of carbon nanotubes in PVOH. A study of aggregation as a function of sonic treatment with a tip and bath was performed and analysed using TEM and optical microscopy. An extensive investigation of water absorption by PVOH based composites has also been carried out. A link is established between polymer crystallinity and mechanical performance.

Chapter 6 presents the crystalline and mechanical properties of various carbon nanotube/PVOH composites. As for the PmPV/ArcMWNT samples, XRD and DSC results are presented in conjunction with tensile tests and DMTA. Evidence is presented supporting the theory that polymer crystallisation is the dominant reinforcement mechanism in PVOH/CNT composites rather than stress transfer to the nanotube.

Chapter 7 concludes with a summary of the main results and a list of essential criteria for the formation of polymer/nanotube composites that utilise the best characteristics of both elements. Finally, a direction is suggested for future research based on the findings of this thesis.

1.6 References

---

[1] A.B. Dalton, S. Collins, E. Munoz, J.M. Razal, V.H. Ebron, J.P. Ferraris, J.N. Coleman, B.G. Kim, R. H. Baughman; "Super-tough carbon-nanotube fibres", *Nature* **423**, 703 (2003)

[2] D. Qian, E.C. Dickey, R. Andrews, T. Rantell; "Load transfer and deformation mechanisms in carbon nanotube-polystyrene composites", *Appl. Phys. Lett.* **76**, 2868 (2000)

[3] Biercuk, M. J.; Llaguno, M. C.; Radosavljevic, M.; Hyun, J. K.; Johnson, A. T.; Fischer, J. E.; *Applied Physics Letters* 2002, *80,* 2767.

[4] M. Cadek, J.N. Coleman, V. Barron, K. Hedicke, W.J. Blau; "Morphological and mechanical properties of carbon-nanotube-reinforced semicrystalline and amorphous polymer composites", *Appl. Phys. Lett.* **81**, 5123 (2002)

[5] B.E. Kilbride, J. N. Coleman, P. Fournet, M. Cadek, A. Drury, W.J. Blau; "Experimental observation of scaling laws for alternating current and direct current conductivity in polymer-carbon nanotube composite thin films", *J. Appl. Phys.* **92,** 4024 (2002)

[6] P. Pötschke, S.M. Dudkin, I. Alig; "Dielectric spectroscopy on melt processed polycarbonate – multiwalled carbon nanotube composites", *Polymer* **44**, 5023 (2003)

[7] *Plastics News* **March 22**, (2004): a weekly newspaper founded in Akron, Ohio, in 1989 by Crain Communications Inc.

[8] *Plastics News* **June 24**, (2003)

[9] H. Zhou; "Nucleation and nucleating agents in crystalline polymers: A literature review", *GE Research & Development* **98CRD138**, (1998)

[10] M.S.P. Shaffer, I.A. Kinloch; "Prospects for nanotube and nanofibre composites", *Composites Science and Technology* **64,** 2281 (2004)

[11] S. Iijima; "Helical microtubules of graphitic carbon", *Nature* **354**, 56 (1991)

[12] M. Endo, Ph.D. Thesis (1975)

[13] S. Iijima, T. Ichihashi; "Single-shell carbon nanotubes of 1nm diameter", *Nature* **364**, 737 (1993)

[14] R.H. Baughman, A.A. Zakhidov, W.A. de Heer; "Carbon nanotubes – the route toward applications", *Science* **297**, 787 (2002)

[15] R. Rawstern, "Nanotube surveys" updated Nov 2004, http://www.nanotech-now.com/nanotube-survey-april2003.htm.

[16] P. Collins, J. Hagerstrom; "Carbon nanotubes: a high performance conductive additive", Hyperion Catalysis International.

[17] J. Sandler, M.S.P. Shaffer, T. Prasse, W. Bauhofer, K. Schulte, A.H. Windle; "Development of a dispersion process for carbon nanotubes in an epoxy matrix and the resulting electrical properties", *Polymer* **40**, 5967 (1999)

[18] P.M. Ajayan, O.Z. Zhou; "Applications of Carbon Nanotubes", Topics Appl. *Phys* **80**, 391 (2001)

[19] A.G. Rinzler, J.H. Hafner, P. Nikolaev, L. Lou, S.G. Kim, D. Tomanek, D. Colbert, R. E. Smalley; *Science* **269**, 1550 (1995)

[20] Y. Saito, S. Uemura, K. Hamaguchi; *Jpn. J. Appl. Phys.* **37**, L346 (1998)

[21] A. Star, J-C. P. Gabriel, K. Bradley, G. Grüner; "Electronic detection of specific protein binding using nanotube FET devices", *Nanolett.* **3**, 459 (2003)

[22] A. Srivastava, O.N. Srivastava, S. Talapatra, R. Vajtai and P.M. Ajayan, "Carbon nanotube filters", *Nat. Mat.* **3**, 610 (2004)

[23] M. Hirscher, M. Becher, M. Haluska, F. von Zepplin, X. Chen, U. Dettlaff-Weglikowska, S. Roth; "Arc carbon nanostructures an efficient hydrogen storage medium?", *J. Alloys and Compounds* **356-357**, 433 (2003)

[24] X. Li, H. Zhu, C. Xu, Z. Mao, D. Wu; "Measuring hydrogen storage capacity of carbon nanotubes by tangent-mass method", *International Journal of Hydrogen Energy* **28**, 1251 (2003)

[25] C.E. Bakis, L.C. Bank, V.L. Brown, E. Cosenza, J.F. Davalos, J.J. Lesko, A.Machida, S.H. Rizkalla, T.C. Triantafillou; "Fiber-Reinforced Polymer Composites for Construction — State-of-the-Art Review", *Journal of composites for construction*, American Society of Civil Engineers, **73** (2002)

[26] R. Andrews, M.C. Weisenberger; "Carbon nanotube polymer composites", *Current opinion in Solid State and Materials Science* **8**, 31 (2004)

[27] P.J.F. Harris; "Carbon nanotube composites", *International Material Reviews* **49**, 31 (2004)

[28] F. Fisher, C. Brinson; "Carbon nanotubes literature review", *Website www.tam.northwestern.edu/~ftf234/ nano/LitReview/LitTry3/NanotubeReview022101web.pdf*

[29] J.P. Salvetat-Delmotte, A. Rubio; "Mechanical properties of carbon nanotubes: a fiber digest for

beginners", *Carbon* 40, 1729 (2002)

[30] W.D. Callister; "Materials Science and Engineering: An introduction", *John Wiley and Sons*, 6th ed., New York (2003)

[31] P.J. Walsh; "Carbon Fibers", *ASM Handbook* **21**, 35 (2001)

[32] D.D.L. Chung; "Carbon Fiber Composites", *Butterworth-Heinemann*, Boston (1994)

[33] G.G. Tibbetts; "Carbon Fibers, Filaments and Composites", ed. J.L. Figueiredo, C.A. Bernardo, R.T.K. Baker, and K.J. Huttinger, *Kluwer Academic Publishers*, Dordrecht, 73 (1990).

[34] K. Hata, D.N. Futaba, K. Mizuno, T. Namai, M. Yumura, S. Iijima; "Water-Assisted Highly Efficient Synthesis of Impurity-Free Single-Walled Carbon Nanotubes", *Science* **306**, 1362 (2004)

[35] E.W. Wong, P.E. Sheehan, C.M. Lieber; "Nanobeam Mechanics: Elasticity, Strength, and Toughness of Nanorods and Nanotubes", *Science* **277**, 1971 (1997)

[36] M.F. Yu, O. Lourie, M.J. Dyer, K. Moloni, T.F. Kelly, R.S. Ruoff; "Strength and Breaking Mechanism of Multiwalled Carbon Nanotubes Under Tensile Load", *Science* **287**, 637 (2000)

[37] S.S. Xie, W.Z. Li, Z.W. Pan, B.H. Chang, L.F. Sun; "Mechanical and physical properties on carbon nanotube", *J. Phys. Chem. Solids* **61**, 1153 (2000)

[38] T.W. Hughes; "Fly Ash Enhanced Ca rbon Nanofiber-Reinforced High Strength Cement", *Ohio coal development office annual project abstract* (2004)

[39] M.D. Frogley, D. Ravich, H.D. Wagner; "Mechanical properties of carbon nanoparticle-reinforced elastomers", *Composites Science and Technology* **63**, 1647 (2003)

[40] J.K.W. Sandler, S. Pegela, M. Cadek, F. Gojny, M. van Es, J. Lohmar, W.J. Blau, K. Schulte, A.H. Windle, M.S.P. Shaffer; "A comparative study of melt spun polyamide-12 fibres reinforced with carbon nanotubes and nanofibres" *Polymer* **45**, 2001 (2004)

[41] J.B.Gao, M.E. Itkis, A.P. Yu, E. Bekyarova, B. Zhao, R.C. Haddon; *Journal of the Americal Chemical Society* **127**, 3847 (2005)

[42] Zoltek; "User's guide for short carbon fiber composites", *Zoltek Companies Inc. St. Louis* (2000)

[43] C.G. Zhao, G.J. Hu, R. Justice, D.W. Schaefer, S.M. Zhang, M.S. Yang, C.C. Han; *Polymer* **46**, 5125 (2005)

[44] C. Park, Z. Ounaies, K.A. Watson, R.E. Crooks, J. Smith, S.E. Lowther, J.W. Connell, E.J. Siochi, J.S. Harrison, T.L. St. Clair; "Dispersion of single wall carbon nanotubes by in-situ polymerization under sonication", *Chemical Physics Letters* **364**, 303 (2002)

[45] S. Kumar, H. Doshi, M. Srinivasaro, J.O. Park, D.A. Schiraldi; *Polymer* 43, 1701 (2002)

[46] K. Lozano, E.V. Barrera; *Journal of Applied Polymer Science* **79**, 125 (2001)

[47] B.P. Grady, F. Pompeo, R.L. Shambaugh, D.E. Resasco; "Nucleation of Polypropylene Crystallization by Single-Walled Carbon Nanotubes", *J. Phys. Chem. B* **106**, 5852 (2002)

[48] Z.J. Jia, Z.Y. Wang, C.L. Xu, J. Liang, B.Q. Wei, D.H. Wu, S.W. Zhu; "Study on poly(methyl methacrylate)/carbon nanotube composites"; *Materials Science and Engineering* **A271**, 395 (1999)

[49] K.W. Putz, C.A. Mitchell, R. Krishnamoorti, P.F. Green; *Journal Of Polymer Science Part B-Polymer Physics* **42**, 2286 (2004)

[50] C. Velasco-Santos, A.L. Martinez-Hernandez, F.T. Fisher, R. Ruoff, V.M. Castano; *Chemistry Of Materials* **15,** 4470 (2003)

[51] S. Kumar, T.D. Dang, F. E. Arnold, A. R. Bhattacharyya, B. G. Min, X. Zhang, R. A. Vaia, C. Park, W. W. Adams, R. H. Hauge, R. E. Smalley, S. Ramesh, P.A. Willis; *Macromolecules* **35**, 9039 (2002)

CHAPTER TWO: MATERIALS AND CHARACTERISATION TECHNIQUES

2.1 Introduction

It is predicted that carbon nanotubes have a Young's modulus in the order of 1 TPa[1] and can possess conductivities similar to copper[2,3]. In order to create composites to harness these mechanical or electronic properties, we must first choose a suitable matrix material in which to embed and disperse the nanotube powder. Polymers make good candidates and have been shown to coat the nanotube surface allowing the formation of a stable dispersion in solution[4,5]. An experiment carried out in 1998 in our research group[6] added arc generated carbon soot, containing multi-walled carbon nanotubes (ArcMWNT), to a poly(*m*-phenylenevinylene-co-2,5-dioctyloxy-*p*-phenylenevinylene) (PmPV)/Toluene solution. It was found that the characteristically yellow polymer solution turned black with the addition of nanotubes. Extensive research went on to demonstrate that carbon impurities actually sedimented to the bottom of the solution and that the nanotube rich solution could be decanted and filtered to yield pure ArcMWNT[7]. Furthermore, the composite solution was extremely stable over long time periods: samples are stored which have suspended MWNT in excess of four years. It is suspected that many of the physical properties observed in polymer/nanotube composites such as the PmPV/ArcMWNT are related to the formation of crystalline polymer coatings around the nanotubes in solution. The work presented here aims to identify the nature of these crystalline coatings by choosing two polymers known to produce stable dispersions of carbon nanotubes – namely (PmPV) and Poly(vinyl alcohol) (PVOH)[8]. In this chapter the polymers, nanotubes and techniques used to characterise their composites will be discussed.

2.2 Polymers

2.2.1 PmPV

Organic polymers are primarily comprised of carbon, hydrogen, nitrogen and oxygen and can be natural or synthetic. Conjugated polymers consist of alternating double and single C-C bonds. Since carbon atoms in C=C are sp^2 hybridised, P_z orbital overlap occurs so that a delocalised π electron cloud exists above and below the plane of the sigma bonds that form the structural framework of the polymer chain. Figure 2-1(c) shows the bonding electron pair reside in the bonding molecular π orbital which corresponds to Highest Occupied Molecular Orbital level (HOMO). The antibonding orbital, which is of higher

energy, is empty and corresponds to the Lowest Unoccupied Molecular Orbital (LUMO) level.

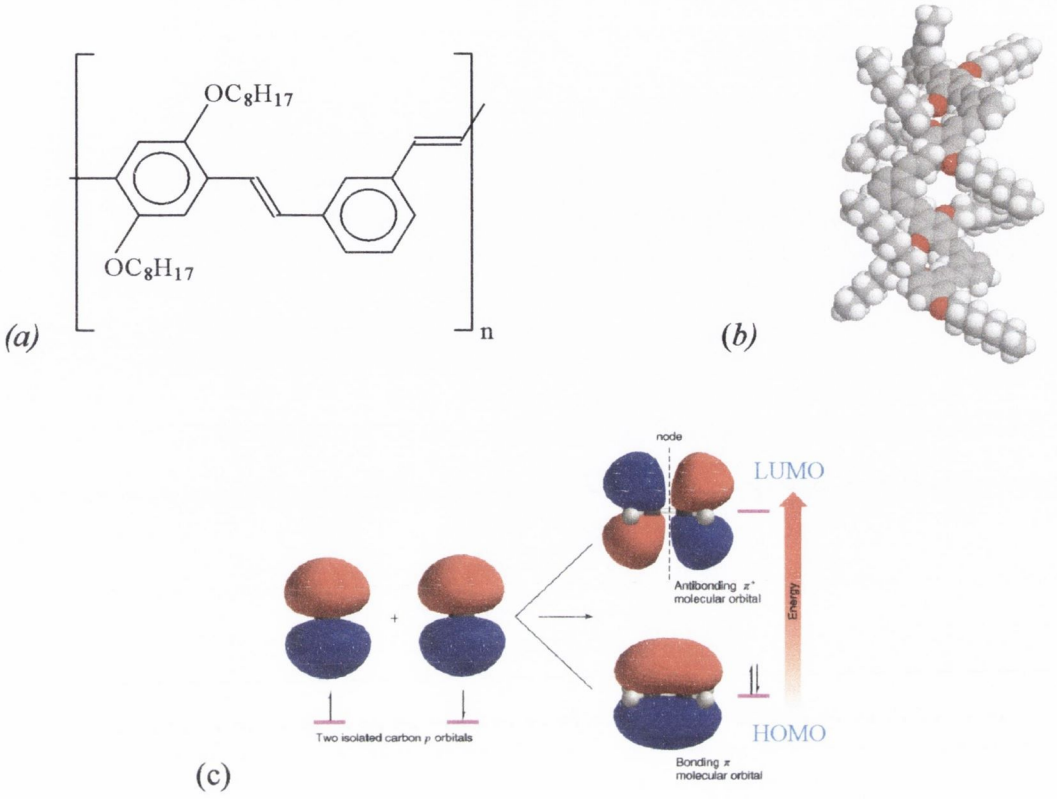

Figure 2-1(a): *PmPV monomer structure.* ***(b)*** *Optimised PmPV polymer structure*[9] ***(c)*** *P orbital bonding schematic.*

Optical or thermal excitation can promote an electron from the HOMO to the LUMO level (π-π^* transition) creating an excited molecular state. In other words, electrons can be excited from the valence band (HOMO) to the conduction band (LUMO) if sufficient energy is added to the system to overcome energy difference between the two levels. However, the energy difference, or band gap, is usually much larger than the thermal energy so virtually no electrons are promoted thermally to the LUMO level. This lack of conduction electrons can be overcome by incorporating a dopant material to increase the charge density of the polymer and increase the number of charge carriers. When an electron is excited from the HOMO level, the charge associated with the vacant electron site is positive. This vacant site is termed a hole and contributes to the evolution of the electronic system since under the right conditions it may be reoccupied by an electron. Such an event is termed electron-hole recombination and the energy lost during the decay of the excited state conduction electron may be observed as photon emission. The excited

electron states necessary to create the environment for electron-hole recombination may be optically induced. Photon emission resulting from optically induced states is termed photoluminescence (PL). Alternatively, excited electron states can be electrically injected into system by the application of an external electric potential. Light emitted through this process is termed electroluminescence.

Poly(*m*-phenylenevinylene-co-2,5-dioctyloxy-*p*-phenylenevinylene) (PmPV), as shown overleaf in Figure 2-1(a), is a derivative of poly(*p*-phenylenevinylene) (PPV). PPV is a semi-conjugated organic polymer which was observed to electroluminesce by Burroughes et al in 1990[10]. The meta linkage and bulky flexible dioctyloxy sidegroups characteristic of PmPV were designed to increase the luminescence efficiency by increasing interchain separation thus minimising the formation of non-emissive species such as interchain polaron pairs[11,12]. A polaron pair consists of an electron and hole residing on opposite chains bound by their mutual Coulomb attraction and has been proposed[13] as a non-radiative decay route in PPV. The more crystalline the polymer, the smaller the interchain separation, thus the probability of polaron pair formation increases. An exciplexe is conceptually similar to a polaron pair but the excited state is created between a ground state molecule and an excited state molecule. The exciplexe can be delocalised over a number of monomer units on a single polymer chain or between two polymer chains. In general polaron pairs are non-emissive while exciplexes tend to be emissive[12]. Excimers are simply a sub-class of exciplexe and the term is used instead of exciplexe when the excited state involves two molecules of the same species.

The PmPV used in this study was synthesised in our laboratory via the Horner route, shown in Figure 2-2, since Horner-ylides are more reactive than the corresponding Wittig-ylides[14]. Furthermore the Horner reaction resulted in better yields in previous investigations[15,16] and the phosphorous product is soluble in water, which makes it easier to separate from the alkene product.

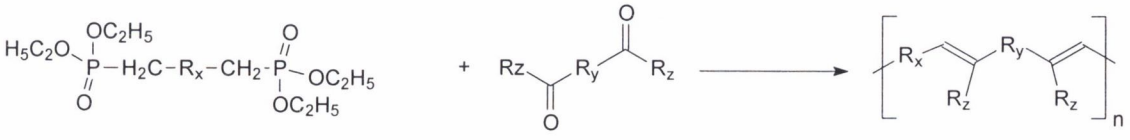

Figure 2-2: *Schematic of Horner synthesis route.*

The phenyl substitutions R_z on the vinylene bond make the polymers soluble and protect them against degradation due to the action of oxygen and light. Additionally, phenyl substitution is expected to offer various possibilities for the introduction of electron donating or withdrawing groups via the phenyl rings and allows diverse structural modifications[17]. For PPV it has been suggested[18] that the *cis* configuration yields a higher a higher solid state emission efficiency than the *trans* configuration. This is consistent with crystallinity studies reported by Drury et al[16] that show PmPV produced by the Horner route (>95% *trans*) is more crystalline than PmPV produced using the Wittig (<86% *trans*). The low crystallinity of the *cis* PmPV implies greater chain separation thus reducing the formation of non-radiative interchain excited states which maximises solid state emission.

Observations in our research group show that for purification of carbon nanotubes PmPV batches with high ratio of *trans*-configuration are required since they tend to wrap more effectively around the carbon nanotube. Modelling studies suggest that the all *trans* polymer chain coils in a regular manner with a coil diameter of 20 Å and a pitch of 6 Å (in vacuum) while the introduction of *cis* linkages into the polymer chain results in a more random coiling[4,6,9,19].

Gel permeation chromatography (GPC) was used to determine a weight-average molecular weight (M_w) of 48,533 and number-average molecular weight (M_n) of 8785 for the PmPV used throughout this thesis. The polydispersivity (M_w/ M_n) is therefore 5.5 and the average chain length is 19 monomer units.

2.2.2 Poly(vinyl alcohol)

Poly(vinyl alcohol) (PVOH) is an organic polymer with monomer and polymer structures as shown in Figure 2-3. The monomer is synthesised by the hydrolysis of polyvinyl acetate since PVOH cannot be produced via a direct addition or condensation polymerisation. Parts of the chain that are not completely hydrolysed during the reaction are left with residual ketone groups. Polymers in general are classified by their molecular weight as determined by chain length. The degree of hydrolysation, which quantifies the number of -OH functional groups present in the chain, must be specified in the case of PVOH. These parameters determine the physical characteristics of the polymer: its

solubility, viscosity, strength and crystallinity – all crucial factors when selecting a host for composite formation.

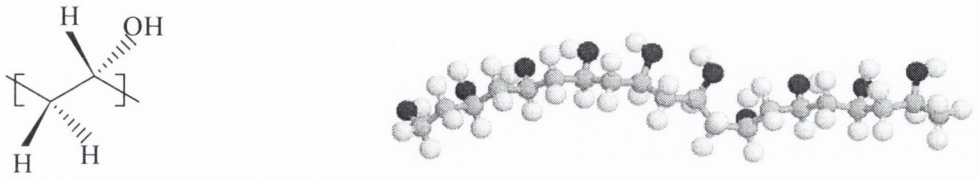

Figure 2-3: Monomer and polymer structure of poly(vinyl alcohol).

The tacticity of a polymer refers to the arrangement of the functional group along the chain and determines the degree of freedom of a polymer chain and therefore its crystallisation kinetics. Isotactic chains have all functional groups residing on the same side of the chain while a syndiotactic polymer has alternating functional groups on either side of the plane. A chain in which the groups are randomly orientated is described as atactic. Tacticity significantly affects the solubility of PVOH with the syndiotactic form being the least soluble. The reason for this is suggested in the literature[20] to be the varying degree of intermolecular and intramolecular hydrogen bonding arising from those OH groups still present in the solid and those already present on the solubilised chains. Tactic specific samples are difficult to produce and therefore commercial polymers usually contain a mix of all three types. It has been reported that the highest degree of crystallinity attainable in PVOH in not dependent on a high degree of tacticity – the highest value of 70% was obtained by annealing common atactic PVOH[21]. The PVOH used in our study was purchased from Sigma Aldrich [product code: 9002-89-5] with a quoted molecular weight of 30k-70k g/mol specified with a 98% degree of hydrolysation.

Pritchard in his book "Poly(vinyl alcohol)"[20] discusses the non-toxic nature of the polymer – it is a component of many cosmetics, is used as a matrix for bacteria resistant agents during treatment of first and second degree burns and an early patent advocated its addition to ice-cream at a concentration of 1% to improve texture. The author does not endorse this practice but highlights that PVOH is speculated to pass unchanged through the alimentary canal. However, when injected subcutaneously the polymer has been shown to cause adverse effects in rats when molecular weight exceeds 50,000. Therefore molecular weights less than 50,000 which have been shown to pass safely through kidneys may have potential in biologically compatible composites of the future for

applications such as injection into joints to coat bone and provide a wear reducing lubricant to treat arthritis. This would depend on the toxicity of the filler and quality of encapsulation within the polymer matrix.

2.3 Carbon nanotubes

A carbon nanotube is an allotrope of carbon along with diamond, graphite and fullerenes. Diamond is a tetrahedral 3d matrix of sp^3 bonded carbon atoms while graphite consists of sheets of carbon atoms each sp^2 bonded to 3 other carbon atoms. Fullerenes contain five and six membered rings of carbon coming together in a spherical structure much like a soccer ball so that each carbon is covalently bonded to 3 others in a trigonal planar arrangement. Graphene is a single atomic layer of graphite where the carbon atoms forming a honeycomb structure in an sp^2 arrangement. Rolled up sheets of graphene form the tube of the nanotube molecule as shown in Figure 2-4[22].

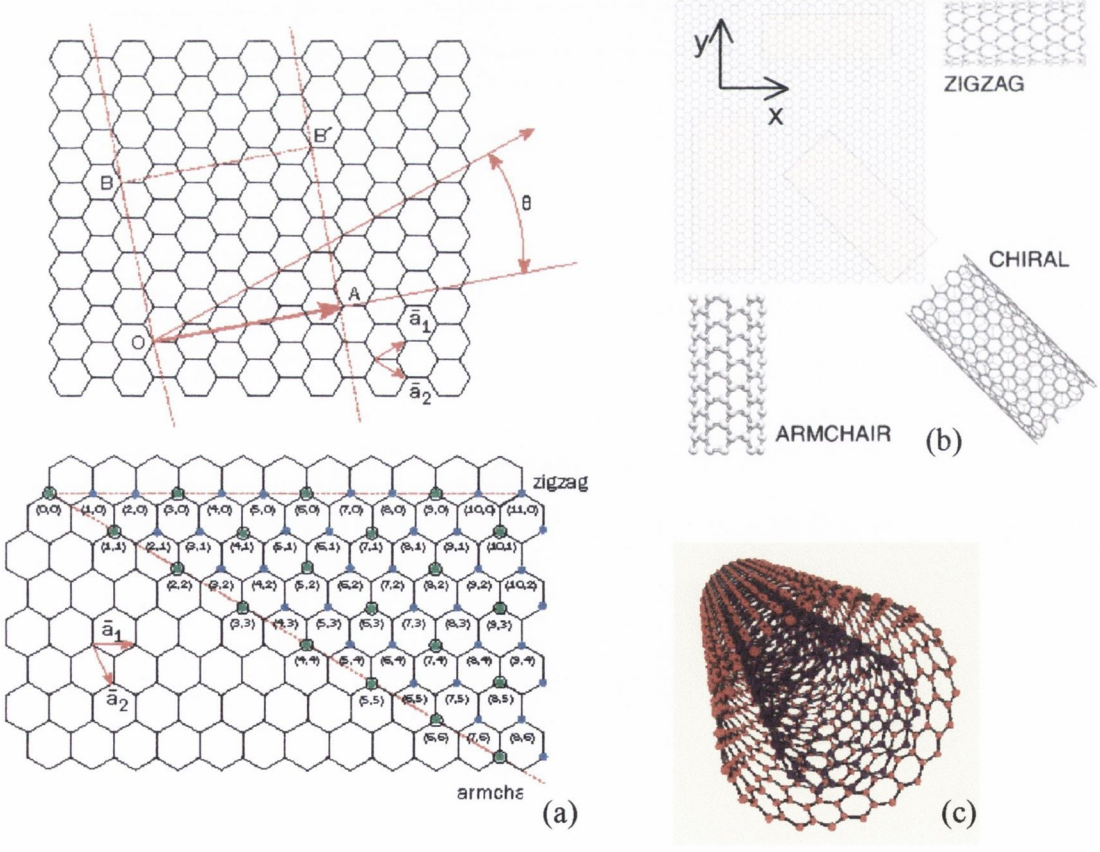

Figure 2-4(a): *Variables used to parameterise the hexagonal lattice that can be rolled to form nanotubes as shown in* ***(b)*** ***(c)*** *Double walled carbon nanotube.*

Each of the numerous configurations can be expressed using a chiral vector written in terms of the unit vectors $\hat{a}_1$ and $\hat{a}_2$ with the chiral angle, θ, measured relative to the $\hat{a}_1$ direction. The chiral vector can therefore be written as $C_h = n\hat{a}_1 + m\hat{a}_2$ where the nanotube (n, m) is formed by rolling the graphene sheet such that O coincides with A and B with B' as shown in Figure 2-4(a). Figure 2-4(b) shows that when $\theta=0°$ the structure is termed zigzag and will be written (n, 0) or (0, m) while those with $\theta=30°$ are armchair nanotubes written as (n, n). All other possible structures, which will have a chiral angle between 0° and 30°, are called chiral nanotubes. It is the chirality of the CNT that determines whether it is metallic, semi-conducting or insulating. The ends of a nanotube are capped with half a fullerene molecule forming a mechanically strong and chemically stable species.

The two main categories of nanotubes are single wall nanotubes (SWNT) and multiwalled nanotubes (MWNT). Different synthesis conditions are employed depending on the type of nanotube desired. SWNT consist of a single cylinder of graphene. They have diameters in the range of 0.7 nm to 1.7 nm and lengths up to several millimetres depending on the growth conditions[23]. MWNT resemble the Matryoshka Russian doll structure and are simply concentrically stacked SWNT with incrementally increasing diameter as illustrated by the double walled nanotube of Figure 2-4(c). They have diameters typically in the range of 10 to 50 μm. These concentric walls have been shown to have a constant spacing of 0.34 nm, which is very similar to the sheet spacing of 0.335 nm for graphite.

2.3.1 Electrical properties of carbon nanotubes

All armchair and one-third of the possible zigzag structures are metallic and these metallic tubes will have m and n values such that $|m-n| = 3q$ where q is an integer. The electronic properties of the remaining nanotube configurations differ depending on their chirality vector. Figure 2-5 illustrates that an 'armchair' CNT shows metallic behaviour and is therefore electrical conductive while 'zig-zag' and chiral show two types of semi-conducting behaviour: one has a band gap of hundredths of an electron volt, while others have about a 1-eV band gap.

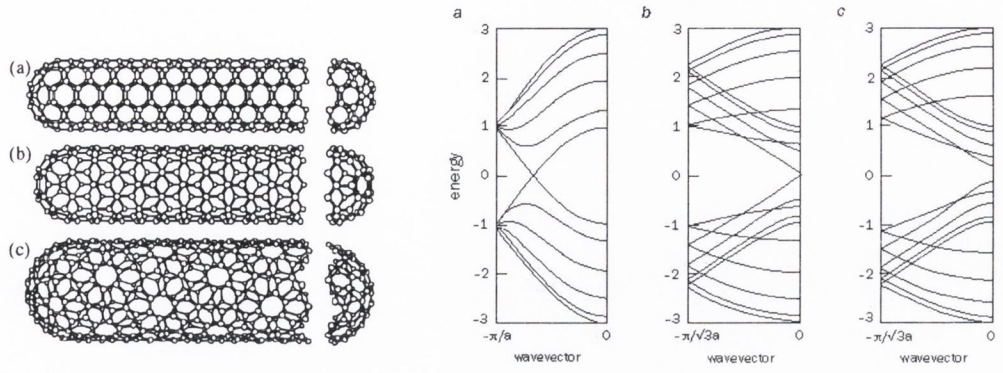

Figure 2-5: *Band structure calculations for single walled carbon nanotubes[24]* ***(a)*** *shows a metallic nanotube with a finite density of states at the Fermi energy* ***(b)*** *shows a semi conducting nanotube with zero bandgap whereas* ***(c)*** *shows semi-conducting behaviour with bandgap.*

Nanotubes have been measured to have resistivities ranging from of 0.05 μΩ m to 10 mΩ m[3]. These values vary widely due to the various chiralities and compare well with the resistivity of copper which is 0.017 μΩ m. The electronic properties of NT result from quantum confinement of electrons in the radial direction by the single atom thickness of the graphene sheet and periodic boundary conditions prevent circumferential propagation. Only axial propagation is possible so nanotubes are a perfect example of a 1D conductor. Individual tubes have been observed to conduct electrons ballistically, without scattering, with coherence lengths of several microns[25]. In addition, they can carry a current density of $>10^9$ A/cm² which is the highest of any known material[26].

2.3.2 Mechanical properties of carbon nanotubes

Impressive mechanical properties were theoretically predicted for carbon nanotubes long before the first experiments were possible. Overney et al calculated a Young's modulus (Y) of 5 TPa for SWNT in 1993[27]. It is important to note that since carbon nanotubes are hollow structures these values were calculated using the cylindrical surface area of the carbon nanotube rather than cross sectional area. In 1999 Srivastava et al[28] computed the critical stress of a SWNT to be 153 GPA for a 12% compressed nanotube in good agreement with a measured value of 135 – 147 GPa by Lourie et al[29]. Lourie's analysis required assuming a conservative Y value of 1.2 TPa for nanotubes based on another relatively early experiment carried out by Treacy et al[1] in 1996. That experiment to evaluate Y for MWNT was a TEM method where one end of the nanotube was effectively

clamped at the edge of a grid while an oscillating deflection was induced at the other end. A model was applied to the magnitude of deflection and calculations yielded Y=1 TPa[1]. More recent experiments[30] in 1998 using Raman spectroscopy have measured a value of Y=2 TPa for a MWNT and 3 TPa for a SWNT. The approximate agreement between these theoretical and measured values is encouraging research worldwide to focus on the potential of carbon nanotubes as reinforcing fillers and is the motivation for the second part of this thesis.

2.3.3 Carbon nanotube production methods

Carbon nanotubes can be produced by arc discharge, chemical vapour deposition or laser ablation. Arc discharge was the method by which the first MWNT's were prepared by Iijima[31,32]. In that process two graphite rods are connected to a power supply with a gap in the order of a millimetre. A current of 100 amps passes through the rods causing the carbon to vaporise into hot plasma some of which recondenses in the form of nanotubes. The tubes produced are of high quality with few defects. Adding metal catalysts to the rod and changing the temperature allows production of both SWNT and MWNT. The disadvantages of this method are low yield (around 30%), and short tubes (50 microns or less). A typical experimental setup is shown in Figure 2-6.

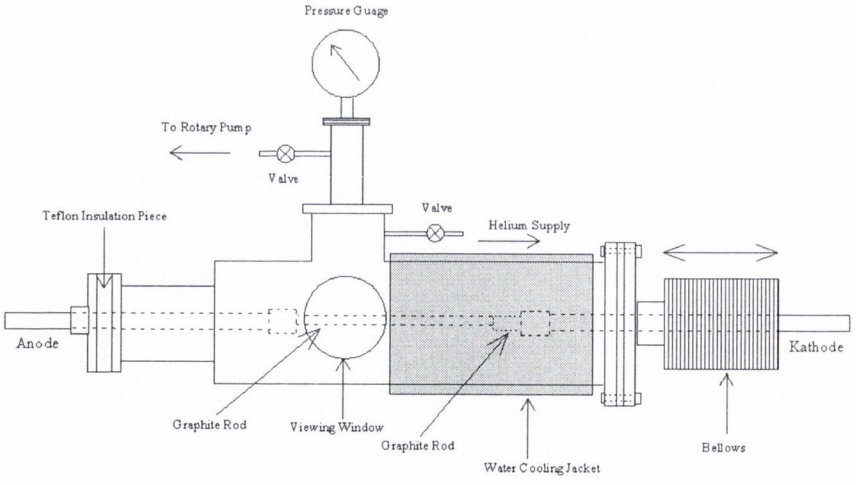

Figure 2-6: *Arc discharge carbon nanotube generator.*

Chemical Vapour Deposition (CVD) is a technique where a substrate is placed in an oven at ~600 °C as shown in Figure 2-7 overleaf. A carbon feed gas such as methane is slowly added, and as the gas decomposes it recombines as nanotubes. A porous catalyst can be used to increase efficiency and growth position control. While this method can produce

high yields, these nanotubes are often riddled with defects and consequently have much lower tensile strength than arc discharge tubes.

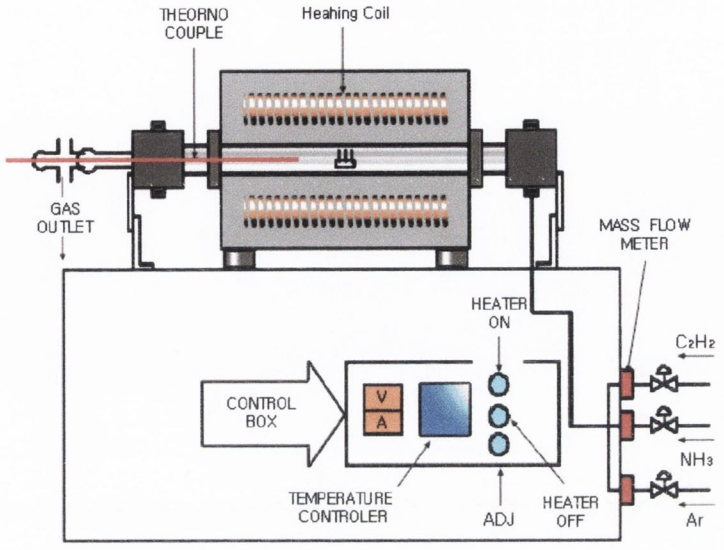

Figure 2-7: *Chemical Vapour Deposition chamber. Image taken from Iiljinnanotech.*

The high-pressure carbon monoxide (HiPco) process, developed at Rice University, has been reported[33] to produce single-walled carbon nanotubes from gas-phase reactions of iron carbonyl in carbon monoxide at high pressures (10-100 atm). The product is reported to contain 97% SWNT.

Laser Ablation is a very costly method that produces SWNT's by focussing a laser on graphite target in an Argon atmosphere[34]. This gives a typical yield of around 70% and varying the furnace temperature gives the great advantage of diameter control.

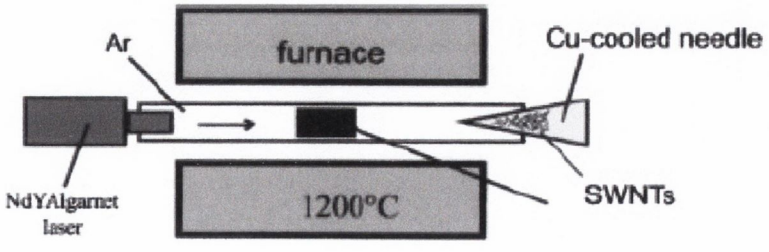

Figure 2-8: *Experimental set-up for production of SWNTs and MWNTs using laser technique: high power laser is focused on composite graphite target (in Ar atmosphere) located inside furnace at 1200 ℃ – tubes are collected from Cu-cooled water trap.*

None of the methods can be tuned to yield a nanotube with a specific chirality although much research is focused in this area. Instead a range of chiralities is produced along with graphitic or catalyst impurities. A summary of the NT production techniques is given in Table 2-1.

Table 2-1: *Summary of carbon nanotube production techniques*[35].

Arc discharge method	Chemical vapor deposition	Laser ablation (vaporization)
Ebbesen and Ajayan, NEC, Japan 1992	Endo, Shinshu University, Nagano, Japan	Smalley, Rice, 1996
Connect two graphite rods to a power supply, place them millimeters apart, and throw switch. At 100 amps, carbon vaporizes in a hot plasma.	Place substrate in oven, heat to 600 C, and slowly add a carbon-bearing gas such as methane. As gas decomposes it frees up carbon atoms, which recombine in the form of NTs	Blast graphite with intense laser pulses; use the laser pulses rather than electricity to generate carbon gas from which the NTs form; try various conditions until hit on one that produces prodigious amounts of SWNTs
Typical yield = 30%	20 to 100 %	Up to 70%
Can produce SWNT and MWNTs with few structural defects	Easiest to scale to industrial production; long length	Primarily SWNTs, with a large diameter range that can be controlled by varying the reaction temperature
Tubes tend to be short with random sizes and directions	NTs are usually MWNTs and often riddled with defects	By far the most costly, because requires expensive lasers

2.4 Carbon nanotubes selected for composite production.

Multi-walled carbon nanotubes (ArcMWNT) were produced in house by the arc discharge method[36] with a nanotube purity of 45 wt%[7]. These ArcMWNT have been used to make both PmPV and PVOH based composites. It is already known that carbon nanotubes act as reinforcing agents in PVOH composites[37]. To further investigate these polymer/CNT composites, and ultimately determine the reinforcement mechanism, a range of carbon nanotubes was deliberately selected to identify any influence of NT diameter on the magnitude of reinforcement. A range of purified catalytic nanotubes were supplied by Nanocyl S.A. (www.nanocyl.com): Double walled nanotubes (DWNT), "Very thin" MWNT and "Thick" MWNT were obtained with characteristics as shown in Table 2-2 overleaf. This data was available from the specification sheets as published on the nanocyl website and was confirmed in our laboratory by TEM microscopy. Elicarb single walled nanotubes were supplied by Harry Swan on behalf of Thomas Swan and company. In addition "Thin" MWNT were obtained from Dr. W.K. Maser at the University of

Zaragoza in Spain (Z_Thin). OH functionalised Thick MWNT were used in an attempt to crosslink their OH functional groups with those of PVOH.

Table 2-2: *Table of nanotubes used for the data presented in later chapters.*

Type	Supplier	Avg. Diameter	Avg. Length	Purity
Arc MWNT	In house	18 ± 5 nm	<1.5 μm	45%[7]
DWNT	Nanocyl	3 ± 0.5 nm	<50 μm	>90%
Very Thin MWNT	Nanocyl	10 ± 5 nm	<50 μm	>95%
Thin MWNT	Nanocyl	15 ± 5 nm	<50 μm	>95%
Thick MWNT	Nanocyl	19 ± 4 nm	<50 μm	>95%
OH Thick MWNT	Nanocyl	25 ± 5 nm	<50 μm	>95%
SWNT	Elicarb	0.7 ± 0.2 nm	<20 μm	>70%
Thin MWNT	Zaragoza	9 ± 3 nm	<50 μm	>93%

2.5 Thermogravimetric Analysis

Thermogravimetric Analysis (TGA) is a quantitative technique where a sample is placed in a furnace on a sensitive balance and heated, typically at a rate of 10 °C. The furnace environment is controlled by continuously purging the system with air or nitrogen as required. A characteristic curve will be obtained displaying mass against temperature that provides information regarding the composition of the sample. For example, organic polymers heated in air will burn and release combustion products. Consequently, sample mass will decrease continuously until all the sample has burned giving a balance reading of close to zero depending on any inorganic impurities that may be present. If a composite is under investigation, the filler material may be more thermally stable than the polymer matrix and will burn at higher temperatures – this is the case for ArcMWNT. The derivative of the mass versus temperature curve can therefore be used to identify any distinct peaks during combustion. Each peak is assignable to a material or product in the composite and the area under the curve can be used to calculate the filler to matrix mass ratio.

2.6 Differential Scanning Calorimetry

Differential Scanning Calorimetry (DSC) is an advanced technique to measure the heat flow through a sample as the sample is heated at a controlled rate. Heat flow is dependent on sample morphology. If the material is amorphous, a shift in the baseline will be observed when the amorphous chains are given enough thermal energy to facilitate movement of the chains. Thus the material changes from a rigid, glassy state to more rubbery state as the chains become more flexible and a change in heat capacity occurs. The temperature at which this change in material properties occurs is referred to as the glass transition temperature, T_g. If the material is crystalline, a peak in the heat flow occurs as the crystals melt or crystallise. Since melting is an endothermic process, it is observed as an endothermic peak which returns to the baseline upon termination of melting. Conversely, crystallisation appears as an exothermic peak. DSC data can be used to determine the following parameters:

- Glass Transitions (T_g)
- Melting (T_m) and Boiling Points
- Crystallisation Time and Temperature (T_c)
- Percent Crystallinity
- Heats of Fusion and Reactions
- Specific Heat and Heat Capacity
- Oxidative Stability
- Rate and Degree of Cure
- Reaction Kinetics
- Percent Purity
- Thermal Stability and Decomposition Temperature (T_d)

Two different types of DSC machine are available; heat flux or power compensation as shown in Figure 2-8. The machine used in this experiment uses the power compensation method. There are two identical pans, one containing the material to be tested and the other acts as a reference pan.

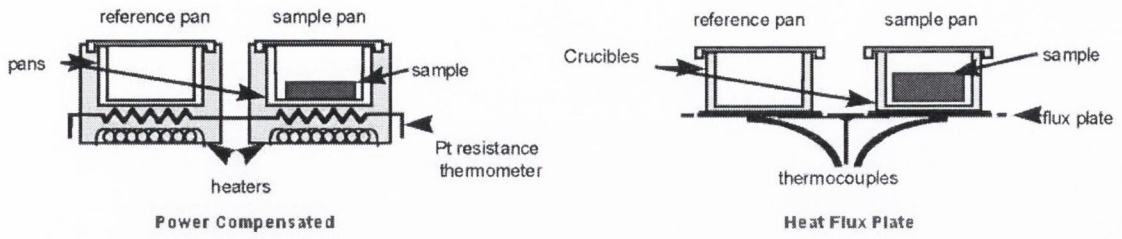

Figure 2-8: *Illustration of the two possible types of DSC machine.*

For power compensation both pans are heated slowly by separated coupled furnaces, such that the temperature in each pan is kept the same. The pan containing the sample will require a different amount of heat to maintain a constant temperature rise than the reference pan because latent heat must be supplied. This is directly related to the heat capacity of the sample, which is the amount of heat required to raise the temperature one degree per unit mass[38].

For crystalline and semi-crystalline materials, an endothermic peak will be observed as the crystalline regions melt and absorb heat. If the sample has not been fully crystallised before the heating process there may also be another transition between T_m and T_g which represents the crystallisation temperature, T_c. This is observed when crystallisable polymers have mobility above the glassy transition such that ordering and crystallisation can occur. The net output in thermal energy is observed as an exothermic peak as the entropy, or disorder, of the system decreases. If a crystalline sample is cooled quickly before the heating step, referred to as quench cooling, the crystallisation will occur during the heating cycle. Therefore the conventional approach to DSC measurements is to first heat the sample to melt the crystalline domains and then a slow cooling step is implemented to allow crystallisation to be completed during cooling. A final heating step will then usually exhibit a glass transition and a sharp melting peak. If the sample is highly crystalline the glass transition, which is associated with any amorphous polymer, may be absent. The values of each parameter discussed above are dependent on the heating and cooling rates employed for the DSC scan. Therefore values quoted in the literature for a specific polymer must be considered with respect to the temperature scan rates used[38,39].

To find the crystallinity as a percentage, we must start by considering the area of the T_c and T_m peaks. The area under the DSC curve is used to calculate the enthalpy required to either melt (ΔH_m) or crystallise (ΔH_c) the sample. It is useful to note that enthalpy does not change with the heating or cooling rate. Melting is observed as an endothermic peak on the heat scan while crystallisation is characterised by an exothermic peak on the cooling scan. If the enthalpy of melting of a theoretical 100% crystalline sample ($\Delta H_{100\%}$) has been calculated then the crystalline fraction (χ) of our unknown sample can be evaluated using Equation 2-1.

$$\chi = \frac{\Delta H_m}{\Delta H_{100\%}}$$

Equation 2-1: *Crystalline fraction of a sample calculated using the enthalpy of melting.*

2.7 Tensile Testing

A tensile tester provides the most direct way to characterise the mechanical properties of a material by applying an increasing force (stress) and measuring the elongation (strain) incurred. Alternatively the elongation can be incremented and the force required to achieve the strain rate can be measured. Deformation where stress (σ) and strain (ε) are proportional is called elastic deformation and is non-permanent elongation. Hooke's law states that for elastic materials, stress is proportional to strain at loads less than the yielding point of the material. This constant of proportionality is Young's modulus (Y) and is therefore calculated from the initial linear part of a stress/strain curve. The stress corresponds to the force per unit area (N/m^2) while strain is dimensionless – this means Y has the unit of pressure (Pa). Other useful parameters are the toughness (T) and the ultimate tensile strength (σ_t), which is the maximum stress applied before fracture of the sample. Toughness is calculated from the area under the stress strain curve and is the energy absorbed per unit volume at fracture. The importance of toughness was highlighted by Gordon in 1976: 'The worst sin in an engineering material is not lack of strength or lack of stiffness, desirable as these properties are, but lack of toughness, that is to say, lack of resistance to the propagation of cracks'[40].

2.8 Dynamic Mechanical Thermal Analysis (DMTA)

DMTA is a technique that measures the modulus (stiffness) and damping (energy dissipation) of materials as they are deformed under periodic stress – it is therefore a dynamic tensile tester with temperature control. From an industry viewpoint the mechanical properties of polymeric materials can be subjected to time, frequency and temperature effects allowing test conditions that simulate the intended application environment. From a research perspective, suitability of innovative materials for new applications can be assessed by considering:

- Modulus
- Damping
- Glass Transition
- Softening Temperature
- Rate of Cure
- Degree of Cure
- Viscosity
- Gelation
- Sound Absorption
- Impact Resistance
- Creep

Films as thin as 5 microns can be studied making DMTA ideal for low sample volume testing. Effects of film orientation can be studied and stress/strain curves can be generated for films and fibres to a better accuracy than is possible with standard physical testing devices, since the mass and inertia of the clamps is much smaller – for this reason results of tensile tests and DMTA will be compared in this thesis.

The Perkin Elmer Diamond DMTA used for our experiments is equipped to carry out tensile tests, bending and shear experiments within a furnace that is heated or cooled with liquid Nitrogen at the required rate. An oscillating force is applied to the sample so that sinusoidal stress and strain curves are recorded as a function of time, as shown in Figure 2-9.

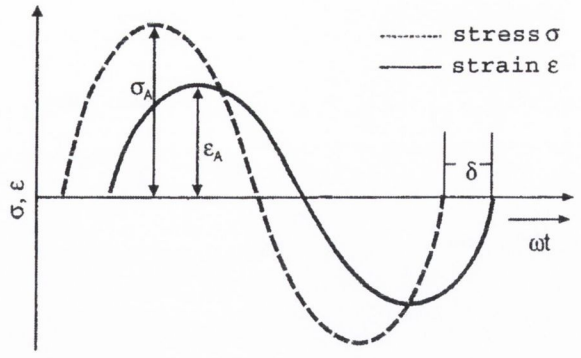

Figure 2-9: Sinusoidal oscillation and response signal of a linear visco-elastic material[85]

Storage modulus (E') represents the stiffness of a material and is proportional to the maximum amount of elastic energy saved in the material during an oscillating loading cycle. It has nearly the same value as the Young's modulus for low deformations and corresponds to that determined by tensile testing. The storage modulus describes the elastic properties of a material.

Energy dissipated in the material during an oscillating loading cycle is represented by the loss modulus (E''). It is proportional to the energy transformed into heat that cannot be regained. The loss modulus describes the viscous properties of a material. An oscillating stress, σ_A, can be expressed as:

$$\sigma_A = \sigma_0 e^{iwt} \qquad \textit{Equation 2-2}$$

Due to the loss of energy during the loading cycle the strain, ε_A, in the sample will exhibit a phase shift relative to the applied stress, σ_A, thus

$$\varepsilon_A = \varepsilon_0 e^{i(wt-\delta)} \qquad \textit{Equation 2-3}$$

The phase angle (δ) represents the phase shift between dynamic stress and dynamic strain in a visco-elastic material that is exposed to a sinusoidal load. The angle δ is expressed in radians. The modulus of the material can therefore be expressed as:

$$E = \frac{\sigma_A}{\varepsilon_A} = \frac{\sigma_0 e^{iwt}}{\varepsilon_0 e^{i(wt-\delta)}} = \frac{\sigma_0 e^{i\delta}}{\varepsilon_0} \qquad \textit{Equation 2-4}$$

Expressing $e^{i\delta} = Cos\delta + iSin\delta$ yields:

$$E = \frac{\sigma_0}{\varepsilon_0} Cos\,\delta + i\frac{\sigma_0}{\varepsilon_0} Sin\,\delta$$
$$= E' + iE''$$

Equation 2-5

The ratio between loss modulus and storage modulus described by the loss factor *Tan δ*. This factor is very useful to describe the damping properties of a material. A high *Tan δ* is characteristically for a material with a more non-elastic behaviour, while a low value of *Tan δ* is characteristic for a more elastic material.

$$Tan\,\delta = \frac{E''(\omega)}{E'(\omega)}$$

Equation 2-6

DMTA is 10 to 100 times more sensitive to changes occurring at the T_g than the DSC technique and is therefore useful to detect a weak T_g [41]. However, DMTA cannot evaluate the crystallinity of a sample and the value for T_g can differ by 10 to 20 °C from that determined using DSC[42]. As with DSC, in addition to quoting the temperature rate used to observe T_g the method of analysis must be stated. Some DMTA operators quote the *Tan δ* peak while others quote the *Tan δ* peak onset or perhaps the onset of the *E'* drop. T_g is quoted as the *Tan δ* peak for all analysis presented in later chapters.

2.9 Modelling of a polymer matrix/reinforcing filler composite

2.9.1 Rule of mixtures

An expression for the Young's modulus of a composite can be derived by assuming the filler geometry is that of a long fibre. In that model, it is assumed that any stress applied to the system will be perfectly transferred from the matrix to the filler so that their Poisson's ratios are equal and equal strain occurs for both elements[43]. This results in the well-known 'rule of mixtures' as shown in Equation 2-7

$$Y_{c_{\parallel}} = v_f Y_f + v_m Y_m, \quad Y_{c_{\perp}} = \frac{Y_f Y_m}{Y_m v_f + Y_f v_m}$$

Equation 2-7: *Rule of mixtures parallel and normal to the principal fibre orientation.*

Where $Y_{\parallel}$ and $Y_{\perp}$ are determined moduli parallel and normal to the principal fibre orientation direction in a continuous unidirectional fibre system. v_f and v_m are the filler and matrix volume fractions, respectively. If the Poisson's ratios are not identical then Equation 2-7 is about 1% in error. The typical Poisson's ratio for thermoplastics matrices is 0.4[43]. The rule of mixtures was then further developed by Cox to model a system where short fibres were used as the filler material.

2.9.2 Cox-shear-lag Theory

Further modifications on the rule of mixture are required to model systems reinforced with short fibres. In this case, the fibre restricts the deformation of the surrounding matrix because it is stiffer than the matrix material. Loads are therefore transferred to the filler via interfacial shear stresses. Cox modelled such a system to derive his shear lag analysis[44] with the assumptions that the fibre and matrix remained elastic in their mechanical response, the interface between the fibre and the matrix has to be perfect and there is no axial force transmitted through the fibre ends:

$$Y_c = Y_m(1-v_f) + Y_f v_f \left(1 - \frac{\tanh\left(\frac{\beta l}{2}\right)}{\left(\frac{\beta l}{2}\right)} \right)$$

Equation 2-8: *Cox-shear-lag Theory*[44,45].

Where the last terms in brackets is explained as the fibre length correlation factor, with **l** as the fibre length and β stands for the stress built up at the fibre ends and is calculated by:

$$\beta = \sqrt{\frac{-4G}{r^2 Y_f \ln(v_f)}}$$

Equation 2-9: *β factor used to incorporate the stress experienced at the fibre ends according to Cox-shear-lag theory*[44,45].

Y_f represents the filler modulus, v_f is the volume fraction, r the fibre radius. G is the polymer shear modulus which is calculated from the expression $G=Y_m/2(1+v)$ where v is the Poisson's ratio and Y_m is the matrix modulus.

Hence, the rule of mixture for randomly oriented fibres can be derived from Equation 2-8 by using η_l to represent the fibre length correlation factor and introducing a term, η_0, to account for random fibre orientation.

$$Y_c = Y_m(1 - v_f) + \eta_l \eta_0 Y_f v_f$$

Equation 2-10: *The Krenchel expression for derived from the rule of mixture for randomly oriented fibres, modified by Cox*[44].

η_0 is called the Krenchel orientation efficiency factor[44,45] and is defined as:

$$\eta_0 = \sum_n a_{fn} \cos^4 \alpha_n \Big/ \sum_n a_{fn}, where \sum_n a_{fn} = 1 \qquad \textit{Equation 2-11}$$

where a_{fn} is the ratio between the cross sectional area presented by a group of fibres oriented at an angle α_n to the applied load direction an the total area of all the fibres at a given cross-section of the composite. The number of groups is designated by n =1, 2, 3, . . . , n[45].

The Krenchel's expression for short carbon fibre composites has been successfully applied for several recent studies of carbon nanotube reinforced polymer composites by Sandler et al[46,47,48].

2.9.3 Halpin-Tsai Theory

The Halpin-Tsai[49] equation is a further refinement of the Krenchel expression and rigorously accounts for a spectrum of fibre lengths and orientations. For randomly oriented nanotubes the Halpin-Tsai equation is expressed as:

$$Y_{random} = \frac{3}{8}Y_{11} + \frac{5}{8}Y_{22}$$

$$Y_{11} = \frac{1+2\left(\frac{l_f}{d_f}\right)\eta_L v_f}{1-\eta_L v_f} Y_m$$

$$Y_{22} = \frac{1+2\eta_T v_f}{1-\eta_T v_f} Y_m$$

Equation 2-12: *Halpin-Tsai Equation for randomly oriented fillers.*

where $\mathbf{Y_{11}}$ and $\mathbf{Y_{22}}$ are longitudinal and transversal components of composite properties such as modulus. The aspect ratio (**l/d**) is the length over diameter ratio for the nanotubes and $\mathbf{v_f}$ is the volume fraction of nanotubes dispersed in the polymer matrix. The $\boldsymbol{\eta}$ parameters are given by

$$Y_C = \left[\frac{3}{8}\frac{1+2\left(\frac{l_{nt}}{d_{nt}}\right)\eta_L V_{nt}}{1-\eta_L V_{nt}} + \frac{5}{8}\frac{1+2\eta_T V_{nt}}{1-\eta_T V_{nt}}\right] Y_M$$

$$\eta_L = \frac{\left(\frac{Y_{nt}}{Y_m}\right)-1}{\left(\frac{Y_{nt}}{Y_m}\right)+2\left(\frac{l_{nt}}{d_{nt}}\right)}$$

$$\eta_T = \frac{\left(\frac{Y_{nt}}{Y_m}\right)-1}{\left(\frac{Y_{nt}}{Y_m}\right)+2}$$

Equation 2-13: *Halpin-Tsai equation applied on carbon nanotube composites.*

Indices used for different moduli are as follows; composite (c), matrix (m) and nanotubes (nt). The modulus values based on this equation have been shown to agree reasonably well with the experimental values for a variety of reinforcement geometries by Mallick[50].

Halpin-Tsai analysis has been successfully applied to the analysis of polystyrene (PS)/MWNT composites where theoretical and experimental values for nanotube modulus were found to agree within 10% by Qian et al[51]. Qian concluded that external tensile loads were transferred to the nanotubes via the PS/MWNT interface. However, previous analysis of PVOH/Carbon nanotube composites by Cadek et al[52] found that Halpin-Tsai theory does not agree with the experimental results suggesting stress transfer is not the

dominant mechanism of reinforcement. Thus, the experiments in this thesis were devised to investigate polymer morphology within the composite and explain the deviation from Halpin-Tsai theory.

2.10 Microscopy

2.10.1 Transmission Electron Microscopy (TEM)

Transmission Electron Microscopy (TEM) uses a stream of monochromatic electrons that are focused to a small, thin, coherent beam by the use of condenser lenses. The wavelength of an electron is described by the de Broglie expression $\lambda=h/mv$, thus with suitable acceleration angstrom wavelengths are achieved and the electrons are scattered from the sample producing an enlarged image. The first lens (usually controlled by the "spot size knob") largely determines the "spot size"; the general size range of the final spot that strikes the sample. The second lens (usually controlled by the "intensity or brightness knob" actually changes the size of the spot on the sample; changing it from a wide dispersed spot to a pinpoint beam. The beam is restricted by the condenser aperture which knocks out high angle electrons before the beam strikes the specimen. A portion of the incident beam is transmitted from the sample and focused by the objective lens into an image that is passed down the column through intermediate and projector lenses. The image strikes the phosphor image screen and light is generated, allowing the user to see the image. The darker areas of the image represent those areas of the sample that fewer electrons were transmitted through (they are thicker or denser). The lighter areas of the image represent those areas of the sample that more electrons were transmitted through (they are thinner or less dense).

2.10.2 Scanning Electron Microscope (SEM)

With a Scanning Electron Microscope (SEM), a stream of monochromatic electrons is condensed by the first condenser lens (usually controlled by the "coarse probe current knob"). This lens is used to both form the beam and limit the amount of current in the beam. It works in conjunction with the condenser aperture to eliminate the high-angle electrons from the beam. This beam is then constricted by the condenser aperture eliminating some high-angle electrons. The second condenser lens forms the electrons into a thin, tight, coherent beam and is usually controlled by the "fine probe current

knob". A user selectable objective aperture further eliminates high-angle electrons from the beam. A set of coils then "scan" or "sweep" the beam in a grid fashion (like a television), dwelling on points for a period of time determined by the scan speed (usually in the microsecond range). The final lens, the Objective, focuses the scanning beam onto the part of the specimen desired. When the beam strikes the sample (and dwells for a few microseconds) it interacts with the material and beam changes are detected. Before the beam moves to its next dwell point, these instruments count the number of interactions (N) and display a pixel on a CRT whose intensity is determined by N. This process is repeated until the grid scan is finished and then repeated, the entire pattern can be scanned 30 times per second.

2.11 UV-Visible and photoluminescence spectroscopy

Ultraviolet and visible (UV-Vis) absorption spectroscopy is the measurement of the attenuation of a beam of light with a wavelength in the range after it passes through a sample or after reflection from a sample surface. The short-wavelength limit for simple UV-Vis spectrometers is 180 nm due to absorption of ultraviolet wavelengths below 180 nm by atmospheric gases. The absorbance, A, is related to the input and output intensities according to the Beer-Lambert Law which is shown in Equation 2-14

$$\frac{I}{I_0} = e^{-A} \qquad \textit{Equation 2-14}$$

The absorbance, A, can be divided by the path length, *l*, to yield the absorption co-efficient α which quantifies the absorbance per metre thus taking film thickness into account.

The absorption of UV or visible radiation corresponds to the excitation of outer electrons. When an atom or molecule absorbs energy, electrons are promoted from their ground state to an excited state. In a molecule, the atoms can rotate and vibrate with respect to each other. These vibrations and rotations also have discrete energy levels, which can be considered as being packed on top of each electronic level as shown in Figure 2-10.

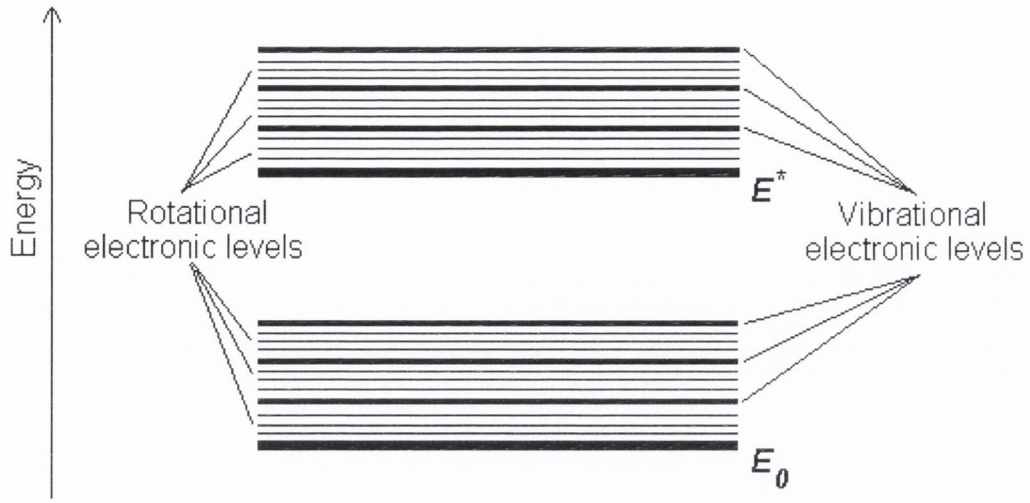

Figure 2-10: *Energy level diagram. E_0 represents the ground state while E^* is the excited state.*

Absorption of ultraviolet and visible radiation in organic molecules is restricted to certain functional groups (chromophores) that contain valence electrons of low excitation energy. The spectrum of a molecule containing these chromophores is complex. This is because the superposition of rotational and vibrational transitions on the electronic transitions gives a combination of overlapping lines. This appears as a continuous absorption band. $\pi \rightarrow \pi^*$ transitions normally give molar absorbtivities between 1000 and 10,000 L mol^{-1} cm^{-1}. These are the transitions of interest in the study of PmPV given the presence of the phenyl group in the polymer structure.

The solvent in which the absorbing species is dissolved also has an effect on the spectrum of the species. Peaks resulting from $n \rightarrow \pi^*$ transitions are shifted to shorter wavelengths (blue shift) with increasing solvent polarity. This arises from increased solvation of the lone pair, which lowers the energy of the *n* orbital. Often the reverse (red shift) is seen for $\pi \rightarrow \pi^*$ transitions. This is caused by attractive polarisation forces between the solvent and the absorber, which lower the energy levels of both the excited and unexcited states. This effect is greater for the excited state, and so the energy difference between the excited and unexcited states is slightly reduced - resulting in a small red shift. This effect also influences $n \rightarrow \pi^*$ transitions but is overshadowed by the blue shift resulting from solvation of lone pairs. This effect is known as solvatochromism.

2.12 Fourier transform infrared spectroscopy (FTIR)

Infrared spectroscopy is particularly applicable to the study of orientation in polymers. Infrared absorbance is due to the interaction between the electric field vector and the molecular dipole transition moments due to the molecular vibrations. The absorbance is at a maximum when the electric field vector and the transition moment are parallel to each other, and zero when the orientation is perpendicular. The orientation of molecular components can be characterised by using the dichroic ratio which is defined as $A_{\parallel}/A_{\perp}$ where $A_{\parallel}$ is the absorbance parallel to the chain axis and $A_{\perp}$ is perpendicular[53,54].

The differing alignment of the molecules results in changes in the intensities of a number of the infrared modes and therefore is an indicator of crystallinity. Because each interatomic bond may vibrate in several different motions (stretching or bending), individual bonds may absorb at more than one IR frequency. The frequency range of IR radiation is 4000 to 400 cm^{-1}. Stretching absorptions usually produce stronger peaks than bending, however the weaker bending absorptions can be useful in differentiating similar types of bonds (e.g. aromatic substitution). It is also important to note that symmetrical vibrations do not cause absorption of IR radiation. For example, neither of the carbon-carbon bonds in ethene or ethyne absorb IR radiation. As a general rule, the most important factors determining where a chemical bond will absorb are the bond order and the types of atoms joined by the bond. Conjugation and nearby atoms shift the frequency to a lesser degree. Therefore the same or similar functional groups in different molecules will typically absorb within the same, specific frequency ranges.

The complex lower region below 1000 cm^{-1} is known as the "fingerprint region" because almost every organic compound produces a unique pattern in this area - Therefore identity can often be confirmed by comparison of this region to a known spectrum. The IR frequency at which a chemical bond absorbs is inversely proportional to the square root of the reduced mass of the bonded atoms.

2.13 XRD

For X-ray Diffraction (XRD) applications, only short wavelength X-rays in the range of a few angstroms to 0.1 angstrom (1 keV - 120 keV) are used. Because the wavelength of X-rays is comparable to the size of atoms, they are ideally suited for probing the structural

arrangement of atoms and molecules in a wide range of materials[55,56,57]. An X-ray tube generates X-rays by focusing an electron beam that has been accelerated across a high voltage field and bombards a stationary or rotating solid target. As electrons collide with atoms in the target and slow down, a continuous spectrum of X-rays are emitted, which are termed Bremsstrahlung radiation. The high energy electrons also eject inner shell electrons in atoms through the ionisation process. When a free electron fills the shell, an X-ray photon with energy characteristic of the target material is emitted. Common targets used in X-ray tubes include Cu and Mo, which emit 8 keV and 14 keV X-rays with corresponding wavelengths of 1.54 Å and 0.8 Å, respectively.

X-rays primarily interact with electrons in atoms. Diffracted waves from different atoms can interfere with each other and the resultant intensity distribution is strongly modulated by this interaction. If the atoms are arranged in a periodic fashion, as in crystals, the diffracted waves will consist of sharp interference maxima (peaks) with the same symmetry as in the distribution of atoms. Measuring the diffraction pattern therefore allows us to deduce the distance between crystal planes. Braggs law states that

$$n\lambda = 2d\sin\theta \qquad \textit{Equation 2-15}$$

where λ is the wavelength of the x-ray, θ the scattering angle, and n an integer representing the order of the diffraction peak.

Reflection geometry as shown in Figure 2-11 was used for our measurements as usual for thin film samples. Transmission geometry is also shown for completeness.

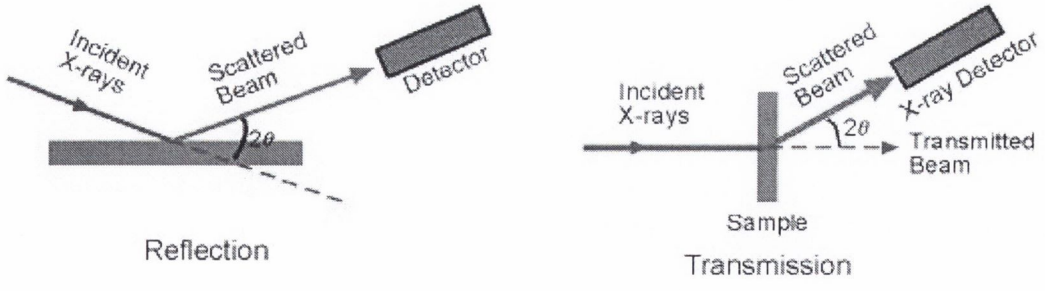

Figure 2-11: *Thin film diffraction experimental setup.*

2.14 Summary

This chapter has introduced the materials used to prepare the composites that will be investigated in subsequent chapters. A brief theory section was been included for each experimental technique used to assess the samples. These techniques included DSC, tensile testing, DMTA, UV-Vis and photoluminescence spectroscopy, FTIR and XRD. Chapter 3 will now discuss the preparation required to produce high quality samples with appropriate geometry for each of the techniques.

2.15 References

[1] M.M.J. Treacy, T.W. Ebbesen, J.M. Gibson; "Exceptionally high Young's modulus observed for individual carbon nanotubes", *Nature* **381**, 678 (1996)

[2] A.B. Kaiser, G. Düsberg, S. Roth; "Heterogeneous model for conduction in carbon nanotubes", *Phys. Rev. B* **57**, 1418 (1998)

[3] P.J.F. Harris; "Carbon nanotube composites", *International Material Reviews* **49**, 31 (2004)

[4] B. McCarthy, J.N. Coleman, R. Czerw, A. B. Dalton, M.I.H. Panhuis, A. Maiti, A. Drury, P. Bernier, J.B. Nagy, B. Lahr, H.J. Byrne, D.L. Carroll, W.J. Blau; "A microscopic and spectroscopic study of interactions between carbon nanotubes and a conjugated polymer", *Journal of Physical Chemistry B* **106**, 2210 (2002)

[5] F. Balavoine, P. Schultz, C. Richard, V. Mallouh, T.W. Ebbesen, C. Mioskowski; "Helical crystallization of proteins on carbon nanotubes: A first step towards the development of new biosensors", *Angewandte Chemie-International Edition* **38**, 1912 (1999)

[6] S.A. Curran, P.M. Ayajan, W.J. Blau, D.L. Carroll, J.N. Coleman, A.B. Dalton, A.P. Davey, A. Drury, B. McCarthy, S. Maier, A. Strevens; "A composite from poly(m-phenylenevinyleneco-2,5-dioctoxy-p-phenylenevinylene) and carbon nanotubes: A novel material for molecular optoelectronics", *Adv. Mater.* **10,** 1091 (1998)

[7] R. Murphy, J.N. Coleman, M. Cadek, B. McCarthy, M. Bent, A. Drury, R.C. Barklie, W.J. Blau; "High-yield, nondestructive purification and quantification method for multiwalled carbon nanotubes.", *J. Phys. Chem. B* **106,** 3087 (2002)

[8] M.S.P. Shaffer, A.H. Windle; "Fabrication and characterization of carbon nanotube/poly(vinyl alcohol) composites.", *Adv. Mat.* **11**, 937 (1999)

[9] M.i.h. Panhuis, R.W. Munn, W.J. Blau; "Optimal polymer characteristics for nanotube solubility", *Synth. Met.* **121,** 1187 (2001).

[10] J.H. Burroughes, D.D.C. Bradley, A.R. Brown, R.N. Marks, K. Mackay, R.H. Friend, P.L. Burns, A.B. Holmes; "Light-Emitting-Diodes Based on Conjugated Polymers", *Nature* **347**, 539 (1990)

[11] M. Yan, L.J. Rothberg, F. Papadimitrakopoulos, M.E. Galvin, T.M. Miller; "Spatially indirect excitons as primary photoexcitations in conjugated polymers", *Phys. Rev. Lett.* **72**, 1104 (1994)

[12] R. Farchioni, G. Grosso; "Organic Electronic Materials", *Springer*, London (2001)

[13] M. Yan, L.J. Rothberg, E.W. Kwock, T.M. Miller; "Interchain excitations in conjugated polymers", *Phys. Rev. Lett.* **75**, 1992 (1995)

[14] J. March; "Advanced Organic Chemistry", 4th Ed., *Wiley*, New York (1992)

[15] S. Maier; *Dipl. thesis*, Private Fachhochschule Fresenius, Wiesbaden, Germany (1997)

[16] A. Drury, S. Maier, M. Rüther, W.J. Blau; "Investigation of different synthetic routes to and structure-property relationships of poly(m-phenylenevinylene-co-2,5- dioctyloxy-p-phenylenevinylene)", *J. Mat. Chem.* **13**, 485 (2003)

[17] H.H. Hörhold, A. Bleyer, E. Birckner, S. Heinze, F. Leonhardt, "A novel approach to light emitting polyarylenes: Cyclization of poly(arylene vinylenes)", *Synth. Met.* **69**, 525 (1995)

[18] W. Holzer, A. Penzkofer, S.H. Gong, A. Bleyer, D.D.C. Bradley; "Laser action in poly (m-phenylenevinylene-co-2,5-dioctoxy-p-phenylenevinylene)", *Adv. Mater.* **8,** 974 (1996)

[19] S.A. Curran, A.P. Davey, J.N. Coleman, A.B. Dalton, B. McCarthy, S. Maier, A. Drury, D. Gray, M. Brennan, K. Ryder, M. Lamy de la Chapelle, C. Journet, P. Bernier, H.J. Byrne, P.M. Ajayan, D.L. Carroll, S. Lefrant, W.J. Blau; "Evolution and evaluation of the polymer/nanotube composite", *Synth. Met.* **103**, 2559 (1999)

[20] J.G. Pritchard; "Poly(vinyl alcohol)", *MacDonald & Co.*, London (1970)

[21] J.F. Kenny, G.W. Willcockson; *J. Polymer Sci.* **4**, 679 (1966)

[22] M. Dresselhaus, G. Dresselhaus, P. Eklund, R. Saito; "Carbon nanotubes", *Physics World*, January (1998)

[23] K. Hata, D.N. Futaba, K. Mizuno, T. Namai, M. Yumura, S. Iijima; "Water-Assisted Highly Efficient Synthesis of Impurity-Free Single-Walled Carbon Nanotubes", *Science* **306**, 1362 (2004)

[24] C. Bourbonnais, D. Jérome; "One-dimensional conductors", *Physics World*, 41 (1998)

[25] S.J. Tans, A.R.M. Verschueren, C. Dekker; "Room-temperature transistor based on a single carbon nanotube", *Nature* **393,** 49 (1998)

[26] B.Q. Wei, R. Vajtai, P.M. Ajayan; "Reliability and current carrying capacity of carbon nanotubes", *Appl. Phys. Lett.* **79,** 1172 (2001).

[27] G. Overney, W. Zhong, D. Tomanek; "Structural rigidity and low-frequency vibrational-modes of long carbon tubules", *Zeitschrift fur physik d-atoms molecules and clusters* **27**, 93 (1993)

[28] D. Srivastava, M. Menon, K. Cho; "Nanoplasticity of Single-Wall Carbon Nanotubes under Uniaxial Compression", *Phys. Rev. Lett.* **83**, 2973 (1999)

[29] O. Lourie, D.M. Cox, H.D. Wagner; "Buckling and collapse of Embedded Carbon Nanotubes", *Phys. Rev. Lett.* **81**, 1638 (1998)

[30] O. Lourie, H.D. Wagner; "Evaluation of Young's modulus of carbon nanotubes by micro-Raman spectroscopy", *J. Mater. Res.* **13**, 2418 (1998)

[31] S. Iijima; "Helical microtubules of graphitic carbon", *Nature* **354**, 56 (1991)

[32] W. Kraetschmer, L.D. Lamb, K. Fostiropoulous, D.R. Huffman; *Nature* 347, 354 (1990)

[33] M.J. Bronikowski, P.A. Willis, D.T. Colbert, K.A. Smith, R.E. Smalley; "Gas-phase production of carbon single-walled nanotubes from carbon monoxide via the HiPco process: A parametric study", *J. Vac. Sci. Technol. A* **19**, 1800 (2001)

[34] M. Terrones; "Carbon nanotubes: synthesis and properties, electronic devices and other emerging applications", *International Material Reviews* **49**, 325 (2004)

[35] H. Cui, O. Zhou, B. Stoner; "Deposition of aligned bamboo-like carbon nanotubes via microwave plasma enhanced chemical vapor deposition.", *J. Appl. Phys.* **88**, 6072 (2000)

[36] M. Cadek, R. Murphy, B. McCarthy, A. Drury, B. Lahr, R.C. Barklie, M. in het Panhuis, J.N. Coleman, W.J. Blau; "Optimisation of the arc-discharge production of multi-walled carbon nanotubes", *Carbon* **40**, 923 (2002)

[37] M. Cadek, J.N. Coleman, K.P. Ryan, V. Nicolosi, G. Bister, A. Fonseca, J.B. Nagy, K. Szostak, F. Béguin, W.J. Blau; "Reinforcement of polymers with carbon nanotubes: The role of nanotube surface area" *Nano Lett.* **4**, 353 (2004)

[38] B. Stuart; "Polymer Analysis", *John Wiley & Sons*, Chichester (2002)

[39] V.A. Bershtein; "Differential Scanning Calorimetry of Polymers", *Ellis Horwood*, Chichester (1994)

[40] Quoted by J.-P. Salvetat-Delmotte, A. Rubio; "Mechanical properties of carbon nanotubes: a fiber digest for beginners", *Carbon* 40, 1729 (2002) [original quote by Gordon 1976]

[41] K.P. Menard; "Dynamic Mechanical Analysis Basics: Part 2. Thermoplastic Transitions and Properties", Perkin Elmer Application notes, PETech-91

[42] J.C. Velasco-Santos, A.L. Martínez-Hernández, F. Fisher, R. Ruoff, V.M. Castaño; "Dynamical–mechanical and thermal analysis of carbon nanotube/methyl-ethyl methacrylate nanocomposites", Phys. D: Appl. Phys. 36, 1423 (2003)

[43] D.W. Clegg, A.A. Collyer; "Mechanical properties of reinforced thermoplastics", Elsevier Applied Science, Essex (1986)

[44] H.L. Cox; "The elasticity and strength of paper and other fibrous materials", Brit. J. Appl. Phys. 3, 72 (1952)

[45] M. O'Regan, D.F. Akay, B. Meenan; "A comparison of Young's modulus predictions in fibre-reinforced-polyamide injection mouldings", Compos. Sci. Technol. **59,** 419 (1999)

[46] J. Sandler, M. S. P. Shaffer, P. Werner, V. Altstädt, M. v. Es, and A. H. Windle; "Carbon-nanofibre-reinforced poly(ether ether ketone) fibres", *J. Mater. Sci.* **38,** 2135 (2003)

[47] J. Sandler, P. Werner, M.S.P. Shaffer, V. Demchuk, V. Altstädt, A.H. Windle; "Carbon-nanofibre-reinforced poly(ether ether ketone) composites", *Composites: Part A-Applied Science and Manufacturing* **33,** 1033 (2002)

[48] J.K.W. Sandler, S. Pegel, M. Cadek, F. Gojny, M. v. Es, J. Lohmar, W.J. Blau, K. Schulte, A.H. Windle, M.S.P. Shaffer; "A comparative study of melt spun polyamide-12 fibres reinforced with carbon nanotubes and nanofibres", *Polymer* **45,** 2001 (2004)

[49] J.C. Halpin, S.W. Tsai, *Air Force Material Laboratory technical report*; ***AFML-TR-67-423*** (1967)

[50] P. K. Mallick; "Fibre-reinforced Composites", *Marcel Dekker*, New York (1993)

[51] D. Qian, E.C. Dickey, R. Andrews, T. Rantell; "Load transfer and deformation mechanisms in carbon nanotube-polystyrene composites", *Appl. Phys. Lett.* **76,** 2868 (2000)

[52] M. Cadek, J.N. Coleman, V. Barron, K. Hedicke, W.J. Blau; "Morphological and mechanical properties of carbon-nanotube-reinforced semi-crystalline and amorphous polymer composites", *Appl. Phys. Lett.* **81,** 5123 (2002)

[53] P.C. Painter, M.M. Coleman, J.L. Koenig; "The Theory of Vibrational Spectroscopy and its Application to Polymeric Materials", *John Wiley & Sons*, Chichester (1982)

[54] J.L. Koenig; "Spectroscopy of Polymers", *Elsevier*, Amsterdam (1999)

[55] H.P. Klug, L.E. Alexander, "X-Ray Diffraction Procedures For Polycrystalline and Amorphous Materials", *Wiley*, New York (1954)

[56] L.E. Alexander; "X-Ray Diffraction in Polymer Science", *Wiley*, London (1969)

[57] F.J. Baltá-Calleja, C.G. Vonk; "X-ray scattering of synthetic polymers", *Elsevier*, Oxford (1989)

CHAPTER THREE: SAMPLE PREPARATION AND EXPERIMENTAL METHODS

3.1 Introduction

This chapter specifies all aspects of sample preparation required to achieve high quality polymer-nanotube composites. Initial procedures to produce polymer solutions are outlined before progressing to the addition of carbon nanotubes. Parameters such as sonication time, sample bottle size, nanotube concentration, drop casting techniques and film drying will be listed. Data will be presented in later chapters to show that deviation from a well-defined combination of parameters results in poor nanotube dispersion. Furthermore, poor dispersion will be shown to limit the ability of nanotubes to promote polymer crystallisation and consequently the level of reinforcement in a composite. As with many processes for optimal sample preparation, while straightforward to follow, the composite formation is non-trivial and in particular the nanotube concentration range should be meticulously adhered to. In addition, the specific sample configuration for each experimental technique will be discussed along with useful instructions for handling the composites.

3.2 Solution processing

3.2.1 PmPV solution

PmPV powder was dissolved in toluene to form a solution with a concentration of 20 g/L. It should be noted that concentrations up to 30 g/L could be obtained before gelling occurred. The PmPV/Toluene sample bottle was placed in a beaker containing a small quantity of water and put into a 60 W sonic bath for two hours to ensure all polymer powder is dissolved. As the name suggests the sonic bath propagates sonic energy through water to break up any aggregates present in solution. Arc discharge produced soot, containing MWNT, was then added to the solution at a concentration of 12 g/L – this is 60 % of the polymer concentration and was determined to be an optimum concentration by Murphy et al[1] given the nanotube content of the arc generated soot. The nanotubes were dispersed using a high power (700 W) ultrasonic tip operated at 20 % so that 140 W was the applied power. The tip duration was 2 minutes followed by 2 hours in the bath before a final 2 minutes under the tip. Sonication by bath alone is insufficient to disperse nanotubes and in some cases a small quantity of tubes were observed to

precipitate out of solution in agreement with the reports of other groups[2]. In addition, the energy distribution within a sonic bath is inhomogeneous and therefore does not have high reproducibility[3] hence the importance of application of the sonic tip to complete the dispersion process. The composite solution was subsequently left to settle for 24 hrs to allow the sedimentation of non-nanotube impurities[4] before decantation to yield a pure MWNT–PmPV solution. Figure 3-1 shows the pure polymer on the left and the composite on the right. This composite solution was then blended with polymer solution (0 wt%) in the required ratios to yield nanotube mass fractions of approximately 1, 2, 4, 6, 8 wt%. The exact mass fractions were determined by thermogravimetric analysis (TGA) details of which will be specified in Chapter 4.

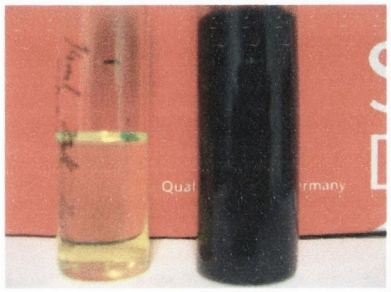

Figure 3-1: *Vials of PmPV (left) and nanotube composite (right) in a toluene solution.*

3.2.2 PVOH solution

PVOH was prepared at a concentration of 30 g/L with de-ionised (DI) water as the solvent. The PVOH powder required use of the sonic tip to ensure full solvation. The tip duration was 2 minutes followed by 2 hours in the bath before a final 2 minutes under the tip producing a transparent solution. A comprehensive range of nanotubes as detailed in Chapter 2 were then prepared for addition to PVOH solution. Composite solutions with the desired NT/polymer ratio were then prepared in 12 ml bottles with 10 ml of solution in each. The use of smaller bottles is critical and will be discussed in Chapter 5. The desired mass of nanotubes was then added to the PVOH solution and sonicated using 15 min tip, 2 hrs bath and 15 min tip to obtain a stable nanotube dispersion. The effect on nanotube length and polymer crystallinity of using these long tip sessions is investigated in Chapter 5. As with the PmPV composites, the solutions were left to settle for 24 hrs before decanting the stable nanotube suspension. A detailed description of the preparation process will now be presented in a stepwise fashion:

- Four bottles containing 25 ml of 30g/L **PVOH** in DI water were produced:
  750 mg PVOH powder was weighed into a 28 ml bottle, 25 ml DI water added
  Any gelling was crushed with a spatula to ensures dispersion of powder
  2 min tip – 2 hours bath – 2 min tip (2t-2b-2t)

- 23 ml of **0.5 wt% NT composite** was produced by weighing
  3.5 mg nanotube powder into a 28 ml bottle and add
  23 ml 30 g/L PVOH solution
  10t-2b-10t

- Composite transferred to two 12 ml bottles for more effective sonication.
  9mls composite in each
  Further 10 min tip.

- UV-Vis to establish NT content (discussed in detail in Section 3.10 below):
  Transferred 0.5 ml composite from either of the 12 bottles into a 7ml vial.
  Add 2.5 ml deionised water (1:5)
  1 min tip before immediate transfer into 1cm cuvette to obtain UV-Vis spectrum

- The two 12 ml bottles were placed on the settling bench until decantation after 24 hours

- Decanted both 12 ml bottles into 28 ml bottle – all mass fractions will be blended from this 0.5 wt% stock solution.
  2 min tip.

- UV-Vis of stock solution:
  Transferred 0.5 ml composite into a 7 ml vial.
  Add 2.5 ml deionised water (1:5)
  1 min tip before transfer into 1 cm cuvette and measurement of UV-Vis spectrum

- Transfer 5 ml of the stock composite into a 12 ml bottle – this is the 0.5 wt%

To make the 0.25 wt%:

Transfer 5 ml of the stock 28 ml composite into a 12 ml bottle.

Add 5 ml PVOH solution, 1 min under the tip

- Make the 0.125 wt%:

  Transfer 5 ml of the 0.25 wt% into a 12 ml bottle.

  Add 5 ml PVOH solution, 1 min under the tip

This was repeated as necessary to obtain the lowest dilution required at which point there will be 10 ml of the lowest mass fraction. 5 ml of this low concentration solution was transferred into a 12 ml bottle and the remainder was kept in reserve as a precaution in the event that a lower mass fraction was later required. At this point there was a collection of 12 ml bottles, each containing 5ml of the required mass fractions. *Before drop casting each bottle was given 5 minutes under the tip and left standing for 30 minutes prior to drop casting. This displaces any air trapped in the solution and gives time for the bubbles to rise to the surface where they form a foam.*

3.3 Drop casting

Robust free-standing thin films for TGA, DSC, DMTA, tensile tests and XRD were prepared by drop casting on Teflon discs with a diameter of 35 mm and a thickness of 12 mm. A thickness of 12 mm was used for ease of handling, in particular for gripping during the sanding process which involved successively sanding with 120, 600 and 1200 grit sandpaper. The final step with 1200 grit paper is critical as insufficient sanding leaves tracks on disc that trap air under the film when solution is dropped – this air will surface as unwanted bubbles in the film. After sanding, the discs were placed in a beaker of water and place in sonic bath for at 5 hr to remove dirt and Teflon particles produced during sanding. The discs were then dried with lint free tissue paper and placed in the oven using microscope slides for support as shown in Figure 3-2.

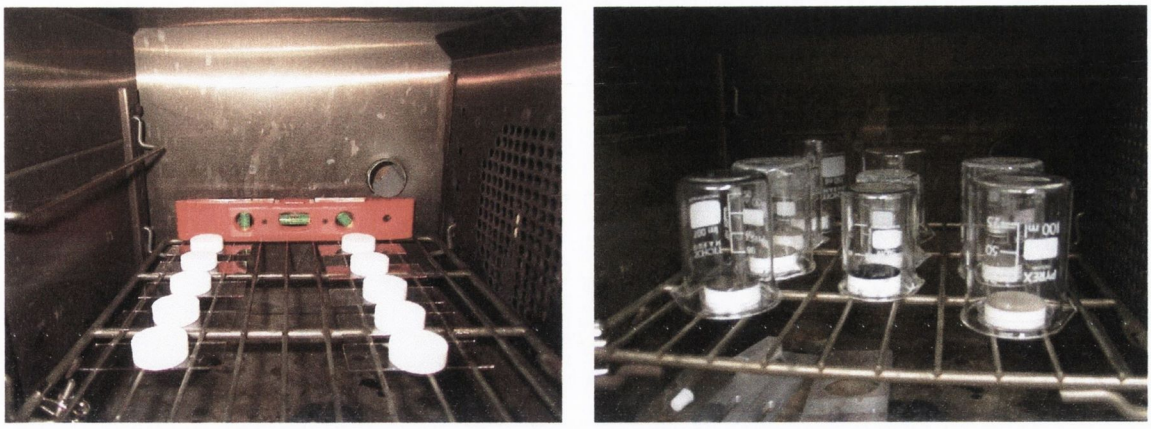

Figure 3-2: *Experimental setup for drop casting on teflon disks.*

Before drop casting, each bottle of solution was given 5 min under the tip and left to settle for 30 min to displace any trapped air. Each film comprised of 5 ml of solution deposited in 1 ml steps with fan assisted oven drying at 60 °C for 2 hours between layers. 60 °C was chosen to facilitate drying below the 70 °C glass transition of PVOH. A beaker was placed over each disk during drying to prevent any contamination. Each of the layers was deposited by placing the pipette on the surface of the disk or preceeding film and injecting the solution to swell the initial droplet as shown in Figure 3-3(a). This created an airtight seal to avoid inducing bubbles in the film. A thin glass pipette was used to smooth the film over the entire surface area of the disc ensuring that surface tension prevented the liquid flowing over the edge as shown in Figure 3-3(b).

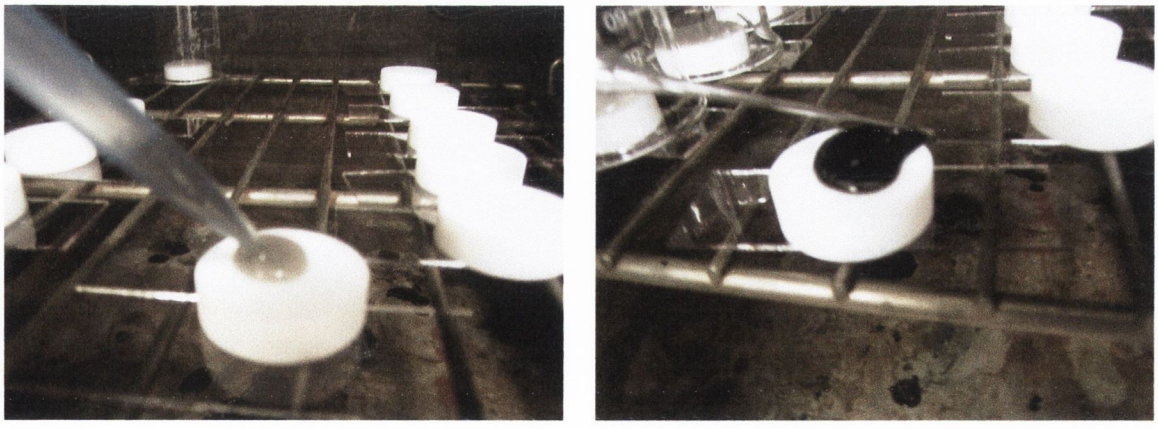

Figure 3-3(a): *Depositing solution.* ***(b)*** *Stretching solution to edge of disk.*

1.5 hrs after deposition of the fourth layer, the film was removed so that the small amount of remaining water gave some flexibility enabling peeling from the discs. This was achieved by lifting the edge with a sharp flat "Bohemian" razor blade and peeling the film

by hand while wearing protective gloves. These steps produced a film of 35 mm diameter with an average thickness of 59±9 μm at the centre and 250±50 μm at the edge. The films were then cut into strips 3±0.3 mm wide using the razor blade and a steel chopping block scored with parallel lines which acted as a template. Some DWNT strips are shown in Figure 3-4 with PVOH on the left followed by the composites from 0.03 to 0.5 wt%. Each film moving left to right contains double the nanotubes relative to its predecessor.

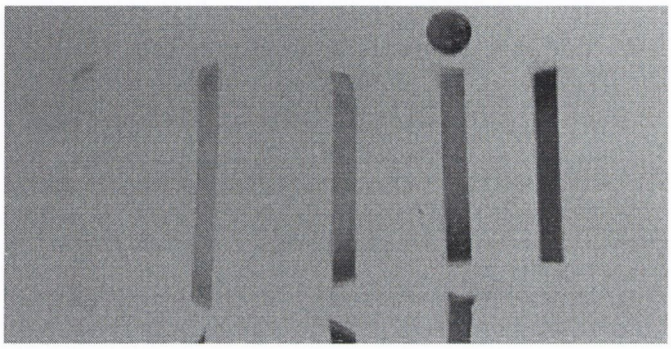

Figure 3-4: *PVOH and DWNT strips before testing. A punched disk is also shown. Moving from left to right: a neat polymer strip is transparent on the left while each of the adjacent composite films contains double the mass of nanotubes than its predeccessor.*

Note that a vacuum oven was tested but found unsuitable for two reasons: Firstly it promoted the formation of bubbles within the film and secondly the rapid removal of solvent reduced the time available for polymer crystallisation – a crucial point given that the later experiments on these films required the highest possible crystalline fraction for ease of detection.

In addition to free-standing films, thin films of PVOH composites were prepared on glass microscope slides to investigate the dispersion and size of aggregates in the samples. The slides were cleaned using water followed by acetone before spraying with nitrogen gas to eradicate any contaminants. 0.25 ml of each solution was dropped onto a glass microscope slide producing a film suitable for inspection with an optical microscope.

3.3.1 Alternative substrates

Chromed metal disks were also assessed as possible substrates for producing free-standing PVOH films. Figure 3-5 demonstrates that these films on metal were free of bubbles and would provide an adequate alternative to Teflon cast films. However, while

the drop cast films could be peeled off the metal relatively easily, Teflon was marginally superior and was the favoured substrate.

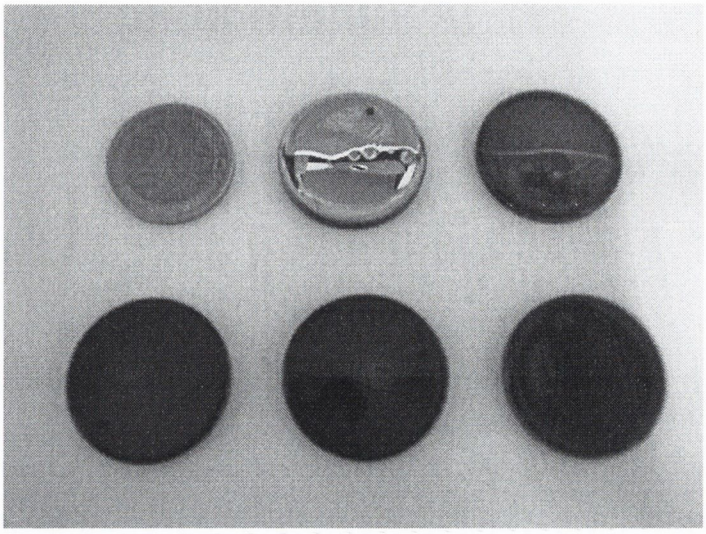

Figure 3-5: *PVOH films depsosited on chromed metal disks. A two Euro coin is included for scale, a PVOH film is to the right of the coin followed by composites with increasing nanotube content from left to right.*

3.4 Spin casting

Spin casting was required to produce thin films for photoluminescence studies of the luminescent polymer PmPV and the PmPV/ArcMWNT composites. 0.25 ml of solution was dropped on a Spectrosil B quartz substrate and immediately spun at 600 rpm using a Convac 2000 spin coater. Profilometry determined an average film thickness of 250 ± 20 nm. Profilometry is an optical technique where the surface of the film to be measured is scratched with a needle to create a groove. A low power laser source is then aimed at the sample and the difference in path length produces interference between the light reflected from the film surface and the bottom of the groove thus allowing calculation of the film thickness.

3.5 Thermogravimetric Analysis (TGA)

Polymer and polymer/nanotube composite disks 5.8 mm in diameter were pressed from the central regions of drop cast free standing films using a standard heavy duty paper punch. The disks were punched from the central regions as surface tension during drop casting creates a thicker profile for the film edge than is characteristic of the centre. When the disks are punched from the central regions of the films they have identical thickness so that their mass is also controlled to a value of 6 ± 0.3 mg. These disks fitted perfectly

into the platinum TGA sample pans giving precise control of the sample mass thus reducing experimental error. The integral balance on the TGA measured the exact sample mass. Both PmPV and PVOH composites were heated in air from 0 °C to 950 °C at a rate of 10 °C /min.

3.6 Differential Scanning Calorimetry

5.8 mm disks of were also pressed for the Differential Scanning Calorimetry (DSC) aluminium sample pans. Each disk was found to weigh 6 ± 0.3 mg and two disks were used in the calorimetry measurements. Samples were prepared by carefully placing the film disks into an aluminium sample pan in layers to ensure maximum thermal transfer through the entire sample. Flowing helium gas was employed to purge any remaining solvent in the sample. PmPV samples were heated from –90 °C to 170 °C at a rate of 40 °C/min and held at 170 °C for one minute to allow the system equilibrate before control cooling to –90 °C at 10 °C/min using a controlled liquid nitrogen feed. A hold step of one minute was applied at –90 °C before a second heating scan was implemented from –90 °C to 170 °C at 40 °C/min. The PmPV/Arc MWNT measurements were completed in one day to ensure a consistent baseline, which was obtained using an empty sample pan. A heat flow resolution of approximately 0.1 W/g was achieved with the instrument. Similarly, PVOH composites were tested so that all mass fractions of a particular nanotube type were ran on the same day. In addition, each of the PVOH composites received 1.5 hr drying at 60 °C in the oven immediately before the DSC scan. This eliminated the water peak that has caused problems in studies conducted by other groups[5].

The temperature program employed for PVOH was 0 °C to 220 °C at a rate of 40 °C/min and held at 220 °C for one minute to allow the system equilibrate before control cooling to 0 °C at 40 °C/min using liquid nitrogen. A hold step of one minute was applied at 0 °C before a second heating scan was implemented from 0 °C to 220 °C at 40 °C/min.

3.7 Tensile Testing

Tensile testing was conducted on a Zwick tensile tester, using a 100N cell for the best possible resolution. L_o was set at 10 mm and the 'flat specimen' programme option was selected. Tensile tests were primarily performed on PVOH composites but for completeness a PmPV and PmPV/Arc MWNT were investigated. Strips of free standing film were cut to the dimensions 20 (± 0.3) mm x 3 (± 0.3) mm x 0.05 (± 0.005) mm for PVOH while the PmPV films were thicker with an average thickness of 0.14 ± 0.02 mm.

Since PVOH is a water soluble polymer, atmospheric water absorption is known to effect the mechanical properties of the film[6,7]. A detailed investigation of the effects of water absorption from the atmosphere will be reported in Chapter 5. To optimise reproducibility the following procedure was followed: 5 days before testing, all films were dried for 5 hours and subsequently stored using unsealed Petri dishes in the laboratory until measurements commenced. Before testing the sample dimensions are recorded using a low torque digital micrometer, clamped and the tensile test is activated as shown in Figure 3-6. The sample dimensions allow the computer to generate the force per cross section area of the sample, termed the stress, and plot this against elongation (strain).

Figure 3-6: *Sample undergoing Zwick tensile test.*

3.8 Dynamic Mechanical Thermal Analysis (DMTA)

DMTA was performed on free-standing film strips from the same film as those subjected to tensile and calorimetry experiments. This enabled direct comparison between the two techniques. The Perkin Elmer Diamond DMTA was operated in tension mode with nitrogen as the furnace purge gas and liquid nitrogen for controlled cooling. For PmPV

samples a ramp rate of 2 °C/min from 0 to 140 °C was applied with a 1 s sample rate and 1 Hz frequency. PVOH was tested with a ramp rate of 2 °C from 0 to 220 °C with a 1 s sample rate and 1 Hz frequency.

3.9 Microscopy: Aggregation study and nanotube imaging

Optical, Transmission Electron and Scanning Electron Microscopy were used to image the composites. A standard optical microscope interfaced to a PC was used in a study of large-scale aggregation for initial assessment of nanotube dispersion in the composite. Dispersions of N_Thick, N_Vthin and N_DWNT were comprehensively studied before and after drying. To investigate the initial aggregation immediately after dropping, wet films were prepared and inspected. These were viewed by placing a thin coverslip on top and inspecting immediately with the microscope. Aggregation attributable to the conditions used to dry the films was also studied using at atmospheric pressure and under vacuum using a vacuum oven. All of these films were dried for 24 hrs. Drying temperature was also varied to study the temperature effects on aggregate formation.

3.9.1 Optical microscopy

Thin films were inspected with an optical microscope using a 4x lens. Slides were placed under the lens on a moving platform, and the image was focused by varying the distance between the platform and the lens. With the image in focus three snapshots of each film were recorded at different locations on the film to allow calculation of an overall aggregate dispersion representative of the entire area of the film. Pictures of the film were recorded using a computer interfaced CCD camera attached to the microscope. Bitmap images (1616nm x 1212nm) were analysed using 'Image Tool' using a 4x4 grid system that was manually superimposed on the original image. The number of observable aggregates were counted for each section on the grid and diameters of aggregates were recorded. Image resolution was dictated by the resolution of the camera with each pixel being equivalent to approximately 2.5 um. Two of the dried films were also inspected on an additional microscope with a more powerful 20x lens to establish the limitations of the lower magnification used to analyse the films. The 4x magnification was found to be sufficient since no improvement in resolution or additional features were observable with the 20x lens.

3.9.2 Transmission electron microscopy (TEM)

A formvar coated copper grid was half dipped into a dilute composite solution to prepare samples for TEM using a Hitachi H-7000 TEM. This enabled polymer coated nanotubes protruding from the film edge to be observed. This technique was used for both PmPV and PVOH based composites.

3.9.3 Scanning electron microscopy (SEM)

SEM was used to examine PVOH composites. Strips of free-standing film were dipped in liquid nitrogen and then snapped at the centre. This technique freezes the polymer matrix which then breaks cleanly with nanotubes protruding from the fracture surface. The samples were then coated in gold and imaged using the backscatter mode of the SEM. The number of tubes per unit fracture surface area, coupled with the nanotube pull out length, can be used to assess the quality of the filler dispersion within the matrix and calculate the strength of the polymer/nanotube interface[8].

3.10 Ultraviolet – visible spectroscopy (UV-Vis)

UV-Vis absorption spectra of the PmPV composites were obtained using thin films spun cast on quartz substrates. A clean quartz substrate was used as the reference material. The samples were scanned over the full spectral range (190 to 1100 nm) of the Shimadzu UV1601-PC spectrophotometer used in this work. This instrument has a double beam, direct ratio photometric measuring system using a dynode feedback method. It has a photometric range of -4 to ~5 in Absorbance, 0 to ~99.99% in Transmittance. It employs a 50W halogen lamp and a Deuterium lamp. Spectra are dispersed by a Czerny-Turner monochrometer with a high performance blazed holographic grating, and detected by an R-928 photomultiplier.

Many of the nanotubes used in the PVOH composites fully decompose below 700 °C so that the nanotube and polymer decomposition peaks overlap. These peaks cannot be deconvoluted as the each element of the composite is expected to catalyse the decomposition of the other. This implies that TGA data could not be used to evaluate the nanotube content. It will be important in chapter 6, where the concentration of a range of nanotube types will be under investigation, to know the approximate volume of nanotubes

in solution. UV-Vis data will therefore be used to monitor the change in absorbance as an indicator of light scattered from the composite solutions before and after decantation. 0.5 wt% nanotubes were rigorously dispersed in the PVOH solution, as outlined in Section 3-3 above, yielding a "stock" solution. 0.5 ml of this stock solution was quickly transferred into a 7 ml bottle to avoid effects of any fast sedimentation processes that may occur. This 0.5 wt% solution has too high an absorption to obtain a suitable signal. In order to reduce the absorption, 2.5 ml of deionised water is added and given 1 min under the tip before immediate transfer to a 1 cm quartz cuvette and an absorption spectrum is obtained. After 24 hours the stock solution was decanted and 0.5 ml was taken and blended as described above to produce another absorption spectrum. The ratio of absorption at 800 nm for the pre- and post decant solution was then used as an indicator of nanotube or carbonaceous material loss during settling.

3.11 Photoluminescence

Photoluminescence measurements were taken by exciting a thin film of the composite in air using an Ultra Violet (UV) diode with peak emission at 373 nm and a full width half maximum of 12 nm. The thin films were spun on quartz disks at 600 rpm. Profilometry determined an average film thickness of 250 ± 20 nm. The PL spectra were collected with a computer interfaced Andor CCD camera coupled to an Oriel spectrometer as shown in Figure 3-7. A shutter opened immediately prior to the acquisition of the spectra to prevent degradation of the film by the excitation source thus ensuring the accuracy of the initial PL intensity recorded.

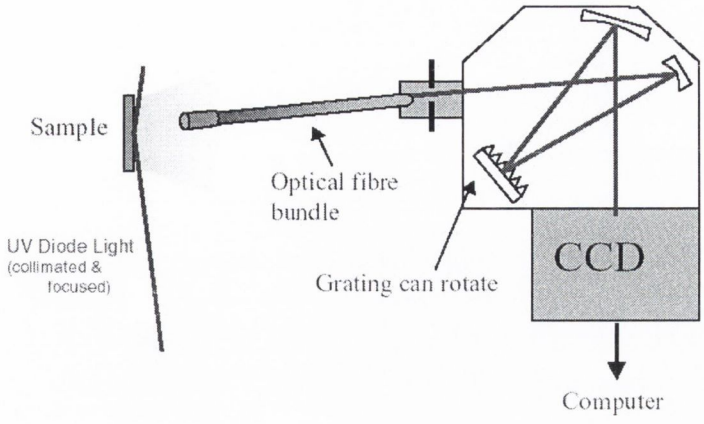

Figure 3-7: *PL experimental setup.*

3.12 Fourier transform infrared spectroscopy (FTIR)

Thin films of PmPV composite were spun cast on potassium bromide (KBr) substrates which are transparent in the IR spectrum. A Nicolet Nexus FTIR spectrometer was used to measure the samples. FTIR was not carried out on the PVOH composites as water will dissolve the KBr substrates. The significant data gathered from the other techniques described above was such that the absence of FTIR is not an obstacle to comprehensively characterising the PVOH samples.

3.13 X-Ray diffraction

A glass substrate was placed in the XRD chamber to support the free-standing film. A small section of double sided tape (1 mm x 1 mm approx.) was used to fix the film. A baseline of the tape and glass was taken to evaluate their contribution to the XRD scattering. Each film was then carefully pressed onto the tape without moving the glass and tape to ensure the baseline remained valid in case of any scattering off the substrate. The films were scanned through 2θ values ranging from 2 to 30°.

3.14 Crosslinking experiment

3.14.1 Introduction

Residual carboxylic acid groups (-COOH) are known to exist on carbon nanotubes as a result of the acid purification process[9,10]. A final experiment was carried out in an attempt

to produce a condensation reaction[11] between these –COOH groups and the OH group of the PVOH chains. It was hoped by dispersing OH nanotubes in PVOH under acidic conditions a suitable reaction could be achieved in a similar way to a paper by Gousse and Gandini[12] where a condensation reaction between PVOH and 2-furaldehyde was used to synthesise the corresponding acetal. The reaction is shown in Figure 3-8.

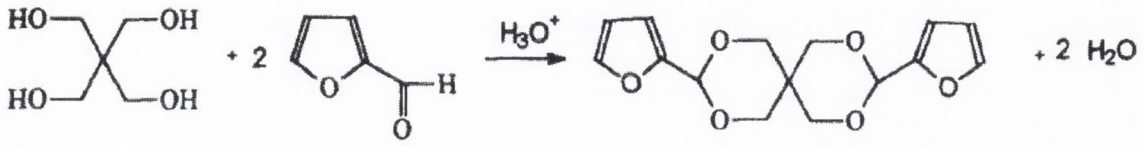

Figure 3-8: *Reaction to crosslink OH groups*[12].

3.14.2 Experimental

Four bottles containing 28 ml of PVOH/de-ionised water solution (30 g/L) were prepared as described earlier. One bottle was used as the reference while 1 wt% of OH_MWNT were added to another. 1 wt% of annealed N_Thin were added to the remaining two bottles. These four bottles were given 1 minute under the sonic tip then transferred to four 50 ml conical flasks. The flasks were securely clamped in a sonic bath as shown in Figure 3-9(a). Sufficient *p*-toluene sulfonic acid/water solution was slowly added to the PVOH solution to lower the pH from 6 to 1. It was observed that an average of 1.3 ml of 1 Molar *p*-toluene sulfonic acid/water solution was required to achieve this. Litmus paper was used to monitor the pH since extreme acidic conditions can damage highly sensitive electrical pH meters. Similarly the pH of the OH_MWNT and one of the annealed N_Thin solutions was decreased to 1 with the addition of acid. The solutions were then left for 9 hours in the 100 Watt sonic bath heated at 45 °C after which they were transferred to 28 ml bottles and placed on the settling bench for 24 hours. The stock solutions are shown in Figure 3-9(b). After decantation the acidic samples were blended with the acidic PVOH to produce a lower nanotube concentration of 0.5 wt% in addition to the 1 wt% sample.

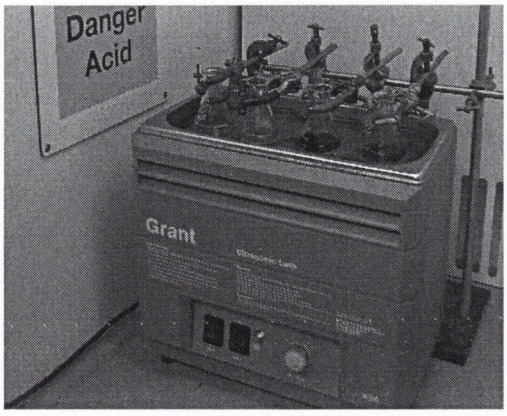

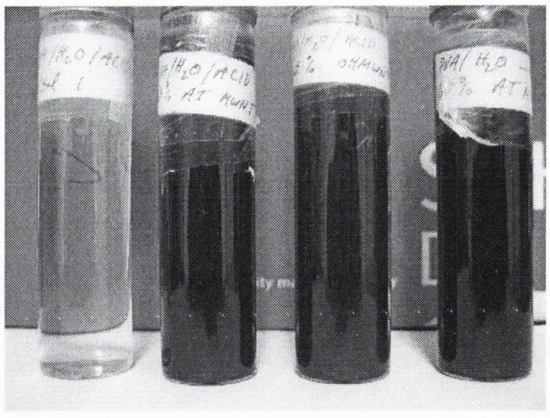

Figure 3-9(a): *Acid reaction experimental setup.* ***(b)*** *Stock PVOH and 1 wt% solutions.*

Free-standing composite films were produced and cut as described in Section 3-3. Given the acidic nature of these films the use of protective gloves is emphasised. Tensile testing was used to investigate the mechanical performance of the films.

3.15 References

[1] R. Murphy, J.N. Coleman, M. Cadek, B. McCarthy, M. Bent, A. Drury, R.C. Barklie, W.J. Blau; "High-yield, nondestructive purification and quantification method for multiwalled carbon nanotubes", *J. Phys. Chem. B* **106,** 3087 (2002)

[2] K. El-Hami, K. Matsushige; "Covering single walled carbon nanotubes by the poly(VDF-co-TrFE) copolymer", *Chemical Physics Letters* **368**, 168 (2003)

[3] S. Niyogi, M.A. Hamon, D.E. Perea, C.B. Kang, B. Zhao, S.K. Pal, A.E. Wyant, M.E. Itkis, R.C. Haddon; "Ultrasonic Dispersions of Single-Walled Carbon Nanotubes", *J. Phys. Chem. B* **107**, 8799 (2003)

[4] J.N. Coleman, D.F. O'Brien, A.B. Dalton, B. McCarthy, B. Lahr, A. Drury, R.C. Barklie, W.J. Blau; "Measurement of nanotube content in pyrolytically generated carbon soot", *Chemical Communications* **20**, 2001 (2000).

[5] O. Probst, E.M. Moore, D.E. Resasco, B.P. Grady; "Nucleation of polyvinyl alcohol crystallization by single-walled carbon nanotubes", *Polymer* **45**, 4437 (2004)

[6] K.E. Strawhecker, E. Manias; "Structure and Properties of Poly(vinyl alcohol)/Na^+ Montmorillonite Nanocomposites", *Chem. Mater.* **12**, 2943 (2000)

[7] O. Probst, E.M. Moore, D.E. Resasco, B.P. Grady; "Nucleation of polyvinyl alcohol crystallization by single-walled carbon nanotubes", *Polymer* **45**, 4437 (2004)

[8] J.N. Coleman, M. Cadek, R. Blake, V. Nicolosi, K.P. Ryan, F. Liégeois, A. Fonseca, J.B. Nagy, Y. Gounko, W.J. Blau; "High performance nanotube reinforced plastics: The mechanism of strength increase", *Adv. Funct. Mat.* **14**, 791 (2004)

[9] A. Kuznetsova, I. Popova, J.T. Yates, M.J. Bronikowski, C.B. Huffman, J. Liu, R.E. Smalley, H.H. Hwu, J.G. Chen; "Oxygen-Containing functional groups on single-wall carbon nanotubes: NEXAFS and vibrational spectroscopic studies", *J. Am. Chem. Soc.* **123**, 10699 (2001)

[10] H. Ago, Th. Kugler, F. Cacialli, K. Petritsch, R.H. Friend, W.R. Salaneck, Y. Ono, T. Yamabe, K. Tanaka; "Workfunction of purified and oxidised carbon nanotubes", *Synth. Met.* **103**, 2494 (1999)

[11] P. Atkins, L. Jones; "Chemistry: Molecules matter and change", *Freeman*, 3rd Ed., New York (1997)

[12] C. Gousse, A. Gandini; "Acetalization of polyvinyl alcohol with furfural", *Eur. Polym. J.* **33**, 667 (1997)

CHAPTER FOUR: PmPV COMPOSITES

4.1 Introduction

Since 1998 a number of publications have demonstrated the formation of crystalline polymer coatings at the nanotube surface in polymer – carbon nanotube composites[1,2,3,4,5,6]. In our group, TEM studies by McCarthy et al identified nanotubes coated with the semi-conjugated polymer poly(m-phenylenevinylene-co-2,5-dioctyloxy-p-phenylenevinylene) (PmPV). For this reason PmPV was chosen as an ideal candidate for characterising the nature of polymeric coating of carbon nanotubes. A typical TEM is shown in Figure 4-1[1]

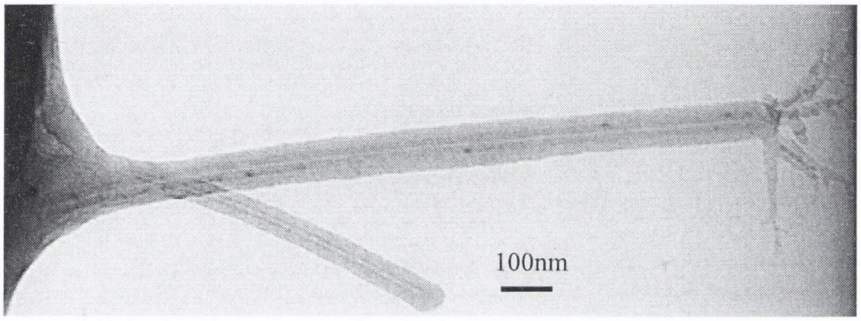

Figure 4-1: *TEM of PmPV/Arc MWNT composite*[1].

This chapter reports on the doping of PmPV with arc produced multiwalled carbon nanotubes (ArcMWNT). The composite is first characterised using TGA to evaluate the nanotube content while XRD and DSC are used to examine sample morphology. Changes in the fingerprint region of FTIR data identify alterations in polymer chain conformation when nanotubes are present while photoluminescence combined with UV-visible absorption techniques are employed to measure the optical properties. These crystalline and optical properties are consistent with a nanotube induced increase in polymer crystallinity. A model that assumes the crystalline polymer exists at the polymer/nanotube interface is introduced and is in excellent agreement with the observed photoluminescence extinction.

4.2 Background literature

Polymer coating of nanotubes is not unique to PmPV but the long-term stability observed for PmPV/arc MWNT composite solutions is not widely reported for the other polymers.

Investigation of the crystallisation of the protein streptavidin around carbon nanotoubes is the subject of some of the most interesting reports[2,4,6]. This streptavidin interaction has been used to create a prototype sensor by Star et al[7]. The sensor comprises of a nanotube coated with a polyethylene imine (PEI)/polyethylene glycol (PEG) polymer blend which has been dipped in Biotin which acts as the sensing element. If the biotin comes in contact with streptavidin a detectable change in NT conductivity occurs.

Polycarbonate has also been observed to coat MWNT. A clearly observable polymer sheath was identified at the fracture surface of a composite by SEM[4]. Other studies have focused on Polypropylene (PP)/Carbon nanotube composites[8,9,10]. In those studies no direct evidence of PP coating of nanotubes has been observed but DSC measurements have verified that CNT increase the rate of polymer crystallisation and will be useful for comparison purposes later in this chapter.

Results presented in this report show that the presence of MWNT in composite films increases PmPV crystallinity suggesting that crystallisation at the polymer-nanotube interface is the mechanism facilitating the polymer-MWNT interaction that enables the non-destructive purification method reported by Murphy et al[11]. The benefits of understanding the effect of nanotubes on polymer systems include the tailoring of the optical and mechanical properties of composites for specific electronic or reinforcement applications. Additionally, development of non-destructive purification methods may achieve the ultimate goal of extracting nanotubes with a specific chirality from arc generated carbon soot[12,13].

4.3 Thermogravimetric Analysis

Thermogravimetric analysis (TGA) was used to determine the exact nanotube mass fractions for the composite samples discussed in Section 3.2 using a Perkin Elmer Pyris 1 TGA. For each mass fraction ~10 mg of free-standing film was heated from 20 °C to 1000 °C in air at a rate of 10 °C/min. By integrating the nanotube peak (~830 °C) of the derivative curve, shown in the TGA oxidation data of Figure 4-2, the exact mass fractions were determined to be 0, 0.7, 1.4, 3.1, 4.6, 7.6 wt%.

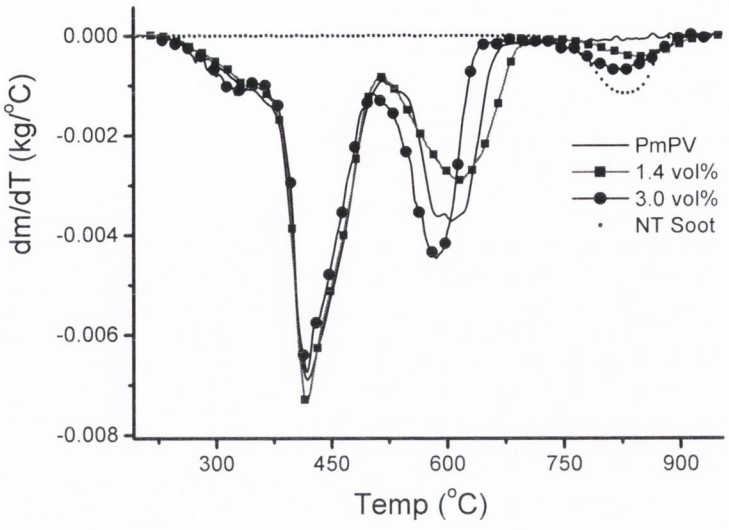

Figure 4-2: *Derivative of TGA data for the ArcMWNT, PmPV, 1.4 and 3.0 vol% films.*

Mass fractions, m_f, were transformed into volume fractions, v_f, of 0 (pure polymer film), 0.4, 0.7, 1.4, 3 and 4.7 vol% respectively using Equation 4-1.

$$v_F = \frac{1}{1 + \frac{\rho_{nt}}{\rho_p}\left(\frac{1 - m_f}{m_f}\right)}$$

Equation 4-1

ρ_{nt}, the density for perfectly graphitised MWNTs, was assumed to be 2.16 g/cm^3 in comparison with graphite in accordance with the work of Qian et al[14]. A polymer density, ρ_p, of 1.3 g/cm^3 was chosen for PmPV since the exact density value for PmPV is unknown and 1.3 g/cm^3 is a typical value for organic polymers[15,16]. For the remainder of this chapter the nanotube content will be quoted in volume fraction.

In addition to the high temperature nanotube decomposition three other transitions at 330 °C, 420 °C and approximately 610 °C are observable in Figure 4-2. Taking average bond dissociation energies[17] into account and the number of C-O, C-H, C-C and C=C bonds present, assignments can be suggested for the transitions as follows: The lowest average bond dissociation energy of 350 kJ/mol is attributable to the C-O bond. Therefore the shoulder at 330 °C is consistent with decomposition of the sidechain end groups. This is expected to be followed by decomposition of the C-C bonds which also

have an average bond dissociation energy of 350 kJ/mol. The C-H bonds have a value of 410 kJ/mol while the C=C bonds of the vinylene and phenyl groups require approximately double the energy of the single bond to achieve decomposition and are therefore the last structures to dissociate. This hypothesis is consistent with the ratio of partial molecular weights compared to the ratio of the area under the TGA peaks. Thus the shoulder at 330 °C and peak at 420 °C are attributable to sidechain decomposition. While no significant change is observed for the polymer sidechain peak with the addition of nanotubes, the onset of decomposition for both the vinylene and phenyl (610 °C) groups is observed to decrease by approximately 30 °C for the 3 vol% composite relative to the pristine PmPV curve. This suggests the polymer backbone conformation is altered by the presence of nanotubes. The TGA data confirms that nanotube thermal conductivity[18] is not a dominant factor in the decomposition of the composite since the PmPV sidechain peaks are not shifted to lower temperatures. Photoluminescence degradation results will be presented later in this chapter that identify a change in oxygen permeability of the sample upon introduction of nanotubes. Such changes in gas permeability, as a result of a change in polymer morphology, may also contribute to the lower temperature thermal degradation of the polymer backbone as observed in the composite samples. To further investigate the change in polymer conformation suggested by the TGA results, crystallinity studies were implemented and will now be discussed.

4.4 X-Ray Diffraction Studies (XRD)

Wide-angle XRD data in the 2θ range of 2° to 10° was recorded for the pristine polymer and the 4.7% composite thin films, as shown in Figure 4-3. In the case of the semicrystalline PmPV, wide angle X-Ray scattering (WAXS) probes the lamellar crystals and determines the periodicity of the polymer chains which form the lamella. The scattering peaks can therefore be used to calculate the polymer chain spacing within a crystalline domain.

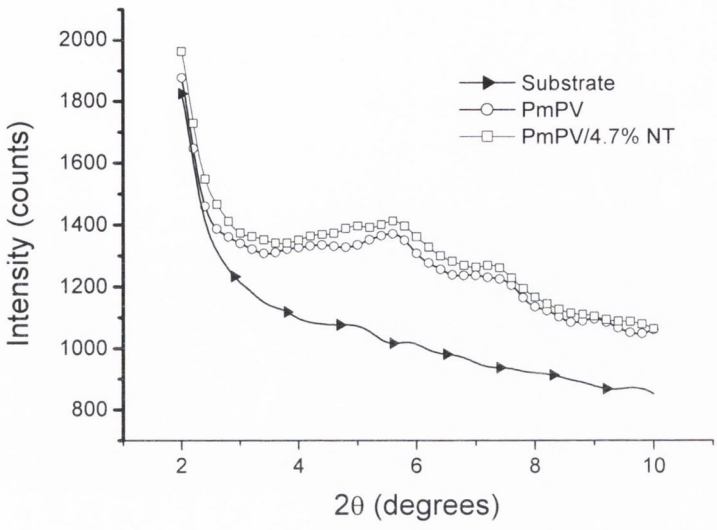

Figure 4-3: *2° to 10° WAXS of substrate PmPV and 4.7% Arc_MWNT composite.*

The wide angle X-Ray scattering (WAXS) in the 2θ range of 2° to 10° identifies two polymer peaks at 5.56° and 6.96°. These peaks are small in magnitude as expected from the low inherent crystallinity of PmPV[19]. Although no shift is observed in the polymer peaks with the introduction of nanotubes, the scattered intensity is observed to increase for the 4.7% Arc_MWNT sample. The 2θ values agree well with XRD studies carried out by Resel et al[20] on solution cast films of a PmPV like polymer where a peak was observed at 5.5°. This peak was attributed to scattering between PPV backbones separated by straight extended octoxy sidegroups. The co-polymer used in those studies is shown in Figure 4-4.

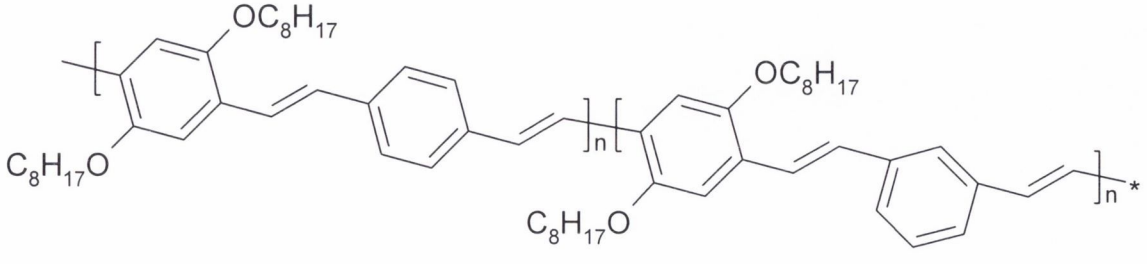

Figure 4-4: *Co-polymer similar to PmPV with a known crystallinity of 20%[20].*

The PmPV WAXS data over the 10° to 30° range exhibits a polymer peak at 23.52° as shown in Figure 4-5.

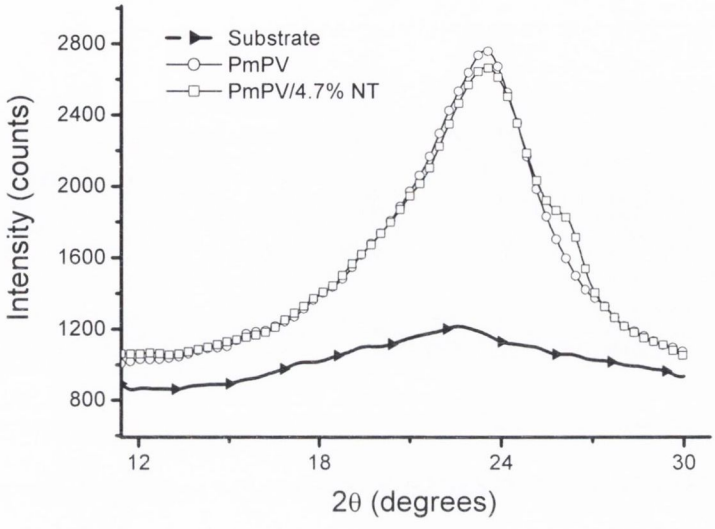

Figure 4-5: *10° to 30° WAXS of substrate, PmPV and 4.7% Arc_MWNT composite.*

This agrees well with a peak observed at 23.2° by Resel[20] who calculated a corresponding *d* value of 3.8 Å which is typical for the closest spacing between two PPV backbones. The intensity of the peak remains approximately the same upon addition of nanotube and a shoulder appears at 26.20°. A peak at this value is characteristic of ArcMWNT[21,22,23] as shown in Figure 4-6 which has been reproduced from Liu et al.

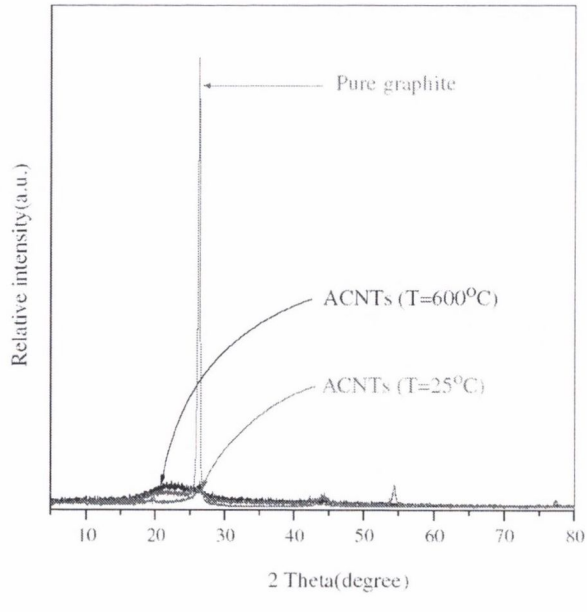

Figure 4-6: *XRD of pure graphite and soot containing carbon nanotubes produced by arc discharge of graphite. Furnace temperatures of 25 °C and 600 °C were used in this work by Liu et al*[21].

In summary, the small increase in intensity observed for the two polymer peaks at 5.56° and 6.96° suggested some morphological changes in the samples but no significant change in the polymer morphology could be identified using WAXS to probe the polymer/nanotube composite. Another useful X-Ray technique, unobtainable for the work presented here, is small angle X-Ray scattering (SAXS) which uses smaller angles to probe over longer length scales and therefore is more suited to identifying the periodicity of the crystal domains within an amorphous matrix – with SAXS it is the entire lamellar crystal that scatters while with WAXS it is the individual lamella of the crystal itself that scatters. SAXS is the preferred technique when assessing the crystallinity of semi-crystalline polymer but the intensity of WAXS scattering peaks was expected to be sufficient to identify any increase in the fraction of crystalline polymer. The failure of to identify an increase in crystallinity by WAXS contrasted to the success of the differential scanning calorimetry (DSC) technique which did identify nanotube induced changes in polymer morphology, those results will be presented in the next section. Given that the penetration depth of X-Rays is several millimetres[24] even at relatively small angles, the minimum film thickness (t) required to ensure the deeper layers of the sample contribute to the diffraction peak intensity is given by Equation 4-2.

$$t \geq \frac{2}{\mu}\sin\theta \qquad \textit{Equation 4-2}$$

Where θ is the Bragg angle and μ is the X-Ray absorption coefficient. μ is approximately 3.9 cm^{-1} for hydrocarbon solid polymers. Thus the sample thickness of approximately 50 μm was insufficient to accumulate the maximum possible scattering intensity and is one explanation for the failure to detect changes in polymer morphology in the composite. Increasing the film thickness would have necessitated drop casting more layers which was impractical due to solvent effects which caused blisters in the films when large numbers of layers were deposited. A second possibility is that the thin film allowed the glass substrate to contribute the broad background present in the data of Figures 4-3 and 4-4. The background is significant since the DSC results will show that the semi-crystalline polymer has broad melt peaks which would appear as broad scattering peaks in X-Ray experiments. Therefore any broad scattering peaks appearing in the composite may be masked by the background. DSC does not have the complication of a substrate contribution or the film thickness issues associated with XRD. It is more suitable for

determining the crystallinity of our samples and is a well-accepted technique for determining polymer crystallinity.

4.5 Differential Scanning Calorimetry

It has previously been determined that PmPV is a mainly amorphous polymer containing some crystalline regions[19] and is referred to as a semi-crystalline polymer. This makes it an ideal material to probe how nanotubes interact or influence crystallisation in conjugated polymer systems. In order to further investigate the local polymer crystallinity as templated by the nanotube, DSC measurements were carried out on all samples.

Traditionally the initial heat of a heat-cool-heat cycle is used to eliminate the thermal history of a sample and the second heat step is accepted as the true melting characteristic of the sample[25]. Other factors to be considered include annealing during sample preparation – such treatment can promote high temperature crystallisation while decreasing the total crystallinity[26]. However, in our case all samples were simultaneously prepared under the same environmental conditions ensuring an identical thermal history for each. Therefore the first heat provides vital information about polymer crystallisation that has occured in the composite solution and/or during film drying. The first heating step of the polymer powder, polymer film and composites are shown in Figure 4-7.

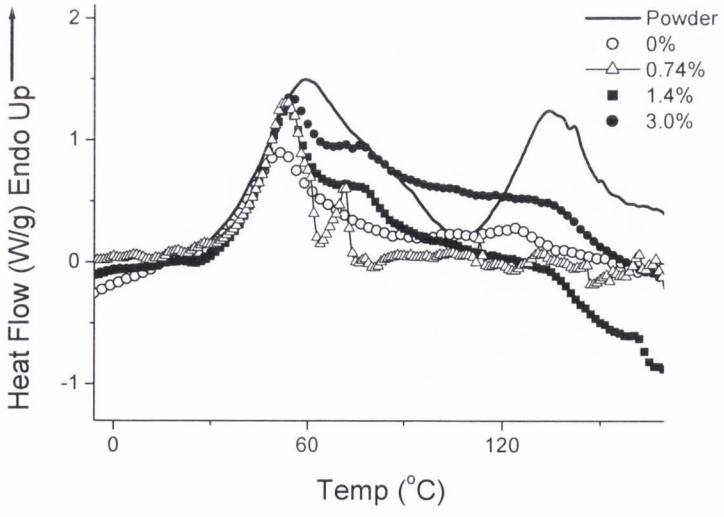

Figure 4-7: *DSC results obtained from the first heat scan.*

As with any DSC curve, transitions must be assessed with the three main transitions in mind – glass transition, crystallisation peak, melting peak. The first peak observed in the powder curve of Figure 4-7 was initially assessed as a possible glass transition before ruling it out for the following reasons: The curve almost returns to the baseline at ~110 °C: if this was a glass transition a clear shift in the baseline should be observed. In addition, quench cooling and a subsequent 20 °C reheat did not display a glass transition. Such rapid cooling will "freeze" the molecular motion at any point of glass transition so that a subsequent heat scan will produce a distinct glass transition corresponding to the reactivation of molecular mobility[26]. PmPV did not exhibit a glass transition under these conditions verifying that both peaks in the powder trace are melt peaks.

PmPV powder exhibits two broad peaks at 59 °C and 134 °C verifying that PmPV is a semi-crystalline polymer with ordered domains embedded in an amorphous matrix. This is expected due to disorder introduced by the bulky octyloxy sidechains in agreement with results by Mikroyannidis[27] for a PPV derivative where highly phenylated sidegroups were observed to impede crystallisation. This low crystallinity is confirmed by the small magnitude of the melt peaks observed in the DSC measurements. Since the melt peaks are broad in nature the melt temperature (T_m) is taken to be the maximum of the endothermal peak in accordance with convention.

Multiple melt peaks are common in systems where transitions occur from one crystallographic conformation to another before the melt occurs, an example of which is poly(p-xylylene)[26]. Systems containing multiple crystal sizes or crystals of varying structure also result in a number of endothermic peaks[26] suggesting that PmPV powder has a complicated morphology as expected given that a broad distribution of molecular weights are present in the polymer, as confirmed by its high polydispersivity of 5.5[19].

The composite film contains a narrower distribution of crystal sizes, which is evident from the single pronounced peak at 51 °C, while a small quantity of crystals that deviate in size from the main distribution result in a broad shoulder terminating at 158 °C. Enthalpy (H) values, shown in Table 4-1 at the end of this section, are calculated from the area under the melting curve and show a significant decrease in crystallinity for the polymer film relative to the powder suggesting that a fraction of the crystals formed

during synthesis are destroyed or reduced in size during the solvation process. Any tiny crystals that remain in solution are expected to exist as aggregates and act to nucleate further crystal growth upon drying.

X-Ray Diffraction (XRD) studies carried out by Resel et al[20] on solution cast films of a PmPV like polymer give crystallinity of approximately 20 %. The copolymer used in those studies has previously been shown in Figure 4-4. Thus, a crystallinity of 20 % is tentatively assumed for pure PmPV in order to transform from enthalpy to crystallinity. The value of 20% is reasonable given that the enthalpy of melting for our PmPV was measured to be 20 J/g and the enthalpy of melting for theoretically 100% crystalline organic polymers is in excess of 100 J/g. Poly (vinyl alcohol), for example, has a theoretical value of 138.6 J/g[28] for a 100% crystalline sample. Enthalpy (*H*) values were calculated by numerical integration between 10 °C and 160 °C for all samples, and normalised to sample mass. This was used to transform enthalpy of melting into crystallinity for all our samples using Equation 4-3 [26].

$$\chi = 0.2 \times \frac{\Delta H_{unknown}}{\Delta H_{20\% crystal}} \qquad \textit{Equation 4-3}$$

The error in the enthalpy is a function of the quality of the baseline for each individual DSC run. From sample to sample the curvature of the baseline deviates slightly with the result that it is often difficult to accurately pick the range over which the peak area should be calculated. This was particularly evident for the 1.4 and 3 vol% samples and is responsible for the large error bars attributable to the % crystallinity values.

A significant increase in the polymer film peak at 51 °C is observed upon introduction of the MWNT and a new feature appears at 73 °C that increases with increasing mass fraction. The total polymer crystallinity as a function of nanotube volume fraction is shown in Figure 4-8.

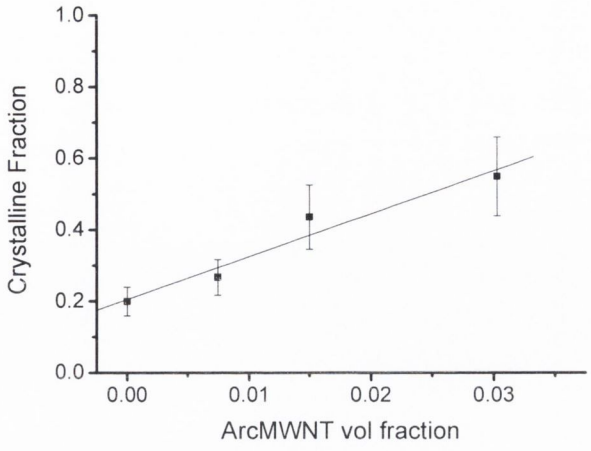

Figure 4-8: Plot of crystalline fraction (χ) as a function of ArcMWNT volume fraction (v_f).

This clearly shows a linear increase in crystallinity from 20% in the pure polymer to approximately 56 % in the 3 vol% composite sample. This suggests that each nanotube is coated with a crystalline layer of average thickness b as described before. As the volume fraction (v_f) is increased, more nanotubes are introduced and hence a larger fraction of the polymer is crystalline. Assuming that each nanotube of radius r_{nt} is coated we can derive a simple equation, Equation 4-4, to describe the crystallinity as a function of v_f:

$$\frac{d\chi}{dv_f} \cong 2\frac{b}{r_{nt}} + \left(\frac{b}{r_{nt}}\right)^2 \qquad \textit{Equation 4-4}$$

Fitting this equation to the data in Figure 4-8 gives a value of 25 nm for b in good agreement with the values from both TEM and photoluminescence spectroscopy. However, it must be noted that the values of χ and b depend greatly on the assignment of a crystallinity of 20% to the pure polymer reference film as discussed above. While 20% is a reasonable value, it could not be experimentally proven for our sample so that large error bars must be associated with the final values. To illustrate this point more clearly, if a lower bound crystallinity of 10% was assumed for the neat polymer film this would result in an increase in crystallinity to 28.8% at 3 vol% ArcMWNT. Since the use of 20% crystallinity as a reference value is essential scaling the enthalpy values, the actual proportional increase in crystallinity is independent of the % crystallinity values. In other

words, the crystallinity of a PmPV film doped with 3 vol% ArcMWNT is 2.8 times that of a pure polymer film. However, a change in slope will occur in Figure 4-8 depending on the scaling factor used. Thus a lower reference crystallinity, such as 10%, would revise down the value of *b*, the crystalline layer thickness to 15 nm. 10% is an extreme lower bound for the crystallinity given the typical enthalpy of melting discussed above for organic polymers and thus can be used to give a realistic error for *b*. The value of 25 nm is consistent with the TEM and photoluminescence results which will be presented in Section 4-6 showing there is merit in implementing the DSC analysis with reference to the Resel results[20].

It is expected that the highly crystalline region at the nanotube surface will exhibit the best possible chain stacking in PmPV. This would be similar to the most ordered component present in the polymer film. For this reason the melt of the crystals at the nanotube surface should occur at the same temperature as the most efficiently formed crystals of the polymer film explaining the increase of the primary polymer peak (59 °C) in the composites. The quantity of polymer in the highly ordered conformation has therefore increased upon introduction of MWNT.

In addition, the introduction of nanotubes results in a new melt peak at the higher temperature of 73 °C in the composite curve. An increase in T_m has been reported to occur with increasing polymer crystallinity in some systems, such as high-density-polyethylene (HDPE)[26]. Thus the 73 °C shoulder exhibited by the composite is associated with the more ordered crystalline conformation of PmPV and has been nucleated by interaction with the NT surface. An idealistic schematic of the semi-crystalline polymer and the composite is shown in Figure 4-9(a) and (b), respectively. Note that a SWNT has been used to represent the nanotubes for clarity in the composite schematic.

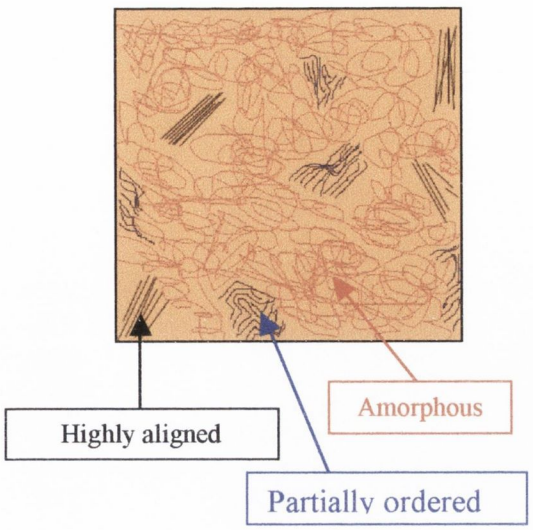

Figure 4-9(a): *Semi-crystalline PmPV schematic.*

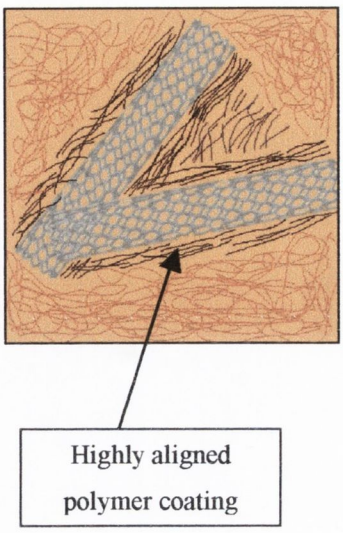

(b) *Composite schematic simplified by the use of SWNT for illustrative clarity.*

The simplistic illustrations of Figure 4-9 raise some interesting questions about the exact nature of the new ordered phase identified by DSC: will the polymer chains wrap around the nanotube or perhaps stack longitudinally on the surface coating the entire circumference? To answer this question it is useful to approximately calculate the number of monomer units per unit volume of the 20 g/L PmPV/Toluene solution. The molecular weight of the monomer is 456.64 amu. This means 6×10^{23} monomers weigh 456.64 g. Therefore there are 2.627×10^{22} monomer units per L in a 20 g/L solution. The volume of the cylindrical nanotube can be calculated at 2.545×10^{-22} m^3 using the average radius (9 nm) and length (1 μm). Theoretically a nanotube could displace 6,686 monomer units in solution based on these figures. Given the molecular weight of 48,533 amu and number-average molecular weight (M_n) of 8785 amu there is an average of 19 monomer units per chain. This simple calculation implies there are greater than 350 polymer chains displaced by the nanotubes in addition to the surrounding polymer chains.

If a region extending 30 nm into the polymer bulk from the tube surface is considered the calculation implies there is a total of 6606 chains present in the vicinity of the polymer/nanotube interface. These chains will exhibit steric hindrance due to the long dioctyloxy sidechains. Thus, while some chains may wrap around the nanotubes, as suggested by modelling studies[1,29], it is impossible for all chains to coil perfectly around the nanotube. A more realistic model of the system is one where crystal growth is nucleated at the nanotube surface forming a mixture of crystal structures: some less

crystalline due to partially aggregated and others with a more ordered structure. This model is consistent with the broad nature of the DSC melt. If perfect crystal nucleation was occurring then a much sharper melt peak would be expected.

Once the crystals formed in solution or during film drying have been melted, the polymer conformation induced in the solution or film-casting stages will have been destroyed. This implies that the cooling and second heat steps represents the morphology adopted by the composite independent of the solvation step and therefore will be referred to as the solid-state environment.

The absence of exothermic peaks during the cooling step, for all the samples, indicates that no detectable re-crystallisation occurs. Therefore the crystals observed in the first melt of the films are characteristic of the solution/film casting procedure. This highlights the difference in using PmPV as the host polymer compared to using more crystalline polymers that do re-crystallise and have been used by other researchers[8,10]. Those studies have used the crystallisation peak of PP to perform isothermal DSC measurements and determine the effect of SWNT on the crystallisation kinetics in the solid state - it was concluded that nucleation of crystal growth does occur in the composite although the inherent crystallinity level of PP is not increased. This is in contrast to the results reported here where the crystallinity of PmPV is increased.

Following the first heat run and the subsequent cooling step, a final heating step was carried out. The absence of re-crystallisation during the preceding cooling run suggests that the melting observed during the second heating is attributable to the crystals formed in the drop cast solution that were not melted by the relatively fast 40 °C/min first heat run. Thus the second heat run is proposed as a method to investigate the nature of the small amount of un-melted material and ascertain the extent of composite melting during the first heat. The data in Figure 4-10 shows that the 73 °C shoulder recorded in the first heat of the composite samples, which we have attributed to high level ordering, is not present in the second heat curve. Only the peak at approximately 50 °C, which we have attributed to the less ordered crystalline domains inherent to the bulk polymer, remains and is of lower magnitude relative to the first heat run data.

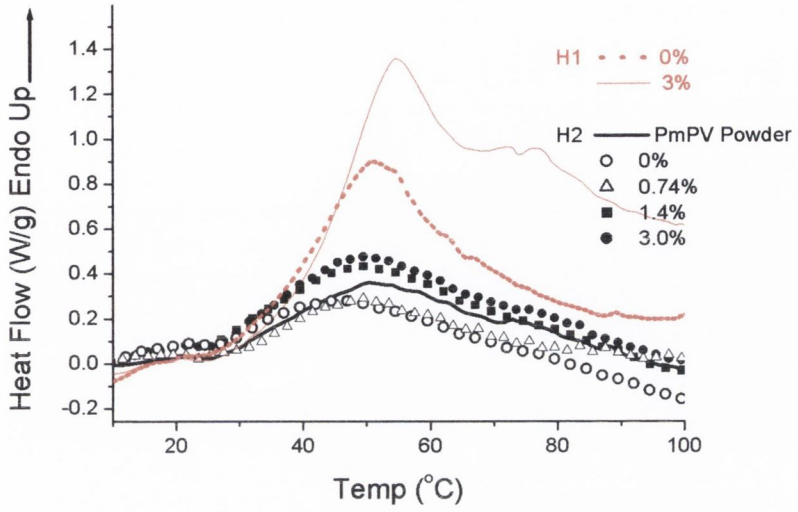

Figure 4-10: *DSC results obtained for second heat scan.*

One possible interpretation of this data is that during the first heat run thermal energy flows through the nanotubes and the polymer immediately in the vicinity of the tubes is melted. In other words, the crystalline coating is melted while the fast scan rate does not give time for heat to propagate entirely through the film so that some lower density semi-crystalline regions survive. The second heat step then only exhibits the low temperature melt peak characteristic the low crystallinity bulk polymer. This is consistent with the TGA data presented in Section 4-3 and previous studies demonstrating the ability of both MWNT[18] and SWNT[30] to efficiently conduct thermal energy. The heat flow data from the first and second DSC heat run was normalized to the primary melt peak for the 3 vol% composite as shown in Figure 4-11. This illustrates the absence of the high temperature shoulder in the second heat for the 3 vol% ArcMWNT/PmPV composite.

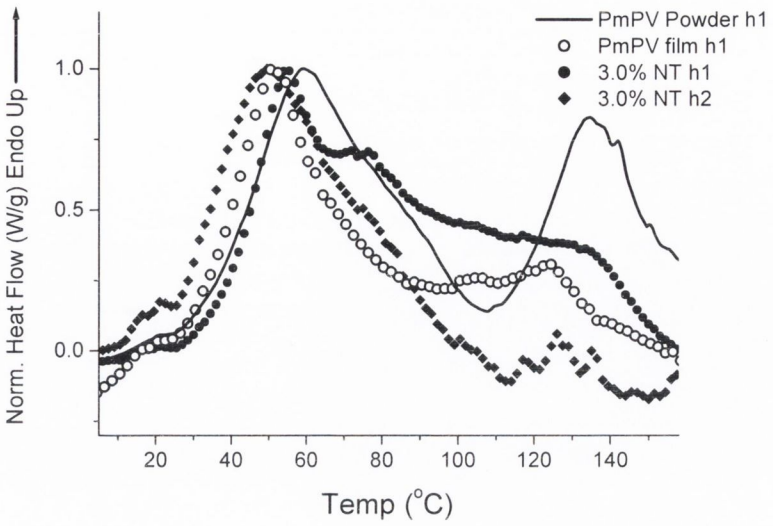

Figure 4-11: *Normalised heat flow for PmPV powder, PmPV film and first and second heat results for 3 vol% composite highlighting the absence of a shoulder in the second heat.*

To further confirm the assumption that the crystals remaining after the first heat were not melted due to the high scan rate, a slow heat rate of 5 °C/min was applied from –90 °C to 170 °C on a pristine composite sample before cooling at 10 °C/min. Subsequently, the second heat scan at 40 °C/min exhibited no melt peaks verifying all crystalline regions melted completely during the first slow heat scan, as expected. In addition this test shows that no recrystallisation occurred during cooling even when the sample was completely melted by the slow heat scan. Table 4-1 lists the enthalpy values.

Table 4-1: *DSC data summary.*

Sample / NT%	Heat run	Peak ±0.2 °C	Enthalpy (J/g)	Crystallinity (%)*
Powder	1	59	20±4	47.5±9.5
	2	50.5	3.7±0.7	
0%	1	51	8±2	20±4
(vol%)	2	46	3±0.6	
0.74 %	1	53.5	12±5	28±6
	2	49.5	1.7±0.3	
1.4%	1	54	18±4	44±17
	2	49	4.1±0.8	
3.0%	1	55	23±5	55±11
	2	49.5	5.5±1.1	

**approximate value calculated relative to enthalpy of 20% film.*

4.6 Photoluminescence Measurements

Polymer morphology can also be probed using photoluminescence (PL) spectroscopy. A combination of PL and absorption spectroscopy can determine the nature of any interchain and intrachain interactions. Absorption spectroscopy is useful to detect complexes formed between ground state molecules. If absorption bands appear that are uncharacteristic of the absorption spectrum of either of the composite elements then charge transfer is occurring. Luminescence measurements can identify the existence of exciplexes – these are interchain interactions between a molecule in its ground state and another molecule in its excited state. If the molecules are of the same species the exciplex is termed an excimer[31], therefore excimer formation is possible between the PmPV chains. The stability of an excimer arises from the overlap of π-orbitals of the two molecules.

Luminescence efficiency tends to be much lower in crystalline polymers because of the formation of another type of complex that is non-radiative. These polaron pairs[32,33,34] form when interchain separation is small enough so the electron is located on one chain while the hole resides on a non-parallel nearest neighbour chain – polaron pairs are also

known as charge transfer excitons. Thus an increase in local crystallinity close to the tube can result in a reduction of the local PL efficiency. In addition excitons formed very close to the tube will preferentially decay non-radiatively through the fast vibrational manifold of the nanotubes[35].

PL intensity was observed to decrease with increasing NT content as shown in Figure 4-12(a).

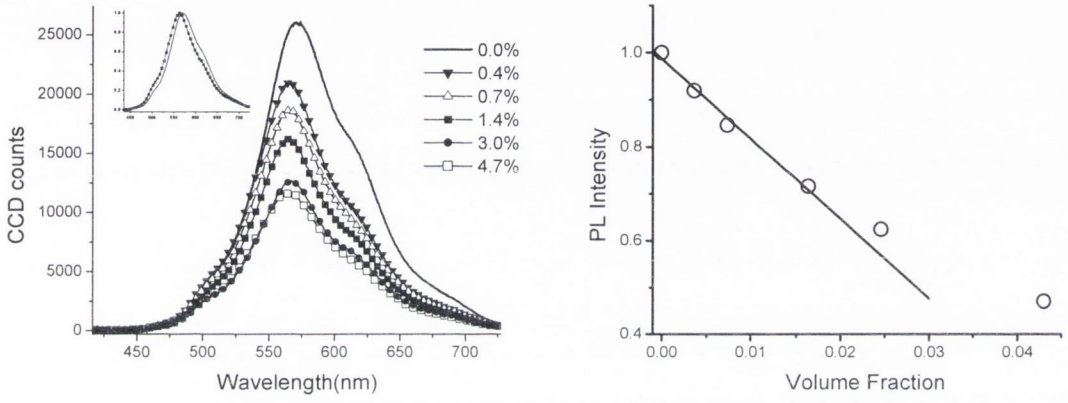

Figure 4-12(a): *PL decrease with increasing NT vol%. [Inset: Polymer and highest NT fraction spectra normalised to wavelength at which maximum photon count has been recorded. 8 nm blue shift observed]* ***(b)*** *Linear Fit to the normalised PL Intensity values as a function of volume fraction.*

An 8 nm blue shift is observed for the polymer peak at a nanotube concentration of 4.7% indicating no radiative excimer formation is occurring since a red shift is characteristic of such processes[31]. This agrees well with the blue shift observed by Star et al[36] in the UV-vis spectrum of PmPV when doped with SWNT. A 6 nm blue shift due to the presence of CVD MWNT in a PPV matrix was reported by Ago et al[43].

The PL intensity decreases with the addition of nanotubes and is consistent with the formation of interchain polaron pairs. The formation of interchain excited states suggests the addition of nanotubes has decreased the polymer chain separation distance and is consistent with the increase in polymer crystallinity measured by DSC above. There is however no dramatic change in the spectral profile suggesting there is no large-scale charge transfer to the nanotube itself – if such charge transfer was occurring, more extensive PL quenching would be expected than observed. In addition, re-absorption by the nanotubes themselves is expected to have little effect as their absorbance has been

shown to be minimal at visible wavelengths[37] for low loading levels. This has been confirmed for the PmPV composite samples used in this experiment using UV-visible absorption measurements and will be presented in the next section.

A simple model for the PL decrease is proposed here. The previously quoted DSC results indicate that the presence of nanotubes nucleates the formation of a crystalline coating of thickness *b*. PL efficiency is expected to be low in this region compared to the bulk amorphous polymer. In the simplest case, we can assume that the efficiency is zero in the crystalline region. The PL intensity, can be described as the number of photons emitted per second, *P*, which can be given by Equation 4-5.

$$P = \Phi N_{ex} V \qquad \textit{Equation 4-5}$$

where Φ is the quantum efficiency, N_{ex} is the number of excitons generated per second per unit volume and V is the sample volume.

In the polymer-nanotube composite case this volume must be partitioned into the emissive (amorphous) volume and the non-emissive (crystalline) volume. Thus Equation 4-5 can be rewritten as:

$$P = \Phi N_{ex} \left[V - N\pi \left(r_{nt} + b \right)^2 l \right] \qquad \textit{Equation 4-6}$$

where N is the number of nanotubes in the sample, r_{nt} is the nanotube radius, b is the crystalline coating thickness and l is the nanotube length. By definition, the volume fraction, v_f, can be written as:

$$v_f = \frac{N}{V} \pi r_{nt}^{\ 2} l \qquad \textit{Equation 4-7}$$

Substituting N from Equation 4-7 into Equation 4-6 and normalising gives:

$$\frac{P}{\Phi N_{ex} V} = 1 - v_f \left(\frac{b^2}{r_{nt}^{\ 2}} + 2\frac{b}{r_{nt}} + 1 \right) \qquad \textit{Equation 4-8}$$

This equation describes the reduction in luminescence due to the nucleation of non-emissive, crystalline regions of polymer by the nanotubes.

Fitting to the linear, low volume fraction region of the data in Figure 4-12(b) yields a value for b of 32 nm in reasonable agreement with the thickness of 25 nm calculated from DSC measurements. The model is theoretically expected to break down at the volume fraction where all nanotubes are coated with a polymer coating of thickness b and no polymer remains un-associated with a nanotube. At this critical concentration the nanotubes must be in close proximity resulting in an overlap of crystalline regions. At this volume fraction since all polymer is divided among the number of nanotubes the volume fraction (of nanotube to polymer) for a single polymer coated nanotube will be identical to that of the whole system. The volume fraction of an individual nanotube to its associated polymer is given by $v_f = v_{nt}/(v_p + v_{nt})$. This equation can be expressed simply in terms of the geometrical cylindrical volumes and many of the terms cancel to yield $v_f = r_{nt}^2/(r_{nt} + b)^2$. Substituting the value of 32 nm as determined by PL spectroscopy for b indicates that the model of linear PL decrease with increasing nanotube concentration should breakdown at v_f = 2.4 vol%. This agrees well with the deviation from linearity observed for PL intensity values of the highest mass fractions. Thus, it is probable that the curvature observed in the data in Figure 4-12(b) is due to breakdown of the model at higher volume fraction due to coalescence of adjacent crystalline regions or nanotube aggregation. It should be emphasised that the calculated layer thicknesses of 25 nm by DSC and 32 nm by PL agree well with a value of 25 nm established by TEM and published previously by McCarthy et al[1]. To complement the extensive DSC and PL study, the following secondary techniques were briefly investigated to confirm the morphological changes discussed above.

4.7 Photoluminescence (PL) degradation studies

In 1982 it was suggested that singlet oxygen may be responsible for photo-degradation of polyacetylene[38]. The issue surfaced again in 1990 when polymer photo-degradation and

stability were the main obstacles to improving the electroluminescence of poly(p-phenylenevinylene) (PPV) based devices. In 1991 it was shown that the photo-excitation of poly(3-alkylthiophenes) produces singlet oxygen, which can react with these polymers. In 1994 studies on PPV showed that photo-degradation in air resulted in the formation of carbonyl groups on the PPV backbone resulting in decreased photoluminescence (PL) efficiency, while the same experiment conducted under nitrogen had no effect on the carbonyl groups population and hence the PL efficiency[39]. In 1995 detailed studies on the photo-degradation of poly(2,5-bis(5,6-dihydrocholestanoxy)-1,4-phenylenevinylene) [BCHA-PPV] were published by two independent group[40,41]. Both groups explained in detail how ground state triplet oxygen can be excited to form singlet oxygen which breaks the vinylene bond on the polymer backbone leading to reduced conjugation lengths and hence reduced PL efficiency through an increase in the number of non-radiative recombination sites. They also show that the bulky side chains, added to PPV to increase solubility, are also involved in the photo-degradation of the polymer. While device encapsulation dramatically improves device lifetime through the exclusion of oxygen and water, it does not improve the inherent polymeric properties of stability and efficiency. The Ph.D. thesis by S. M. Lispon entitled "Optical and Electrical Properties of Modified Conjugated Polymer Thin Films" developed degassing treatment methods, coupled with increased interchain separation, that increased the efficiency of PmPV films by 24%[42].

For the work presented here a spun cast film was constantly exposed to UV light for 1 hr in air while a photoluminescence spectrum was captured every two minutes. The luminescence intensity was then calculated by integrating the area under each spectrum. The values were normalised to the polymer only film and plotted against time as shown in Figure 4-13.

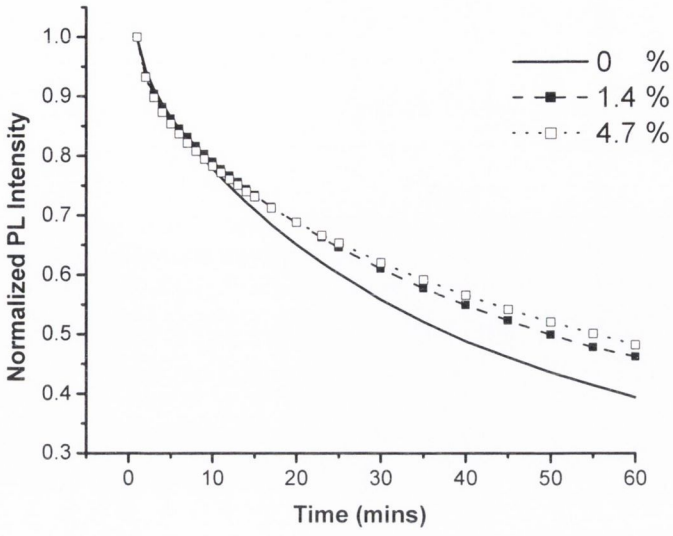

Figure 4-13: *Photo-degradation curves for spun cast polymer (solid line), 1.4 vol% (solid square) and 4.7 vol% (hollow square) composite films.*

The luminescent decay curves were modelled using a bi-exponential fit, as shown in Equation 4-9. The parameters *u* and *v* are the initial intensities of the individual decay curves and their sum is the initial PL intensity.

$$y = ue^{\frac{-t}{\tau_1}} + ve^{\frac{-t}{\tau_2}} \qquad \textit{Equation 4-9}$$

Two different regimes of luminescence decay are evident. There is an initial time constant τ_1, followed by a second longer time constant τ_2. Where τ_1 and τ_2 are time constants, defined as the time taken for the PL intensity to fall to 1/e of its initial value and therefore are a measure of the lifetime of the luminescence from the samples. The time constants are shown in Table 4-2. It is evident that the presence of nanotubes increase the intial decay rate as represented by the 49.3% decrease in τ_1. However the secondary decay rate is reduced with a 30.3% increase in τ_2.

Table 4-2: *Biexponential time constants.*

NT vol%	τ_1 (mins)	τ_2 (mins)
0	8.1	83.3
1.4	4.5	90.9
4.7	4.1	100.0

Lipson[42] performed degradation experiments in both air and argon. By comparing the data he showed that the initial sharp decay is due to oxygen in the atmosphere and the second decay was related to the volume of oxygen trapped in the film during preparation. Thus the time constants can be used to assess the gas permeability of the films. The decrease in τ_1 with addition that nanotubes shows that nanotubes increase the permeability of the polymer to oxygen in the atmosphere. However, the increase in τ_2 shows that nanotubes are reducing the oxygen trapped within the film and reducing the degradation rate. This agrees fully with the increase in crystallinity measured above which would reduce the available free volume that oxygen can occupy within the composite.

4.8 UV-Visible Spectroscopy Results

UV-visible spectroscopy was carried out on spin cast thin films of the PmPV and composite deposited on quartz. Figure 4-14 clearly shows there is marginal absorption in the visible region. This is in perfect agreement with studies by Ago et al[43] and Elim et al[44] who investigated UV-Vis absorption of CVD MWNT. Ago subsequently embedded the CVD MWNT in PPV and measured the PL and absorption of the composite. Low absorption in the visible region indicates that the dramatic loss in PL upon introduction of the Arc_MWNT is not attributable to charge transfer processes - photoinduced charge transfer can quench luminescence as they are up to 1000 times faster than luminescence reactions. This supports the model proposed above which is in excellent agreement with the PL data.

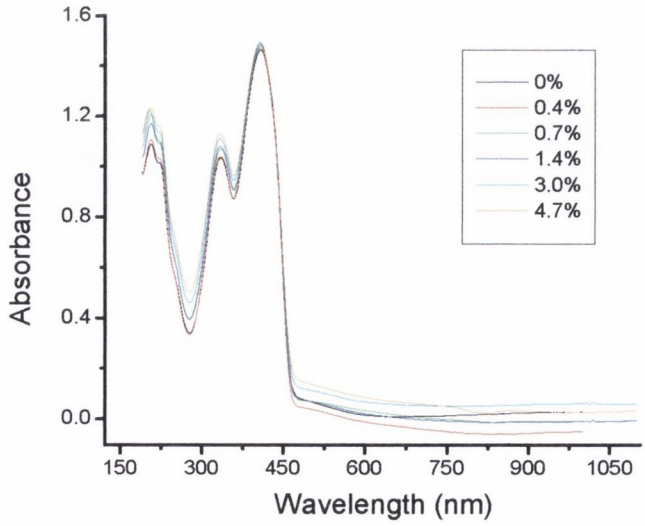

Figure 4-14: *UV-vis spectra for all PmPV/Arc MWNT composites.*

4.9 Fourier Transform Infrared Spectroscopy (FTIR)

The region of interest in the FTIR spectrum is between 100 and 1000 cm^{-1}. Absorbance in this region changes with crystallinity for many compounds. An article by Mallapragada and Narasimhan[45] gives an excellent review of the applications of FTIR to semi-crystalline and liquid crystalline polymers. When a polymer passes from the amorphous to the crystalline phase three things may occur: new absorption bands may appear, splitting of existing peaks may be observed and/or changes in peak intensities. The technique has been successfully employed for polymers such as polyurethane[46], polyethylene[47] and polystyrene[48].

The primary region of interest for the PmPV composites is between 630 and 700 cm^{-1}. Here a dramatic increase in absorption confirms a change in polymer morphology with the addition of nanotubes. The absorption area between 625 and 710 cm^{-1} increases by 61% for the highest nanotube volume fraction of 4.7%. It should be noted that the number of data points is limited by the sampling rate of the spectrometer but enough points are present to confidently detect the presence of a peak at 669 cm^{-1} in the nanotube composites shown in the inset of Figure 4-15. This peak is not present or of very low magnitude in the pristine polymer. For clarity, the inset only shows the 1.4 and 4.7 wt% composites with the pure polymer.

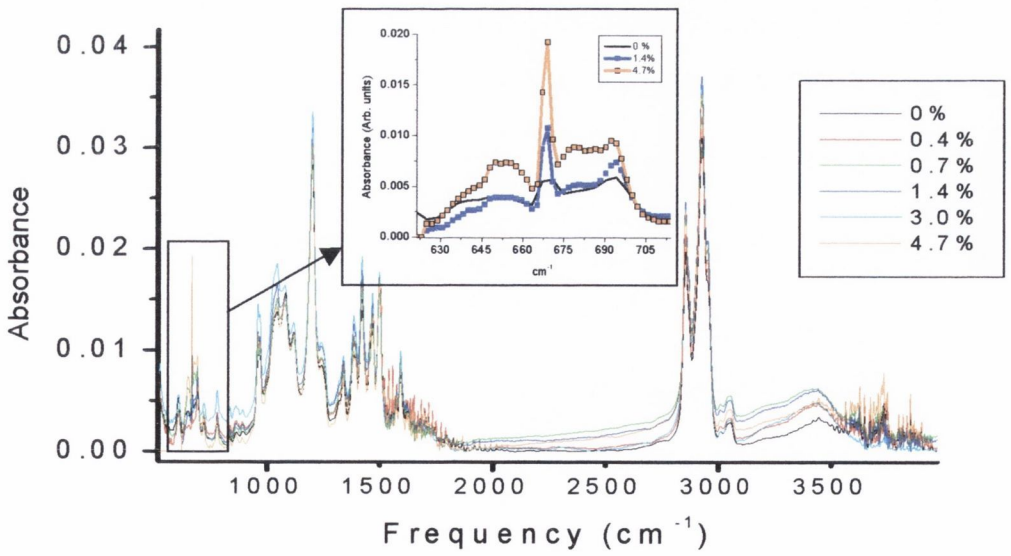

Figure 4-15: *FTIR spectra of PmPV and the ArcMWNT composites. Inset magnifies fingerprint region, only three nanotube concentrations are shown for clarity.*

4.10 Mechanical measurements

Preliminary mechanical measurements were carried out on both the tensile tester and the dynamic mechanical and thermal analyser (DMTA) to characterise a free-standing film of PmPV and the composite with the highest nanotube content. All samples were cut to measure 20 (± 0.3) mm x 3 (± 0.3) mm and had a thickness of 0.14 ± 0.02 mm after drop casting. Figure 4-16 shows the stress strain curves obtained using the tensile tester operated in an ambient environment at 17 °C. The Young's modulus (Y), ultimate tensile strength (σ_T) and toughness (T) are shown in Table 4-3 and demonstrate that while Arc_MWNT are useful to increase the stiffness of PmPV, strength and toughness are compromised.

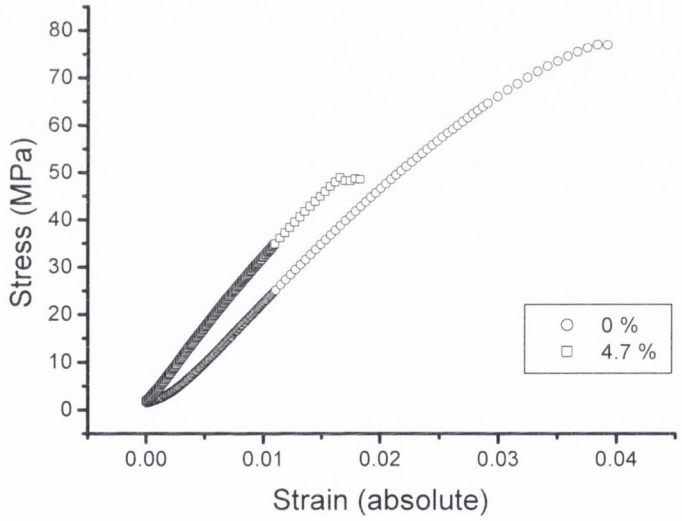

Figure 4-16: *Stress/strain curve for PmPV (circles) and 4.7% Arc_MWNT composite (squares).*

Table 4-3: *Mechanical data for PmPV and 4.7% composite.*

	Y (GPa)	σ_T (MPa)	T (J/m^3)
PmPV	2.48	76.9	1.69
PmPV/4.7% ArcMWNT	3.24	48.9	0.52
Difference (%)	+30.6	-36.4	-69.2

A 14% error in the tensile results arises from the error in calculation of the cross sectional area. Additional strips from the same films were tested using the tension head of the DMTA. A scan was initiated over a temperature range of 0 to 140 °C at a rate of 2 °C/min. The frequency was 1 Hz. While the composite initially exhibits a higher storage modulus, *E'*, the relationship changes with temperature, shown in Figure 4-17. As expected from the increase in thermal conductivity identified by TGA, the composite storage modulus falls off more rapidly with temperature relative to the neat polymer film.

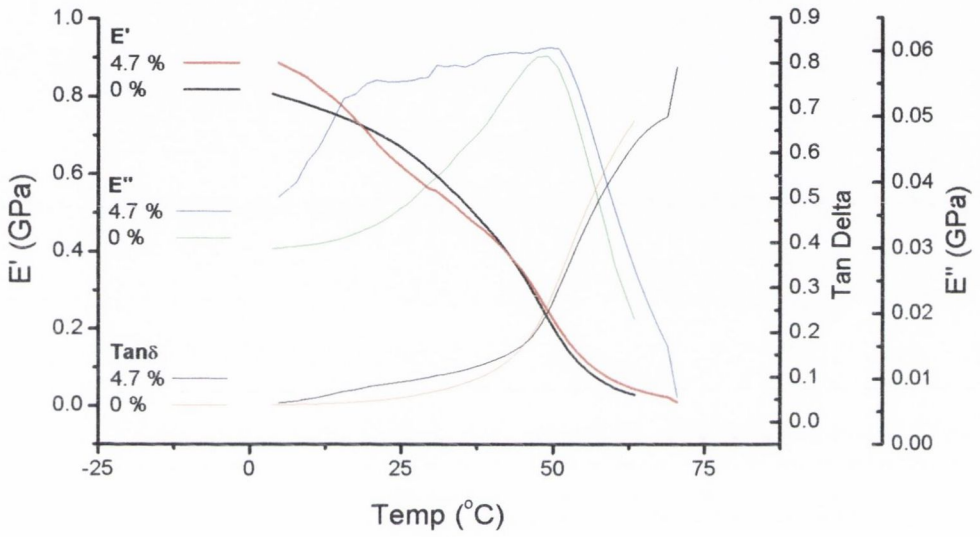

Figure 4-17: *DMTA of PmPV and 4.7% Arc_MWNT composite.*

Both the PmPV and composite films melt before *Tan δ* reaches a peak thus a glass transition temperature cannot be identified. However *Tan δ* increases slowly from 8 °C to 49 °C before sharply rising. This indicates, that as expected, the mobility of the polymer chains increases slowly with temperature as it approaches the polymer melt temperature. The PmPV *E''* peak at 49.18 °C corresponds to the melt temperature and agrees well with the value of 51°C measured using DSC. The *E''* peak increases marginally to 51.02 °C with addition of nanotubes and is consistent with the higher melt temperature associated with the more ordered crystalline phase in the DSC data.

4.11 Conclusions

TGA confirmed the presence of Arc_MWNT in the PmPV matrix and indicated a nanotube induced change in the polymer backbone conformation. To further investigate the changes in polymer morphology identified by TGA, WAXS and DSC crystallinity studies were undertaken. WAXS data did not find an increase in polymer crystallinity while DSC measured an almost 3-fold increase in crystallinity at a nanotube concentration of 3 vol%. The absence of increased crystalline scattering in the WAXS pattern is most likely due to the thin 140 μm film thickness which reduces the number of layers that contribute to the scattering signal. A film with a thickness of several millimetres would be required to ensure maximum sensitivity and utilize the penetration depth of the X-Rays. Film thickness is not an issue for DSC which allows stacking of the sample in the crucible. The furnace then melts the entire contents and heat flow is averaged over the total sample mass. For this reason DSC is very suitable for the experiments presented here and was the preferred technique. A model was proposed where the crystalline polymer resides at the polymer-nanotube interface. A crystalline volume calculation based on this proposed geometry calculates a thickness of 25 ± 10nm for the crystalline region adjacent to the nanotube. This calculation incorporated the crystalline fractions determined relative to an assumed 20% crystalline neat polymer film hence the large error. Nevertheless, such a crystalline layer would account for the photoluminescence quenching observed in the NT composites given that UV-Vis data does not identify a charge transfer process. A layer thickness of 32 nm was obtained by fitting a model of the system to the photoluminescence data. Both these thickness values of 25 and 32 nm agree well with a value of 25 nm reported previously by TEM[1].

FTIR provides further evidence of a change in polymer conformation with a significant increase in the peaks of the fingerprint region. Specifically, the absorption area between 625 and 710 cm^{-1} increases by 61% for the highest nanotube volume fraction of 4.7 vol%.

Mechanical measurements show that nanotubes enhance the stiffness of PmPV by 30.6% but compromise toughness and strength. The composite measured contained 4.7 vol% Arc_MWNT: it was realised in later experiments that nanotube overloading can have an adverse effect on mechanical performance. The following chapters will address this issue.

Since PmPV is a semi-crystalline polymer and as such contains a mixture of several phases it was difficult to analyse the results and separate the contributions of these various conformations. For this reason, the more crystalline polymer poly(vinyl alcohol) (PVOH) was the preferred choice for the extensive crystallinity and mechanical property experiments to be reported in Chapters 5 and 6. The main conclusion of this chapter is that the results, as published in Chemical Physics Letters[49], are consistent with highly crystalline PmPV coating the nanotubes to a thickness of 25-32 nm. As a result of this coating nanotubes have been shown as effective crystal nucleation sites with the result that the crystalline fraction of the matrix polymer is increased.

4.12 References

[1] B. McCarthy, J.N. Coleman, R. Czerw, A.B. Dalton, M.I.H. Panhuis, A. Maiti, A. Drury, P. Bernier, J.B. Nagy, B. Lahr, H.J. Byrne, D.L. Carroll, W.J. Blau; "A microscopic and spectroscopic study of interactions between carbon nanotubes and a conjugated polymer", *J. Phys. Chem. B* **106**, 2210 (2002)

[2] H.J. Barraza, F. Pompeo, E.A. O'Rear, D.E. Resasco; "SWNT-Filled thermoplastic and elastomeric composites prepared by miniemulsion polymerization", *Nanolett.* **2**, 797 (2002)

[3] F. Balavoine, P. Schultz, C. Richard, V. Mallouh, T.W. Ebbesen, C. Mioskowski; "Helical crystallization of proteins on carbon nanotubes: A first step towards thedevelopment of new biosensors", *Angewandte Chemie-International Edition* **38**, 1912 (1999)

[4] W. Ding, A. Eitan, F.T. Fisher, X. Chen, D.A. Dikin, R. Andrews, L.C. Brinson, L.S. Schadler, R.S. Ruoff; "Direct observation of polymer sheathing in carbon nanotube-polycarbonate composites", *Nanolett.* **3**, 1593 (2003)

[5] K. Keren, R.S. Berman, E. Buchstab, U. Sivan, E. Braun; "DNA-Templated carbon nanotube field-effect transistor", *Science* **302**, 1380 (2003

[6] C. Richard, F. Balavoine, P. Schultz, T.W. Ebbesen, C. Mioskowski; "Supramolecular self-assembly of lipid derivatives on carbon nanotubes", *Science* **300**, 775 (2003)

[7] A. Star, J-C. P. Gabriel, K. Bradley, G. Grüner; "Electronic detection of specific protein binding using nanotube FET devices", *Nanolett.* **3**, 459 (2003)

[8] B.P. Grady, F. Pompeo, R.L. Shambaugh, D.E. Resasco; "Nucleation of Polypropylene Crystallization by Single-Walled Carbon Nanotubes", *J. Phys. Chem. B* **106**, 5852 (2002)

[9] A.R. Bhattacharyya, T.V. Sreekumar, T. Liu, S. Kumar, L.M. Ericson, R.H. Hauge, R.E. Smalley; "Crystallization and orientation studies in polypropylene/single wall carbon nanotube composite", *Polymer* **44**, 2373 (2003)

[10] L. Valentini, J. Biagiotti, J.M. Kenny, S. Santucci; "Morphological characterization of single-walled carbon nanotubes-PP composites", *Composites Science and Technology* **63**,1149 (2003)

[11] R. Murphy, J.N. Coleman, M. Cadek, B. McCarthy, M. Bent, A. Drury, R.C. Barklie, W.J. Blau; "High-yield, nondestructive purification and quantification method for multiwalled carbon nanotubes", *J. Phys. Chem. B* **106,** 3087 (2002)

[12] M. Cadek, R. Murphy, B. McCarthy, A. Drury, B. Lahr, R.C. Barklie, M. in het Panhuis, J.N. Coleman, W.J. Blau; "Optimisation of the arc-discharge production of multi-walled carbon nanotubes", *Carbon* **40**, 923 (2002)

[13] W. Kraetschmer, L.D. Lamb, K. Fostiropoulous, D.R. Huffman; "Solid C60 - a new form of carbon", *Nature* **347**, 354 (1990)

[14] D. Qian, E.C. Dickey, R. Andrews, T. Rantell; "Load transfer and deformation mechanisms in carbon nanotube-polystyrene composites", *Appl. Phys. Lett.* **76**, 2868 (2000)

[15] C.A. Finch; "Poly(Vinyl alcohol) – development", *John Wiley & Sons Ltd*, Chichester (1992)

[16] M.S.P. Shaffer, A.H. Windle; "Fabrication and characterization of carbon nanotube/poly(vinyl alcohol) composites.", *Adv. Mat.* **11**, 937 (1999)

[17] J. McMurray, R.C. Fay; "Chemistry", *Prentice Hall*, London (1995)

[18] P. Kim, L. Shi, A. Majumdar, P.L. McEuen; "Thermal transport measurements of individual multiwalled nanotubes", *Phys. Rev. Lett.* **87**, 215502 (2001)

[19] A. Drury, S. Maier, M. Ruether, W.J. Blau; "Investigation of different synthetic routes to and structure–property relationships of poly(m-phenylenevinylene-co-2,5-dioctyloxy-pphenylenevinylene)", *Journal of Materials Chemistry* **13**, 485 (2003)

[20] R. Resel, B. Tertinek, S. Tasch, A. Davey, W.J. Blau, H.H. Horhold, H. Rost, G. Leising; "Conformation studies on layers of soluble poly (para-) phenylenevinylenes", *Synthetic Metals* **101**, 96 (1999)

[21] Y. Liu, S. Xiaolong, Z. Tingkai, Z. Jiewu, M. Hirscher, F. Philipp; "Amorphous carbon nanotubes produced by a temperature controlled DC arc discharge", *Letters to the editor/Carbon* **42**, 1852 (2004)

[22] Y. Chen, M.J. Conway, J.D. FitzGerald, J.S. Williams, L.T. Chadderton; "The nucleation and growth of carbon nanotubes in a mechano-thermal process", *Carbon*

[23] L. Cao, H-Z. Chen, H-B. Zhou, L. Zhu, J-Z. Sun, X-B. Zhang, J-M. Xu, M. Wang; "Carbon-Nanotube-Templated Assembly of Rare-Earth Phthalocyanine Nanowires", *Advanced Materials* **15**, 909 (2003)

[24] F.J. Baltá-Calleja, C.G. Vonk; "X-ray scattering of synthetic polymers", *Elsevier*, Oxford (1989)

[25] Perkin Elmer; "Polyethylene: The Effect of Thermal Conditioning on Percent Crystallinity", *Perkin Elmer Thermal Analysis Newsletter* **PETAN-58**.

[26] V.A. Bershtein; "Differential Scanning Calorimetry of Polymers", *Ellis Horwood*, Chichester (1994)

[27] J.A. Mikroyannidis; "Synthesis by Heck coupling of soluble, blue-light-emitting fully conjugated poly(p-phenylenevinylene)s with highly phenylated side groups", M*acromolecules* **35**, 9289 (2002)

[28] C.M. Hassan, N.A. Peppas; "Structure and application of poly(vinyl alcohol) hydrogels produced by conventional crosslinking or by freezing/thawing methods" in Advances in Polymer Science, *Springer,* New York (2000)

[29] A.B. Dalton, J.N. Coleman, M.I.H. Panhuis, B. McCarthy, A. Drury, W.J. Blau, B. Paci, J.M. Nunzi, H.J. Byrne; "Controlling the optical properties of a conjugated co-polymer through variation of backbone

isomerism and the introduction of carbon nanotubes." *Journal of Photochemistry and Photobiology A: Chemistry* **144**, 31 (2001)

[30] M.J. Biercuk, M.C. Llaguno, M. Radosavljevic, J.K. Hyun, A.T. Johnson, J.E. Fischer; "Carbon nanotube composites for thermal management", *Applied Physics Letters* **80**, 2767 (2002)

[31] J. Guillet; "Polymer photophysics and photochemistry", *Cambridge University Press*, Cambridge (1985)

[32] M. Yan, L.J. Rothberg, E.W. Kwock, T.M. Miller; "Interchain excitations in conjugated polymers", *Phys. Rev. Lett.* **75**, 1992 (1995)

[33] M. Yan, L.J. Rothberg, F. Papadimitrakopoulos, M.E. Galvin, T.M. Miller; "Spatially indirect excitons as primary photoexcitations in conjugated polymers", *Phys. Rev. Lett.* **72**, 1104 (1994)

[34] R. Farchioni, G. Grosso; "Organic Electronic Materials", *Springer*, London (2001)

[35] J.N. Coleman, A. Fleming, S. Maier, S. O'Flaherty, A.I. Minett, M.S. Ferreira, S. Hutzler, W.J. Blau; "Binding kinetics and SWNT bundle dissociation in low concentration polymer-nanotube dispersions", *Journal of Physical Chemistry B* **108**, 3446 (2004)

[36] A. Star, J.F. Stoddart; "Dispersion and solubilization of single-walled carbon nanotubes with a hyperbranched polymer", *Macromolecules* **35**, 7516 (2002)

[37] H. Ago, M.S.P. Shaffer, D.S. Ginger, A.H. Windle, R.H. Friend; "Electronic interaction between photoexcited poly(*p*-phenylene vinylene) and carbon nanotubes", *Phys. Rev. B.* **61**, 2286 (2000)

[38] H.W. Gibson, J.M. Pochan; "Chemical modification of polymers. Part 19: Oxidation of polyacetylne", *Macromolecules* **15**, 242 (1982)

[39] M. Yan, L.J. Rothberg, F. Papadimitrakopoulos, M.E. Galvin, T.M. Miller, "Defect Quenching of Conjugated Polymer Luminescence", *Phys. Rev. Lett.* **73**, 744 (1994)

[40] B.H. Cumpston, K.F. Jensen, "Photo-oxidation of polymers used in electroluminescent devices", *Synth. Met.* **73**, 195 (1995)

[41] R.D. Scurlock, B. Wang, P.R. Ogilby, J.R. Sheats, R.L. Clough; "Singlet Oxygen as a Reactive Intermediate in the Photodegradation of an Electroluminescent Polymer", *J. Am. Chem. Soc.* **117**, 10194 (1995)

[42] S.M. Lispon; "Optical and Electrical Properties of Modified Conjugated Polymer Thin Films", *Phd. Thesis*, Dublin University (2001)

[43] H. Ago, M.S.P. Shaffer, D.S. Ginger, A.H. Windle, R.H. Friend; *Physical Review B* **61**, 2286 (2000)

[44] H.I. Elim, W. Ji, G.H. Ma, K.Y. Lim, C.H. Sow, C.H.A. Huan; "Ultrafast absorptive and refractive nonlinearities in multiwalled carbon nanotube films", *Appl. Phys. Lett.* **85**, 1799 (2004)

[45] S.K. Mallapragada, B. Narasimhan; "Infrared Spectroscopy in Analysis of Polymer Crystallinity", *Encyclopedia of Analytical Chemistry*, R.A. Meyers,
John Wiley & Sons Ltd, Chichester, 7644 (2000)

[46] D.Y. Shen, S.K. Pollack, S.L. Hsu; "Far-infrared study of hydrogen-bonding in a semicrystalline polyurethane", *Macromolecules* **22**, 2564 (1989)

[47] J.L. Koenig; "Spectroscopy of Polymers", *Elsevier*, Amsterdam (1999)

[48] X.M. Xie, A. Tanioka, K. Miyasaka; "Fourier-transform infrared spectroscopic studies of gelation and crystallization of polystyrene carbon-disulfide solutions", *Polymer* **34**, 1388 (1993)

[49] K.P. Ryan, S.M. Lipson, A. Drury, M. Cadek, M. Rüther, S.M. O' Flaherty, V. Barron, B. McCarthy, H.J. Byrne, W.J. Blau, J.N. Coleman; "Carbon Nanotube Nucleated Crystallinity in a Conjugated Polymer Composite", *Chem. Phys. Lett.* **391**, 329 (2004)

CHAPTER FIVE: DISPERSION OF CARBON NANOTUBES WITHIN A PVOH MATRIX: OPTIMAL CONDITIONS

5.1 Introduction

It has been shown in Chapter 4 that arc discharge carbon nanotubes can be used to increase the crystallinity of the semi-crystalline polymer PmPV. However it was also noted that PmPV has a low inherent crystallinity and that sensitive measurements were required to detect any variation in morphology even at the relatively high nanotube loading fraction of 8 wt%. Thus poly(vinyl alcohol) (PVOH), a more crystalline polymer than PmPV, was chosen as a more suitable candidate for comparison of crystal and mechanical properties in composites formed with various types of carbon nanotube. PVOH was successfully used to form nanotube composites in 1999 by Shaffer et al[1]. This chapter will begin by measuring the inherent properties of PVOH followed by the development of a process to produce a free-standing polymer film. At this point carbon nanotubes will be introduced and the optimum dispersion parameters are determined. The effects and control of atmospheric water absorption are presented as water critically affects the mechanical properties of the composite. Crystallinity and mechanical measurements are used to determine the DWNT nanotube concentration range that maximises crystal nucleation which in turn will be shown to boost polymer performance.

5.2 Dispersion study

Four different types of nanotube were deliberately selected to assess the relationship between NT diameter and difficulty of dispersion. Nanocyl "thick" MWNT (N_Thick), Nanocyl "very thin" MWNT (N_VThin), Nanocyl DWNT (ND) and Elicarb SWNT (ES). Optical microscopy was used to measure the number and size of nanotube aggregates that were present in the N_thick and N_Vthin films. TEM was required to assess the SWNT and DWNT because the aggregates in the film are too small to be observed with the optical microscope - the fact that the features are unobservable implies that they are reasonably well dispersed during preparation and did not aggregate on a micron scale. Note that PVOH is a colourless non-conducting polymer, thus any aggregates that are observed are due to nanotube aggregation.

5.2.1 Drying temperature and pressure

PVOH/Carbon nanotube composite films were cast from 30g/L PVOH solutions containing 0.5 and 2 wt% of N_thick carbon nanotubes. Each solution received a standard sonication treatment comprising of 5 min tip followed by 2 hr in the sonic bath before a final 5 min tip session. No aggregates were observable in the wet N_thick composite films cast on glass proving aggregation does indeed occur during the subsequent drying process. It is for this reason that drying conditions must be carefully controlled to enhance crystallinity while limiting the formation of large aggregates.

Temperature and pressure have been studied to characterise the drying parameters for both 0.5 wt% and 2 wt% solutions of N_Thick in 30 g/L PVOH. For the dispersion study a vacuum oven was employed since films dried under vacuum exhibited less dust contamination and low pressure conditions did not affect the size or distribution of the aggregates in the film – Later in this chapter it will be shown that the vacuum oven is not suitable for drying free standing films on Teflon as it promotes bubble formation.

Figure 5-1(a) and Figure 5-1(b) show images of the 0.5 wt% dried at 60 °C and the 2 wt% dried at 45 °C, respectively. The majority of smaller aggregates displayed a circular geometry so that the mean diameter was used to classify aggregate size. Large aggregates were assessed by approximating to a circular geometry. At both temperatures more aggregates were observed for the 2 wt% film than the 0.5 wt% film. It appears from the microscope images that these large aggregates are due to the nucleation of many smaller aggregates like those observed in higher temperature films.

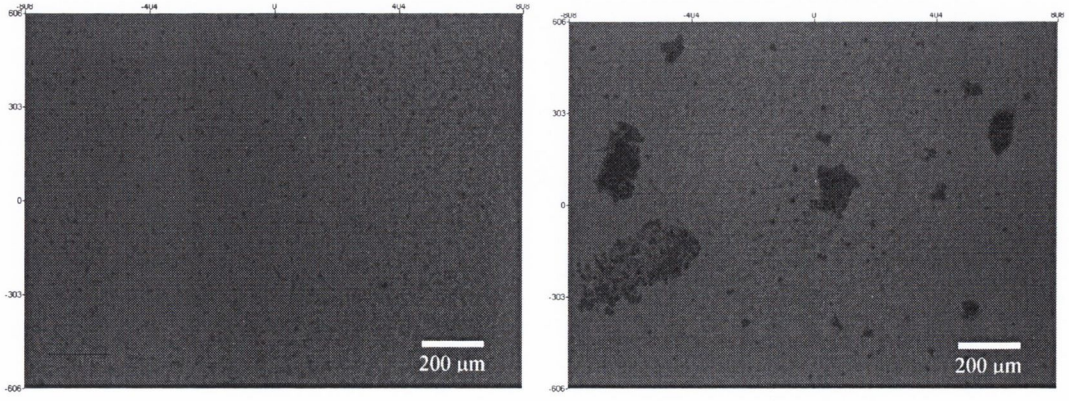

***Figure 5-1(a)** : Optical microscope images of 60 °C 0.5 wt% **(b)** the 45 °C 2 wt% N_thick films. Each precursor solution received 5 min tip – 2 hr bath – 5 min tip.*

Since aggregation takes place during drying, it suggests that when films are dried slowly (lower temperature) small aggregates can form early in the process but remain mobile in the film, allowing them to group together to form bigger aggregates. This accounts for both the irregular shape of the aggregates and why the 2 wt% film shows larger aggregates than the 0.5 wt% film rather than just four times the number of small aggregates. In the more concentrated film there are more small aggregates in close enough proximity to nucleate into these large irregular clusters.

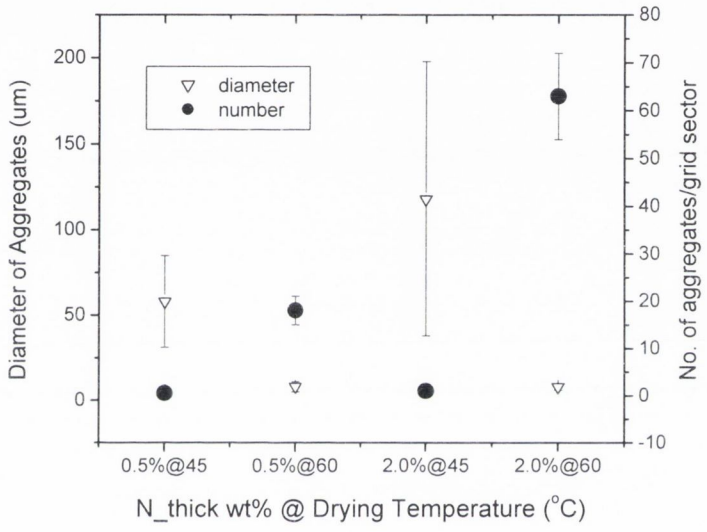

Figure 5-2 : *Aggregation study of 0.5 and 2 wt% composites under vacuum at 45 °C and 60 °C. Each precursor solution received 5 min tip – 2 hr bath – 5 min tip.*

Thus for better dispersion the highest possible drying temperature is preferable but if the rate of drying is too high there is little time for polymer crystallisation in the films. In summary, Figure 5-2 confirms that a low temperature of 45 °C reduces the drying rate thus increasing the time for crystallisation/ aggregation resulting in a small number of large aggregates. Conversely, increasing the drying temperature to 60 °C results in a larger number of smaller aggregates.

5.2.2 Sonication

The next factor for investigation was the effect of various sonication times applied to the solution before drop casting – it was decided to dry these films slowly at 45 °C to promote

large aggregate formation: the reasoning is that varying sonication will alter the tiny nanotube aggregates present in solution that are precursors or nucleating sites of the larger aggregates that grow upon drying: if sonication minimises the size of the final microscope observable aggregate then it confirms the optimum sonication to produce good nanotube dispersion in solution.

Two sonication regimes were adopted: the first program was 5 min tip, 2 hr bath and 5 min tip while the second "further sonication" program consisted of an extra 10 min tip session. Figure 5-3 shows that for the less sonicated samples there are approximately twice as many aggregates in the 2.0 wt% film as the 0.5 wt% film and that the aggregates double in size with the increase in concentration. Further sonication *(fs)*, seems to prevent the formation of large irregularly shaped aggregates, resulting in films with evenly dispersed aggregates of approximately the same size. As expected there are approximately four times as many aggregates observed in the 2.0 wt% film compared to the 0.5 wt% film, and aggregates are the same size in both.

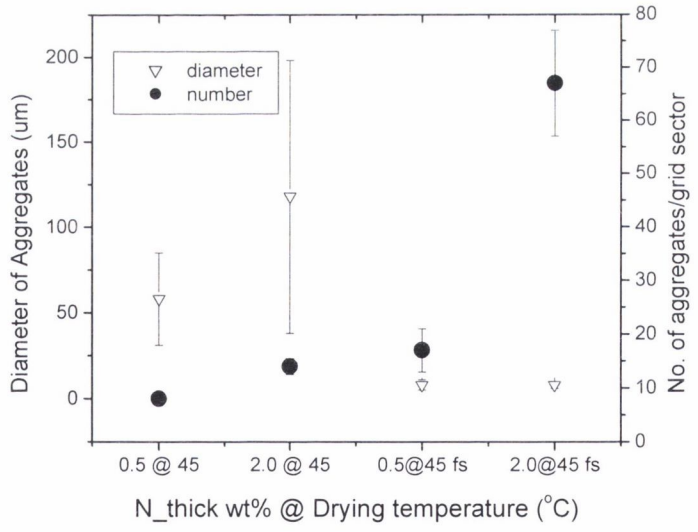

Figure 5-3: *Effect of sonication for 0.5 and 2 wt% films dried at 45 °C. Each precursor solution received 5 min tip – 2 hr bath – 5 min tip while the "fs" films received an extra 10 min under the sonic tip.*

The results presented in the previous two sections suggest that a rigorous sonication regime and an optimum drying temperature of 60 °C are required to produce the best possible nanotube dispersion.

evaporated off it is expected that larger aggregates will form in the 45 g/L film since there are more nanotubes present. Figure 5-5 shows that this is indeed the case. For a good NT dispersion aggregate size and number must be minimised. It can be seen from the graph that these two factors are optimised at 30 g/L were the least observable aggregates are counted. These aggregates have a mean size of 8 μm. Aggregates observed in the 45 g/L solution are considerably larger with an average diameter of 12 μm. Based on this data 30 g/L was adopted as the optimum polymer concentration.

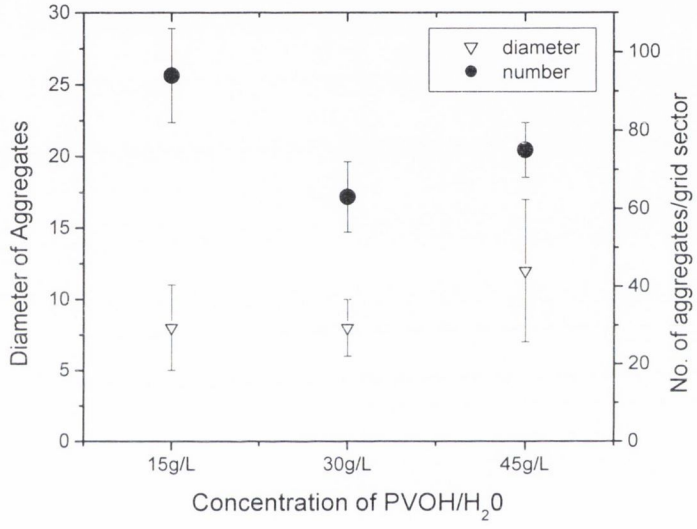

Figure 5-5: *Number and diameter of aggregates with varying PVOH concentration.*

5.2.5 Settling time prior to decantation of solute

When an extended settling time of 14 days was applied to a 2 wt% N_VThin solution before decantation, it was found that the aggregate size increased slightly and the number of aggregates decreased compared to an identical sample decanted after one day. This proved that while highly unstable material sedimented within 24 hours, an additional small amount of nanotubes had re-aggregated in solution over the two week period. As a consequence of this all future composite samples were re-sonicated under the tip for 1 min before any experiments to re-disperse any nanotube re-aggregation and improve reproducibility.

5.2.6 Conclusions of aggregation study

A good dispersion was achieved for mass fractions of up to 5 wt% with all the nanotube types under investigation. However, it is important to state from the outset that these high nanotube levels later transpired to be less effective for reinforcement – Section 5.7 will show that maximum reinforcement is achieved at much lower NT fractions. To achieve well-dispersed small aggregates a high drying temperature is vital. Aggregation occurs mainly in the drying phase and quicker drying means the aggregates are mobile for a shorter time and are hence less likely to agglomerate. Therefore the films need to be dried at a high temperature. To be absolutely sure that no alteration of the polymer morphology occurred during drying, a temperature of 60 °C was chosen since the glass transition of PVOH is 70 °C.

The optimum concentration for the PVOH was found to be 30 g/L. In less concentrated solutions the nanotubes were too mobile as the fluid was less viscous, and in more concentrated solutions the tubes were in close proximity causing undesirable aggregation. Studies also conclusively showed that a longer sonication time with the high powered sonic tip gave both smaller aggregates and a better dispersion. The next section will examine the effects of intensive sonic tip usage on the properties of PVOH and carbon nanotubes.

5.3 Effects of intensive sonic tip use on carbon nanotubes and PVOH

5.3.1 Effect of sonication on polymer crystallinity: DSC

Sonication effects on PVOH morphology were examined by comparing DSC scans of two drop cast films dropped from two bottles of PVOH solution that were prepared using the sonic tip for 2 min and 30 min, respectively, to disperse the polymer powder. The enthalpy of melting was found to be 22.50 J/g for the 2 min sample and 22.11 J/g for the 30 min sample. This confirms within experimental error that there is no alteration of the crystalline structure of the polymer due to intensive sonication. The fact the two values are so close indicates that two minutes under the tip is sufficient to fully disperse the polymer chains.

5.3.2 Effect of sonication on carbon nanotube length and dispersion: TEM

TEM was carried out on composite solutions to examine the structure on the nano-scale, in particular with respect to possible breakage of the CNT by the sonic tip – this was necessary since Liu et al reported breaking of SWNT by prolonged sonication[2]. A PVOH/5 wt% N_Thick MWNT composite solution was given an initial 15 min under the sonic tip after which the TEM image shown in Figure 5-6(b) was taken. The composite solution was then blended to 1 wt% and given a further 45 min under the tip and Figure 5-6(d) was captured. Rapid acquisition of the images was necessary due to melting of the polymer by the electron beam causing distortion and destruction of polymer features – a similar problem has been reported by Lourie et al when imaging Epoxy/CNT composites where polymer strain was induced by heating[3]. Images taken from various points on the TEM grids for each composite were consistent with those of Figure 5-6 and were analysed using "Imagetool".

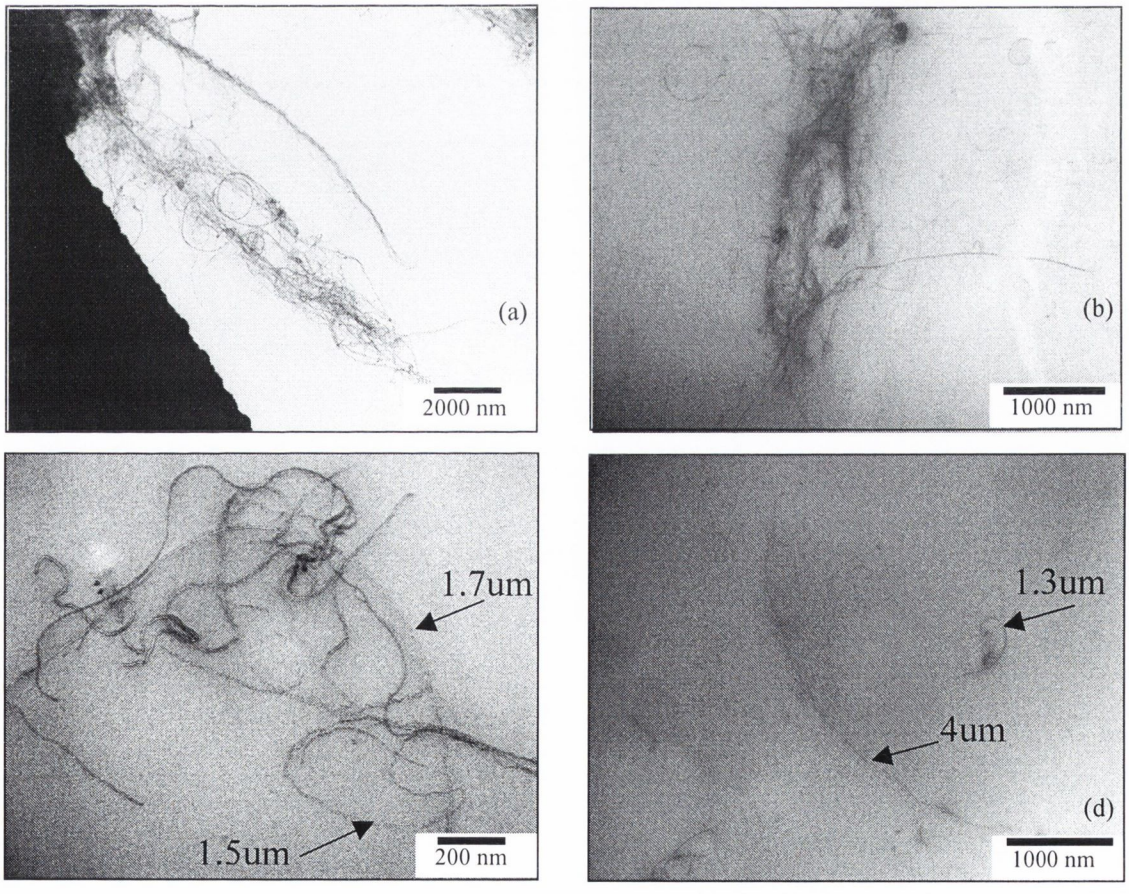

Figure 5-6(a): *N_thick as supplied* ***(b)*** *5 wt% N_thick composite [15 min tip]* ***(c)****Higher magnification of image (a)* ***(d)****1 wt% blended from the 5 wt% N_thick composite given further 45 min tip.*

Given the extensive entanglement observed in the "as supplied" nanotubes (Figure 5-6(a)) it is difficult to reliably determine an average length value – Given the scale bar of 2 μm for the batch of material imaged here, lengths range from 4 μm to 10 μm. Comparing this to Figure 5-6(b) and (c) it can be seen that some shortening of the N_Thick tubes has occurred after 15 min tip sonication. Aggregates of tubes are observed for the 5 wt% sample, even after 15 min tip sonication. The nanotubes in the aggregate do not exhibit the shortening that has occurred for single well dispersed tubes seen in the peripheral areas. Upon dilution to 1 wt% and applying a further 45 min tip the aggregates disappear as shown in Figure 5-6(d). Interestingly, no further shortening of nanotubes is observed when Figure 5-6(c) and (d) are compared suggesting fracture occurred at structural defects in the tubes during the first 15 min sonication and tube lengths remain stable after elimination of these defects. The images also prove that the entanglement exhibited by the 5 wt% composite had been eliminated by the blending to 1 wt% and further 45 min tip sonication. It was at this point that the project began to focus on lower nanotube fractions and employ long sonication times to aid dispersion. The influence of nanotube length on composite reinforcement is still under debate. Qian et al[4] reported a 4% decrease in Young's modulus for a Polystyrene (PS) / MWNT composite when nanotube length was reduced from 50 to 15 μm.

It should be noted that using the sonic tip for long periods of time inevitably increases the temperature of the dispersion. A 28 ml bottle containing 25 ml of solution typically heats to 78 °C after 15 minutes under the tip. This is slightly above the PVOH glass transition temperature of 70 °C. Therefore it is acknowledged here that polymer chain mobility may be increased by long sonication times helping the dispersion of the chains which then can interact with carbon nanotubes.

5.4 Drop cast films on Teflon

After the initial aggregation study it was necessary to process the composite solutions to produce free-standing films with enough material to enable TGA, DSC, DMTA, tensile testing and XRD all from the same film for consistency. Teflon discs were employed to allow easy removal of a drop cast film. While Chapter 3 outlines the final drop casting technique a number of important points were discovered in the process and will be discussed in detail here. Factors including elimination of bubbles, importance of uniform

film thickness and drying time between layers were used to improve the quality and reproducibility of the composite films.

5.4.1 Bubbles

One of the first problems encountered while drop casting was the presence of bubbles in the film after drying. Three distinct sources of bubbles were identified and the following techniques were developed to eradicate them. Firstly, large bubbles were introduced to the system when solution was dropped from above onto the disc in a drip like fashion – these bubbles did not appear in films when the pipette tip was placed on the disc surface while injecting the solution to swell an initial drop of material.

Secondly, inadequate sanding was found to leave small tracks on the discs. When solution was drop cast the surface tension was sufficient to cover the tracks without filling them. This trapped air which subsequently rose to the surface as bubbles upon drying. Use of 1200 grit sandpaper was found to eliminate this source of bubbles.

The size of sample bottle used in relation to sonication time prior to drop casting was identified as the third and final source of bubbles. Small diameter sample bottles were found to be best. It would appear that the larger aspect ratio when using taller bottles is more efficient at elevating air to the top of the solution when they are displaced by the sonic tip and form bubbles. A 30 minute rest period between application of the tip and casting was sufficient to allow the bubbles rise from the solution. Trials have shown tiny evenly dispersed air bubbles appear throughout the film if the rest time is omitted.

5.4.2 Sonic tip efficiency depending on volume of solution

The sonic tip was observed to disperse nanotubes more efficiently when the composites were sonicated in small volumes – for example 10 ml 30 g/L PVOH/H_20 solution containing 0.5 wt% NT powder will turn completely black in approximately 5 seconds while 25 ml of the same concentration in a 28 ml bottle will take 20 seconds to turn black. Based on this simple observation all composites were sonicated in 10 ml batches and then merged in a larger bottle when volumes in excess of 10 ml were required.

5.5 Initial tensile test results: Moisture absorption by PVOH and composites

The significant problem encountered in the early stages of sample testing was fluctuation of mechanical data, in particular for PVOH reference films. Given the well-documented water permeability of PVOH[5,6] initial attempts to control the water content involved drying the thin strips of film in a fan oven at 60 °C for 1 hr prior to testing. However, this approach was not ideal as PVOH reference films tested soon after removal from the oven exhibited an unsatisfactory standard deviation with Young's modulus ranging from 2.8 to 3.9 GPa. These fluctuations were not due to differences in strip dimensions or polymer concentration as these parameters had been carefully controlled.

To evaluate moduli at various levels of water absorption tensile tests were conducted on

(i) A strip that has undergone no additional drying to control its water content since two hour drying period applied to the final layer of solution. Labeled "No Oven" since no oven drying was applied on the test day.

(ii) A strip that was dried for 1 hour to remove water immediately prior to testing. (Approximately 2 minutes to remove sample from the oven, clamp it and activate the test cycle on the tensile tester). Labeled "Immediate"

(iii) A strip that has been dried then left for 10 minutes to allow a time controlled absorption of atmospheric water. Labeled "After 10 min"

The solid black circles in Figure 5-7(a) demonstrate the significant effect of drying conditions on the Young's modulus of the Polymer only films. The red line is at 3.5 GPa in each plot as a visual aid to compare the data points.

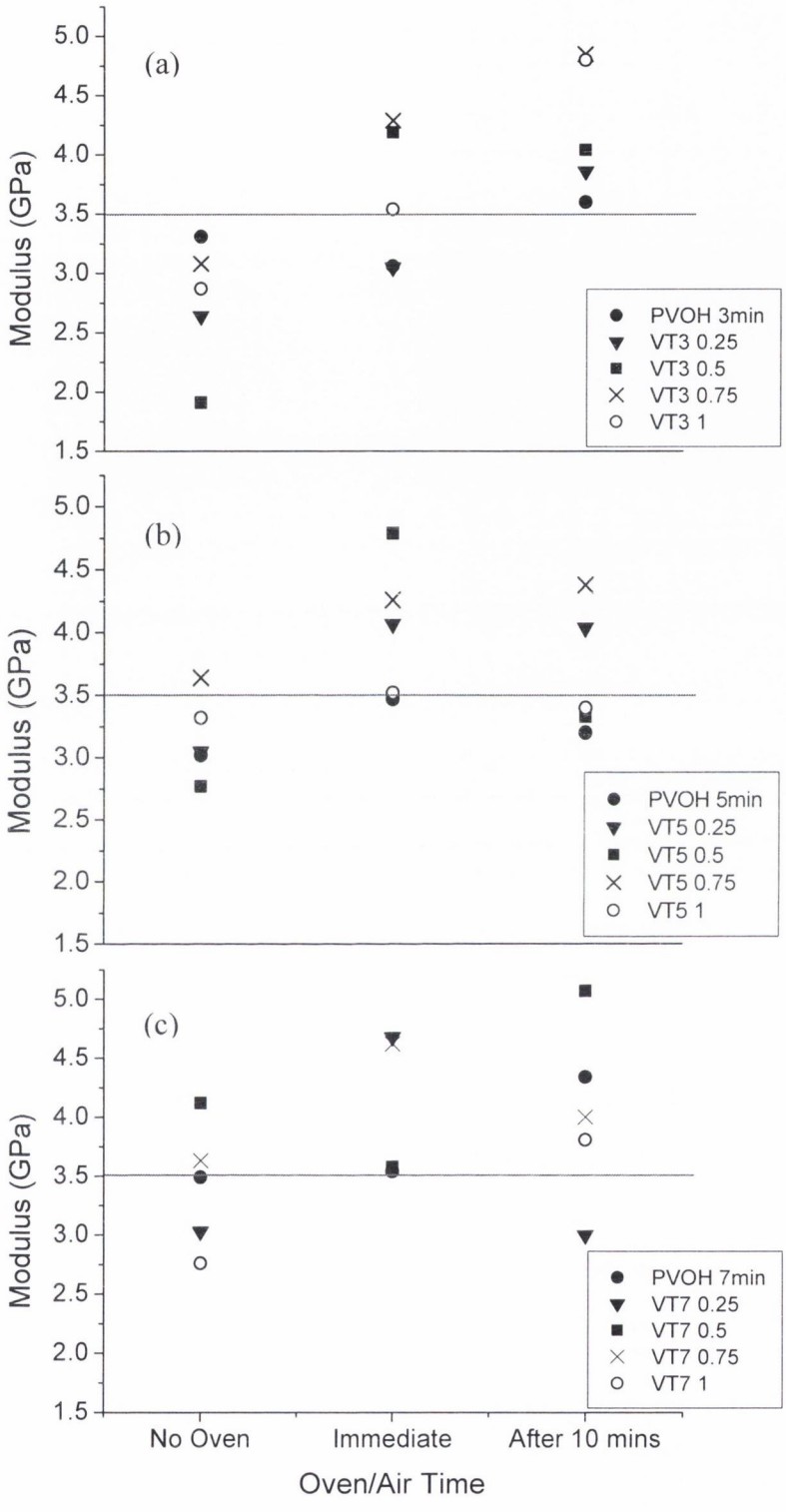

Figure 5-7(a): *Moduli values for PVOH and composites with 3 min tip prior to drop* ***(b)*** *5 min tip prior to drop* ***(c)*** *7 min tip prior to drop.*

The strips that have been tested without drying show lower moduli values compared to samples dried immediately before testing. Interestingly the samples left out of the oven

for 10 minutes before testing exhibit even higher moduli values than the "straight out of oven" tests. It is concluded that the highest modulus values can be achieved with the addition of a limited quantity of water.

Figure 5-7 also shows the data for PVOH/N_Vthin nanotube composites at concentrations of 0.25, 0.5, 0.75 and 1 wt%. The difference between the three data sets shown in Figure 5-7 is the sonication time prior to dropping. (a) received 3 min under the tip, (b) 5 min and (c) 7 min. This was studied to examine if the mechanical properties could be improved by increasing sonic tip time to improve re-dispersion of any sediment/aggregates in solution before drop casting. Although an exceptionally high modulus of 5.04 GPa was observed for the 7 min tip time 0.5 wt% sample, no trend of modulus increase with increasing "pre-drop cast" sonication time is observed. Consequently a tip time of 5 min prior to dropping was adopted as the surface quality was superior to that of the 3 min film.

Armed with this data it was decided that a drying procedure was required that would enable reproducible results rather than achieving the maximum modulus. Using TGA the mass of water contained in discs of PVOH film was monitored after exposure to atmospheric conditions for a range of times up to 2 weeks. Figure 5-8 shows that after 5 days the uptake of water has stabilised so this was taken as the time required for PVOH films to become water saturated. The following procedure was adopted as the most controllable and reproducible: PVOH reference and composite samples were stored after fabrication for a few days – this storage time is irrelevant since drying will eradicate any moisture accumulated over these days so that the films will be back to a base water level. The samples were then dried for 5 hr at 60 °C before stacking their unsealed Petri dishes in the laboratory five days prior to testing. In this way the samples were at an equilibrium water content when tested.

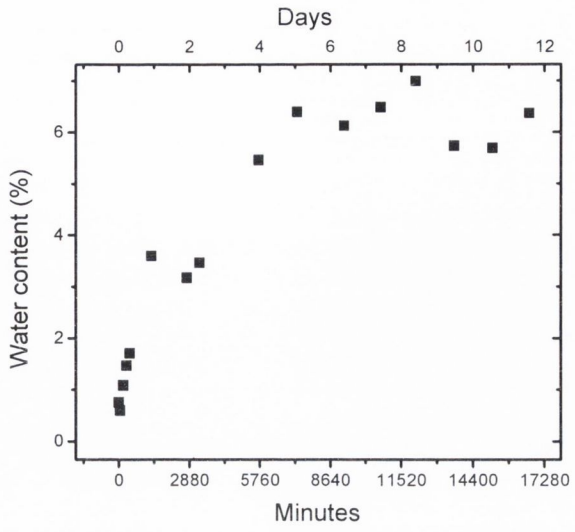

Figure 5-8: *Water content of PVOH film exposed to atmosphere over two weeks.*

One final point to highlight in this section from Figure 5-7(a), (b) and (c) is that the 1 wt% N_Vthin sample does not generally exhibit the highest modulus – in fact the 0.5 wt% does. This suggests a limit exists for the nanotube fraction above which reinforcement of the polymer is compromised. Chapter 6 will focus on this issue.

5.6 Tensile testing

To verify the drying sequence described above a set of N_Vthin composites were made with concentrations of 0.2, 0.4, 0.6, 0.8 and 1 wt%. The Black squares in Figure 5-9 show the modulus data for the samples dried 5 days previously. Strips given extra drying on the day of testing are represented by triangles (1.5 hr drying) and circles (3 hr) – A linear fit can confidently be fitted to the first 5 data points of the films containing water. Again we see that the 1 wt% exhibits a low modulus and in fact the dried samples both peak at 0.6 wt% - this agrees well with the peak at 0.5 wt% exhibited by the early N_Vthin samples shown in Figure 5-7(a) and confirms the reproducibility of the sample preparation/testing techniques.

The ultimate tensile strength values, S, are plotted in red alongside modulus in Figure 5-9.

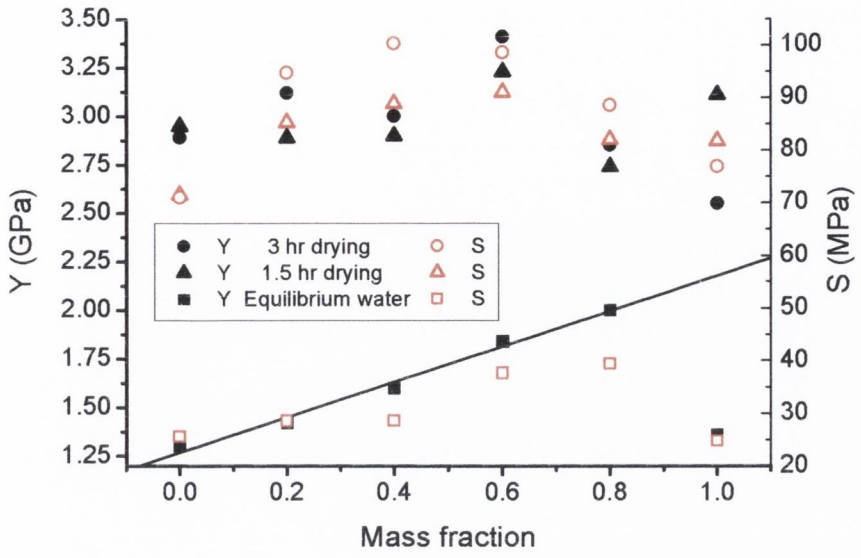

Figure 5-9: *Strength (red) and moduli (black) values for N_Vthin composites with equilibrium water concentration (square), 1.5 hr drying prior to testing (triangle) and 3 hr prior to testing (circle).*

These experiments verify that to achieve reproducibility films should be tested at an "ambient" water content so atmospheric moisture absorption ceases to be a problem. For practical applications it means that the performance of PVOH/NT based composites can only be accurately predicted when they are used in a moisture controlled environment.

5.7 Excess loading – loss of reinforcement

After assessing and optimising the techniques described above, PVOH/nanotube composites were made with N_Thick (average diameter of 25 nm) and ND (average diameter of 2.8 nm), both obtained from Nanocyl S.A. The tensile tests for these samples were conducted using a Perkin Elmer Diamond DMTA with a tension head operated in F-control mode. A jaw spacing of 5 mm was used to clamp the samples while a force ramp rate of 500 mN/min from 0 to 9 N was employed. The data file was exported to excel where the force and head position were extracted to produce a stress/strain curve as shown in Figure 5-10. An impressive increase in Young's modulus was observed upon addition of nanotubes for the lower volume fractions.

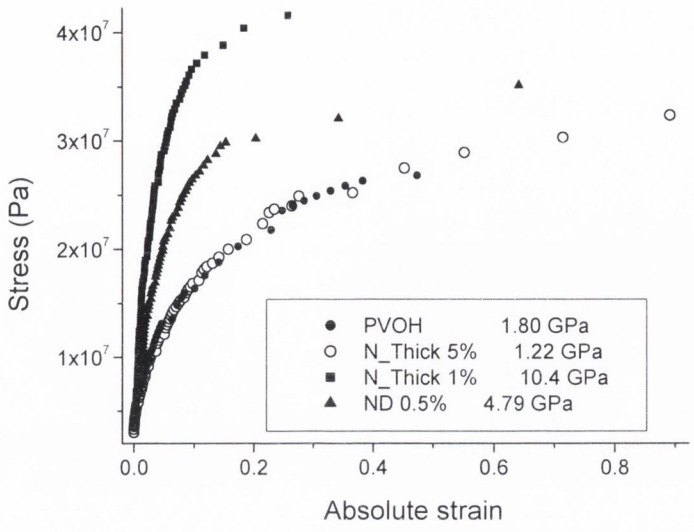

Figure 5-10: *Stress strain curves for the PVOH, ND and N_Thick composites.*

It is interesting to note that the 5 wt% N_Thick composite exhibits no reinforcement but upon dilution to 1 wt% the situation improves dramatically with a 5 fold increase in modulus. This agrees well with the data shown previously in Figure 5-9 for the N_Vthin composites where an upper limit or threshold of 0.5 wt% existed beyond which the modulus deteriorated – here in the case of the N_Thick sample the threshold appears to be a little higher with 1 wt% having a modulus 6 times that of the pure PVOH. The threshold value may vary depending on nanotube type, for example SWNT would be expected to aggregate or bundle at different concentration to ArcMWNT – Chapter 6 aims to investigate if there exists a diameter dependence on reinforcement.

The emergence of a threshold above which excess nanotubes compromise mechanical performance is not surprising since familiar composites such as reinforced steel and reinforced concrete exhibit similar critical filler loading fractions. Reinforced steel is a metal alloy whose major component is iron, with carbon being the primary alloying material. Carbon acts as a binding agent, locking the otherwise easily-moved iron atoms into a rigid matrix. Varying the amount of carbon and its distribution in the alloy controls the qualities of the resulting steel. With the increased carbon, steel is harder and has a much higher tensile strength than iron, but is also more brittle. Reinforced concrete is a composite building material made from the combination of an aggregate mixed with cement binder with interwoven steel rods. Local stresses experienced by the matrix are transferred to the steel which then distributes the stress through the entire structure[7]. In

this respect, reinforced concrete is a large scale equivalent of our polymer/nanotube system.

TEM images of the composite help in understanding why an effective NT concentration exists. Figure 5-11(a) and (b) show images of the 5 wt% and 1 wt% N_Thick samples respectively. The images show that the larger 5 wt% nanotube concentration contains wispy nanotube aggregates while the 1 wt% exhibits excellent nanotube dispersion to the level where each "thick MWNT" has been isolated.

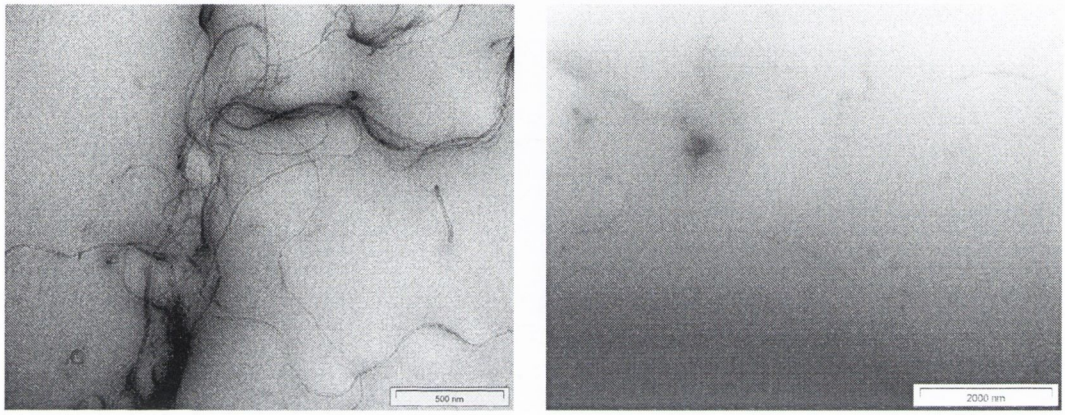

Figure 5-11(a): *TEM of the 5 wt% N_Thick composite [15 min tip]* ***(b)*** *1 wt% [60 min tip]*

The ND sample can now be evaluated bearing in mind that it has been subjected to a less rigorous sonication regime (15 minutes under the sonic tip) relative to the 1 wt% N_Thick composite (60 minutes). A three-fold increase in Young's modulus was observed as shown in Figure 5-10. The fact this is less than that of the 1 wt% N_Thick can be accounted for by studying its TEM image as shown in Figure 5-12(a). The image shows an impressive web of polymer coated nanotubes. When the dimensions of the nanotubes are analysed it is clear that the largest features at 25 ± 5 nm, such as the example marked A, are too large to be individual DWNT. The smaller long uniform rods, marked B, were measured at 5 ± 1 nm suggesting they may be polymer coated individual DWNT. Therefore it is a range of polymer coated bundles and single coated DWNT that exist in the sample. The fact that the ND composite does not match the Young's modulus of the N_Thick sample suggests the nanotube bundles are compromising the reinforcement such that nanotube-nanotube interactions limit the potential strength gain.

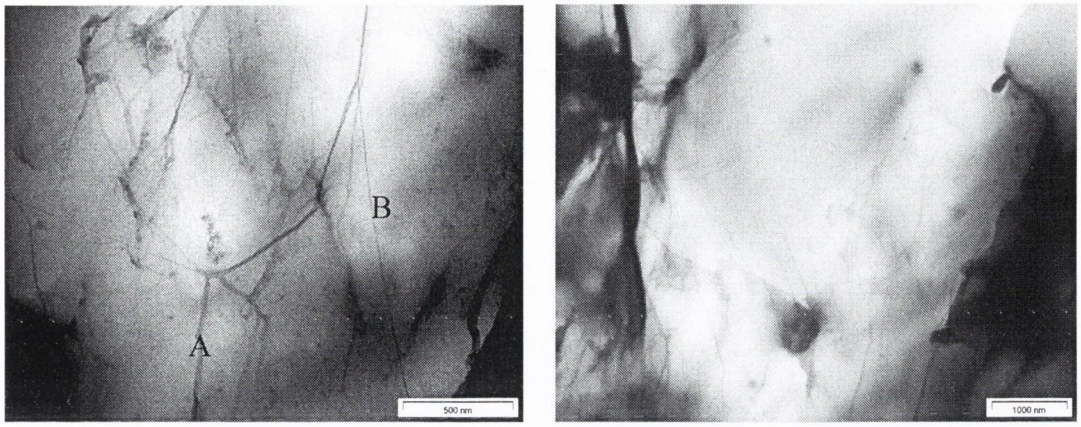

Figure 5-12: *TEM images of 0.5 wt% NDWNT composite film.*

5.8 Differential Scanning Calorimetry (DSC)

DSC measurements were carried out to investigate the polymer crystallinity in the ND composite. The PVOH reference and composite samples were simultaneously prepared ensuring an identical thermal history for each. Under these circumstances, the first heat run provides useful information about the polymer crystallisation that has occurred in composite solution formation and during film drying. In addition, the second heat run represents an entirely different system where the melting curve is attributable to crystal defined by the cooling parameters as opposed to crystals formed during the film drying stage[5]. A single broad endothermic melt peak at 190.81 °C, as shown in Figure 5-13, was observed for the PVOH film as expected for a semi-crystalline polymer. Enthalpy (ΔH) values were calculated by numerical integration of the area under the melting and crystallinity peaks for both samples. This was divided by 138.6 J/g[8], which is the theoretical enthalpy for 100 % crystalline PVOH, to give the actual crystallinity level.

The curve obtained for the first heating step exhibits curvature at 100 °C that is associated with water trapped in the film – since this water evaporates in the first heat run water is absent when the sample is reheated after cooling. The values of the enthalpies calculated for the entire DSC heat-cool-heat cycle are shown in Table 5-1 for both samples.

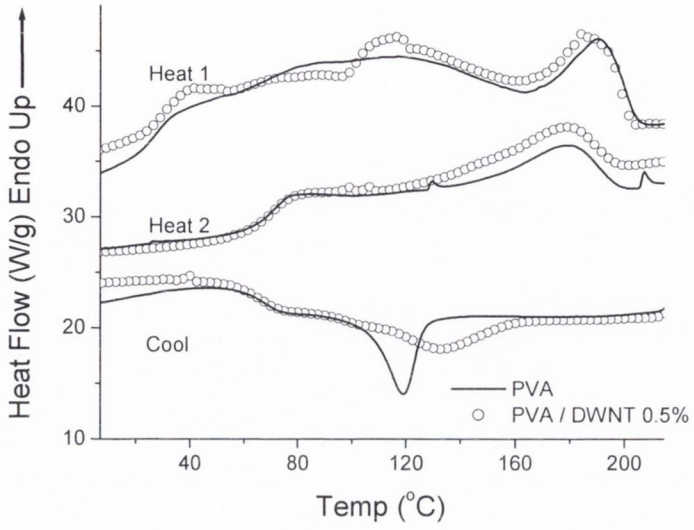

Figure 5-13: *DSC results for PVOH and the ND composite*

Table 5-1: *Enthalpy and Crystallinity values calculated by DSC for ND composite.*

Sample	Step	Peak (°C)	Enthalpy (J/g)	Crystallinity (%)
PVOH	Heat 1	190.81	23.42	16.9
	Cool	119.32	-17.661	
	Heat 2	178.66	22.49	16.2
PVOH/NDWNT	Heat 1	184.71	25.47	18.4
0.5 wt%	Cool	132.15	-17.724	
	Heat 2	177.96	26.834	19.4

From the enthalpy change of the first heat run it can be calculated that the introduction of 0.5 wt% DWNT produces a 1.5 % increase in crystallinity. This implies the nanotubes nucleate crystallinity during film drying. Recall that the same sample exhibited a three-fold increase in Young's modulus suggesting that a small change in crystallinity is sufficient to produce significant changes in mechanical properties.

In addition to analysing the first heat run, important information regarding crystal nucleation can be obtained from the controlled cooling data. Upon cooling from the melt the nanotube sample exhibits a 13 °C increase in the crystallisation temperature (T_c) relative to the PVOH film. This upward shift confirms the nanotubes are acting as nucleation sites for polymer crystallisation in the absence of solvent. This compares well

to a 5 °C increase in T_c reported by Grady et al[9] for polypropylene (PP) doped with 1.8 wt% SWNT. Similarly, Valentini et al[10] reported an almost 20 °C increase in T_c for PP with 20 wt% SWNT. It should be noted that those studies used melt blending to produce the composites and consequently do not have polymer morphology induced during film drying. Secondly, they did not investigate the first heat due to concerns regarding thermal history. Therefore only the cooling and second heating runs of their heat-cool-heat data are useful for comparison purposes. As with PmPV, discussed in Chapter 4, the crystallisation induced by cooling from the melt is entirely different to that produced by slow evaporation of solvent – it is a more "solid-state" like crystallisation since it occurs in the absence of solvent which had been evaporated during the first heat. Table 5-1 shows the enthalpy of melting for the second heating (ΔH_{m2}) is almost 3% higher for the nanotube sample. It is concluded that nanotubes may act as crystal nucleation sites in both the solution and the composite cooling/solid-state phase.

Other groups have observed similar nanotube nucleated crystallinity for a range of materials. Fukushima[11] reported a significant enhancement of ΔH_c for 1-butyl-3-methylimidazolium tetrafluoroborate ($BMIBF_4$) with the addition of 0.5 wt% of SWNT. This is in excellent agreement with the fact our best results occur for low nanotube concentrations. Valentini reports an increase of 3 °C for T_c and an increase in ΔH_c from 9.0 J/g, for neat poly3-octylthiophene (P3OT), to 13.8 J/g for a 1 wt% SWNT/P3OT composite. He concludes: "from these results it can be assumed that SWNTs promote the formation of heterogeneous nuclei with lower energy consumption necessary to reach critical stability for crystal growth"[12,13].

5.9 PANI/ArcMWNT composites

5.9.1 Introduction

A recent collaboration with the Maser group from the Institute of Carbon Chemistry at Zaragoza in Spain provided a timely opportunity to perform DMTA measurements on a range of polyaniline/ArcMWNT composites with nanotube concentrations identical to those found effective for PVOH reinforcement. It will be shown that the storage modulus follows a similar trend with nanotube concentration as reported above for the Young's modulus of PVOH composites. The structure of polyaniline in its half-oxidized emeraldine base (EB) state is shown in Figure 5-14.

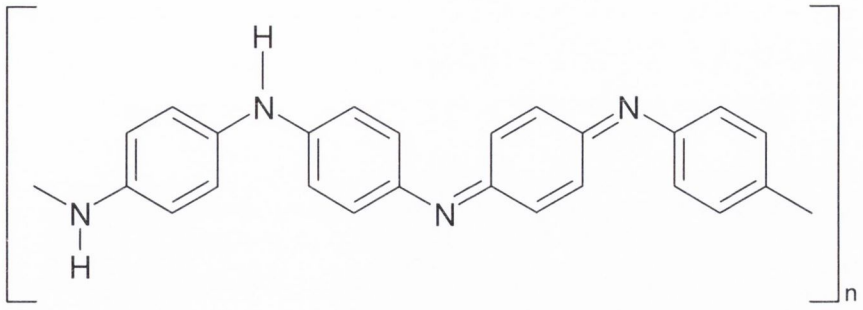

Figure 5-14: *Chemical structure of polyaniline in its half-oxidized emeraldine base (EB) state.*

5.9.2 Material background

The non-conducting soluble emeraldine base (EB) form of polyaniline (PANI) was chosen as a matrix polymer as the conjugated nature of polyaniline is expected to give rise to interesting electronic and morphological properties when interfaced with carbon nanotubes. The synthesis process involves polymerisation of the aniline monomer in the presence of 30 wt% AMWNT. The polymer in the resulting composite is the insoluble emeraldine salt (ES) of polyaniline, therefore a final deprotonation was used to convert the polymer into the soluble emeraldine base (EB) form. This composite EB/AMWNT was in powder form but was easily solubilised in the solvent n-methylpyrrolidinone (NMP). The details of the synthesis process are described elsewhere[14],[15].

Films were cast on glass from the composite solution and required drying in a vacuum oven for 2 hours due to the extremely high NMP boiling point of 202 °C[16]. Unlike similar experiments in the literature no additional annealing was applied with the result a small percentage of NMP has remained in our films. This is deliberate since PANI is a very hygroscopic polymer (like PVOH discussed above) and we expect the level of water and NMP present to be at an equilibrium in each film since all composites received identical drying and storage conditions to minimise deviations in thermal history.

5.9.3 Thermogravimetric analysis

The TGA data of Figure 5-15(a), and the associated derivative curve (b), show NMP evaporation from the film upon heating. The area under the peak between 72 °C and 285 °C in Figure 5-15 remains approximately constant indicating a similar NMP content

for all films although the ArcMWNT fractions above 0.4 wt% exhibited slightly lower solvent content.

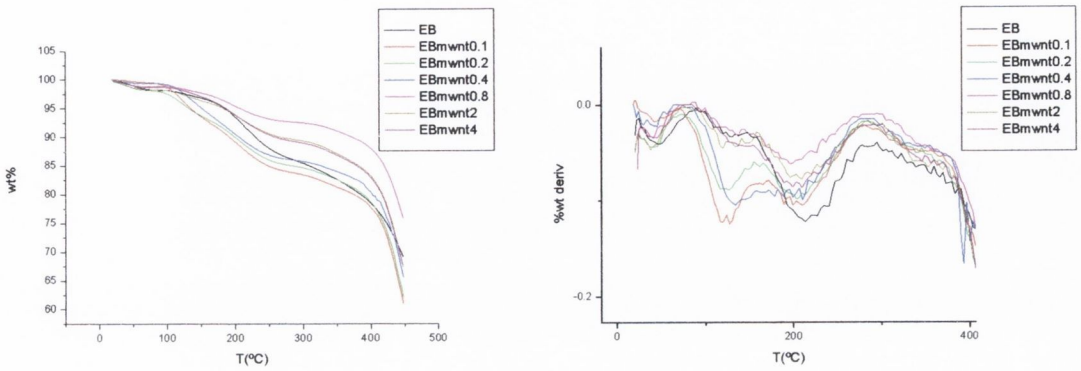

Figure 5-15(a): *TGA data* ***(b)*** *Derivative of (a) for EB/ArcMWNT composites.*

5.9.4 Dynamic mechanical and thermal analysis

Two strips of free-standing film were tested on the DMTA with a temperature range of 20 °C to 350 °C at with a rate of 2 °C/min and frequency of 1 Hz. Nitrogen gas was used to purge the furnace. It is interesting to compare the DMTA results of Figure 5-16(a) with the results described previously for PVOH/nanotube composites.

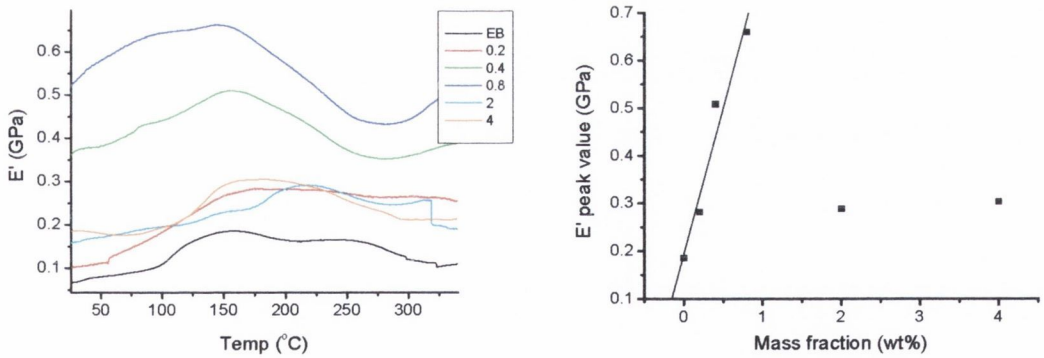

Figure 5-16(a): *E' DMTA results for EB and ArcMWNT composites.* ***(b)****Peak E' values.*

Upon introduction of nanotubes the storage modulus increases linearly with nanotube content up to the 0.8 wt% composite where a peak E' value 3.5 times that of the neat EB film is observed. The further addition of nanotubes was found to be detrimental to the reinforcement, as demonstrated by the low E' values measured for the 2 and 4 wt%. The initial increase in storage moduli followed by a peak at approximately 150 °C reflects the

evaporation of solvent from the system and is consistent with elimination of residual NMP[16] given its high melting temperature. It should be noted that initial concerns suggesting that a high NMP content was responsible for the high modulus exhibited by the 0.8 wt% sample were disregarded given a low solvent content was determined by TGA (Figure 5-15).

Wei et al[17] have studied the effect of NMP content on T_g for cast films of neat EB. They found that the plasticization effect of 20% NMP decreases the T_g to 120 °C from 220 °C for a fully dried sample. Therefore the glass transition at 129 °C in the *Tan δ* data, shown in Figure 5-17(a), is consistent with the glass transition of EB[18] and suggests an upper limit of 20% for the NMP content. The second peak at 207.6 °C is consistent with a transition caused by the evaporation of any remaining NMP. These NMP molecules are expected to be trapped within the film and therefore do not evaporate at the lower temperatures while any surface NMP molecules will have evaporated at lower temperatures.

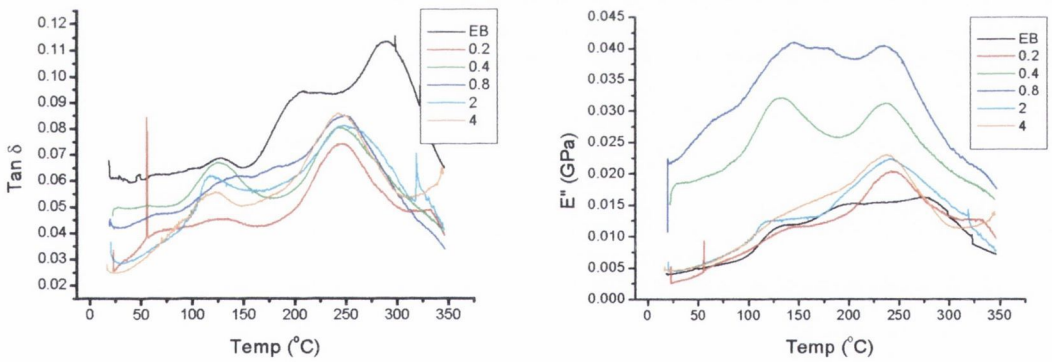

Figure 5-17(a): *Tan δ* ***(b)*** *Loss moduli data for EB/ArcMWNT composites.*

Any transitions below 225 °C are influenced by NMP, above this we are dealing strictly with polymer transitions. Crosslinking between the quinoid groups of the emeraldine base has been reported to occur at temperatures above 250 °C. These reports include DMTA measurements by Han et al[18] identify a peak at 273 °C while Ding et al[19] detect an irreversible reaction, consistent with crosslinking, at 250 °C using modulated DSC – crosslinking is expected to be promoted by chain alignment induced by the applied tensile force during DMTA measurements[20]. The *Tan δ* peak at 288 °C for our samples confirms crosslinking in the neat EB sample while the TGA data of Figure 5-15(a) and the

derivative curve (b) provides further evidence that this is a crosslinking reaction since there is no weight loss observed at 288 °C. With the addition of 0.1 wt% nanotubes the crosslinking temperature is determined to decrease significantly to 247 °C as determined from the *Tan δ* peak of Figure 5-17(a). This indicates a change in thermal conductivity in the sample. In addition, the absence of the second solvent transition observed at 207.6 °C in the *Tan δ* curve for neat EB suggests the nanotubes alter the polymer morphology such that the retention of solvent is limited – this agrees with the results reported above where PVOH/NT composites were less susceptible to moisture absorption due to polymer conformation changes induced by the nanotubes. To confirm polymer morphology changes in the composite as a function of ArcMWNT content SEM will now be presented.

5.9.5 Scanning electron microscopy

In order to investigate the breakdown of polymer reinforcement by nanotubes above 0.8 wt% SEM was carried out for both the 0.8 and 4 wt% composite films as shown in Figure 5-18.

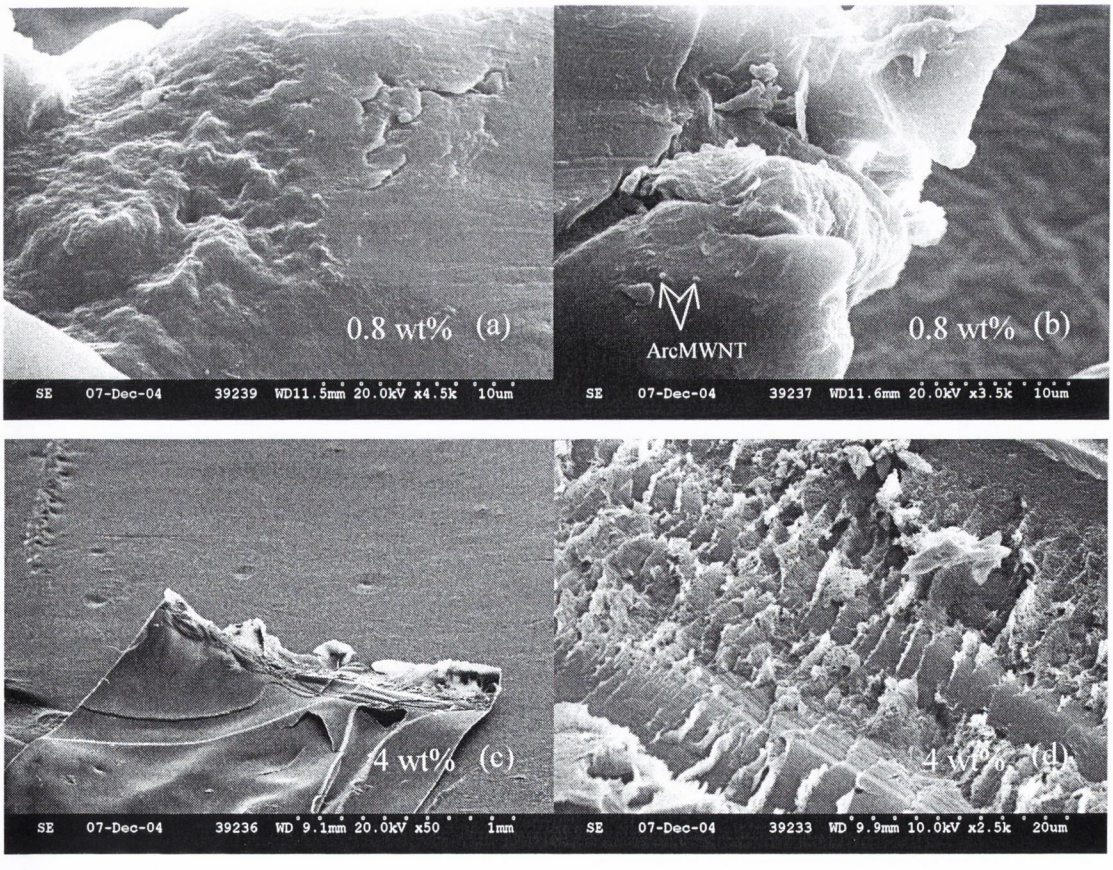

Figure 5-18(a): *SEM of EB 0.8 wt% ArcMWNT, rough fracture edge and smooth surface of film* ***(b)*** *nanotubes protruding from EB 0.8 wt%* ***(c)*** *EB 4 wt% fractured edge* ***(d)*** *higher magnification of 4 wt% suggesting a different fracture surface morphology at the higher nanotube concentration.*

Figure 5-18(a) captured both the rough fracture surface (left) and the smooth surface (right) of the 0.8 wt% composite film. Figure 5-18(b) is a different area of the 0.8 wt% film and arc MWNT can be seen to protrude from the edge. Figure 5-18(d) demonstrates that the fracture surface morphology is significantly different for the 4 wt% composite. The features that resemble planes of PANI that have torn during fracture have been referred to as a "fibril" structure based on recent AFM results performed on similar composites by Sainz et al[15]. These images are typical of the entire fracture surface area for each film. While the promotion of this fibril structure may simply be due to a change in one of the fracture parameters, such as the temperature gradient across the film after immersion in liquid Nitrogen or fracture angle, the DMTA results have previously identified a change in PANI modulus with nanotube concentration. Thus the change in fracture morphology observed in the TEM images may also be attributable to nanotube induced changes in PANI morphology.

5.10 Conclusions

The experiments presented in this chapter have investigated dispersion of carbon nanotubes in PVOH. TEM images show that intensive sonication has achieved nanotube isolation for the largest (N_Thick) nanotubes. Double walled nanotubes (ND) have also been well dispersed to a level where small bundles and isolated polymer coated nanotubes coexist in a web like fashion. It is evident from mechanical measurements that a high nanotube content, such as the 5 wt% that was dispersed in the early aggregation study, is not well dispersed on the nanometer scale and nanotube bundling or aggregation compromises the reinforcement that was observed for lower nanotube concentrations. By refining the nanotube range under investigation the threshold where degradation of mechanical properties occurs was found to exist between 0.5 and 1 wt% for both the Very Thin and Thick nanotubes. Chapter 6 involves a more comprehensive range of nanotube concentrations to study this threshold effect for single, double, thin and arc multi-walled nanotubes. Interestingly, DMTA experiments on the emeraldine base form of polyaniline doped with carbon nanotubes have shown a similar degradation in storage modulus at 0.8 wt%.

In addition to the tensile measurements, that identified a 3-fold increase in Young's modulus for a PVOH matrix doped with double walled carbon nanotubes, DSC measurements show a small increase in the polymer crystallinity (1.5%). This again is consistent with TEM images that show the presence of darker polymer regions around the nanotube web. Meanwhile, the 5-fold increase for well-dispersed 1 wt% thick MWNT proves that to harness the ultimate strength of carbon nanotubes the tubes must be completely isolated from one another within the polymer matrix to maximise the surface area available for crystallisation.

5.11 References

[1] M.S.P. Shaffer, A.H. Windle; "Fabrication and characterization of carbon nanotube/poly(vinyl alcohol) composites.", *Adv. Mat.* **11**, 937 (1999)

[2] J. Liu, A.G. Rinzler, H. Dai, J.H. Hafner, R.K. Bradley, P.J. Boul, A. Lu, T. Iverson, K. Shelimov, C.B. Huffman, F. Rodriguez-Macias, Y.-S. Shon, T.R. Lee, D.T. Colbert, R.E. Smalley; "Fullerene pipes", *Science* **280**, 1253 (1998)

[3] X O. Lourie, D.M. Cox, H.D. Wagner, "Buckling and collapse of Embedded Carbon Nanotubes", *Phys. Rev. Lett.* **81**, 1638 (1998)

[4] D. Qian, E.C. Dickey, R. Andrews, T. Rantell; "Load transfer and deformation mechanisms in carbon nanotube-polystyrene composites", *Appl. Phys. Lett.* **76**, 2868 (2000)

[5] O. Probst, E.M. Moore, D.E. Resasco, B.P. Grady; "Nucleation of polyvinyl alcohol crystallization by single-walled carbon nanotubes", *Polymer* **45**, 4437 (2004)

[6] K.E. Strawhecker, E. Manias; "Structure and Properties of Poly(vinyl alcohol)/Na^+ Montmorillonite Nanocomposites", *Chem. Mater.* **12**, 2943 (2000)

[7] K. Maekawa, A. Pimanmas, H. Okamura; "Mechanics of Reinforced Concrete", *Spon Press*, London (2003)

[8] C.M. Hassan, N.A. Peppas; "Structure and application of poly(vinyl alcohol) hydrogels produced by conventional crosslinking or by freezing/thawing methods" in Advances in Polymer Science, *Springer,* New York (2000)

[9] B.P. Grady, F. Pompeo, R.L. Shambaugh, D.E. Resasco; "Nucleation of Polypropylene Crystallization by Single-Walled Carbon Nanotubes", *J. Phys. Chem. B* **106**, 5852 (2002)

[10] L. Valentini, J. Biagiotti, J.M. Kenny, S. Santucci, *Composites Science and Technology* **63**, 1149 (2003)

[11] T. Fukushima, A. Kosaka, Y. Ishimura, T. Yamamoto, T. Takigawa, N. Ishii, T. Aida; *Science* **300**, 2072 (2003)

[12] L. Valentini, I. Armentano, J. Biagiotti, E. Frulloni, J.M. Kenny, S. Santucci; "Frequency dependent electrical transport between conjugated polymer and single-walled carbon nanotubes", *Diamond and Related Materials* **12**, 1601(2003)

[13] V.B.F. Mathot; "Calorimetry and Thermal Analysis of Polymers", *Carl Hanser Verlag*, Munich (1994)

[14] R. Sainz, A.M. Benito, M.T. Martínez, J.F. Galindo, J. Sotres, A.M. Baró, B. Corraze, O. Chauvet, W.K. Maser; "Soluble and self-aligned carbon nanotube/polyaniline composites", *Adv. Mat.* **17**, 278 (2005)

[15] R. Sainz, A.M. Benito, M.T. Martínez, J.F. Galindo, J. Sotres, A.M. Baró, B. Corraze, O. Chauvet, A.B. Dalton, R.H. Baughman, W.K. Maser; "A soluble and highly functional polyaniline-carbon nanotube composite", *Nanotechnology* **16**, S150 (2005)

[16] P.C. Rodrigues, G.P. de Souza, J.D. DA Motta Neto, L. Akcelrud; "Thermal treatment and dynamic mechanical properties of polyaniline", *Polymer* **43**, 5493 (2002)

[17] Y. Wei, G.W. Jang, K.F. Hsueh, E.M. Scherr, A.G. MacDiarmid, A.J. Epstein; "Thermal transitions and mechanical properties of films of chemically prepared polyaniline", *Polymer* **33**, 314 (1992)

[18] M.G. Han, Y.J. Lee, S.W. Byun, S.S. Im; "Physical properties and thermal transition of polyaniline films", *Synth. Met.* **124**, 337 (2001)

[19] L. Ding, X. Wang, R.V. Gregory; "Thermal properties of chemically synthesized polyaniline (EB) powder", *Synth. Met.* **104**, 73 (1999)

[20] A.G. MacDiarmid, T. Y. Mint, J.M. Wiesinger, E.J. Oh, E.M. Scherrt, A.J. Epstein; "Towards optimization of electrical and mechanical properties of polyaniline: is crosslinking between chains the key?", *Synth. Met.* **55-57**, 753 (1993)

CHAPTER SIX: EFFECT OF NANOTUBE DIAMETER ON MECHANICAL AND MORPHOLOGICAL PROPERTIES OF CARBON NANOTUBE – PVOH COMPOSITES

6.1 Introduction

In Chapter 5, a study of the effect of sample environment on polymer reinforcement identified a narrow range of nanotube loading fractions for effective reinforcement in PVOH/Carbon nanotube composites. This chapter progresses from the previous work and characterises PVOH composites within the optimum nanotube concentration range. Elicarb SWNT, Nanocyl DWNT, Zaragoza Thin MWNT and Arc MWNT were specifically chosen to investigate any effect that carbon nanotube diameter may have on polymer morphology and mechanical properties of the composite. Light scattered by the composite solutions is measured using a UV-Vis spectrometer to qualitatively estimate the amount of carbonaceous material lost during sedimentation. Free-standing composite films are then cast from the solutions and cut into the appropriate geometry for calorimetry and mechanical testing. DSC will be used to measure any nanotube induced changes in polymer morphology and dynamic cooling data is used to monitor the crystallisation process. In this way any effect of nanotube diameter on crystal nucleation can be identified. Tensile testing in conjunction with DMTA will be used to evaluate the mechanical performance with respect to the corresponding crystallinity data. It will be shown that low nanotube volume fractions are most effective at nucleating polymer crystallisation and models fitted to the DSC and tensile data are consistent with the formation of a crystalline polymer coating at the polymer-nanotube interface.

6.2 UV-Vis: Determination of nanotube content

TGA can be used to determine the nanotube content of the Arc_MWNT composite since the nanotube decomposition temperature at 830 °C is well removed from the polymer decomposition peaks. However, the low decomposition temperature characteristic of CVD tubes implies that the nanotube decomposition peak overlaps those of the polymer in the other composites. Therefore UV-vis spectroscopy was assessed as a method of estimating the nanotube content. Reference UV-Vis absorption spectra were initially taken for de-ionised water (DI) and a DI/PVOH solution as shown in Figure 6-1. Spectra taken before and after decantation were then used to monitor the quantity of nanotubes retained in solution for a range of nanotube composites. Each of these "stock" solutions

initially contained 0.5 wt% of the selected carbon nanotubes and received identical sonication/decantation treatment - It should be noted that while the nanotube rich powder is referred to as "carbon nanotubes", there will be varying degrees of impurity depending on whether the CVD or Arc synthesis route has been used as discussed in Chapter 2. The absorption spectra were captured from stock solution diluted with deionised water in the ratio 1:2.5 to remain within the absorption limit of the spectrometer. Deionised water was used for this to maintain the 0.5 wt% nanotube to polymer ratio.

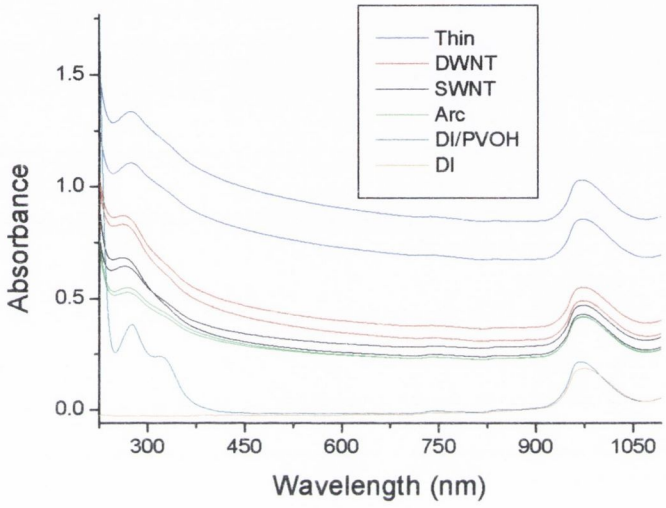

Figure 6-1: *UV-Vis spectra before and after decantation for de-ionised water, PVOH solution and the stock 0.5 wt% composite solutions.*

Using the Beer-Lambert law, the absorbance, A, is proportional to the concentration of the absorbing species, c, according to the equation $A=cl\varepsilon$ where l is the path length and ε is the molar absorption co-efficient. Since the same cuvette is used for all measurements the path length is constant, as is the molar absorption co-efficient since the absorbing species is identical for each "before and after" experiment. Therefore the ratio of highest (before decantation) to the lowest (after decantation) absorption, at a specified wavelength, gives the fractional decrease in the concentration of the absorbing species. This corresponds to the quantity of nanotubes lost from the original 0.5 wt% solution. The absorbance was measured at a wavelength of 800 nm for all samples. The Thin MWNT/PVOH composite exhibits the largest decrease in absorption after settling, confirming the loss of a large amount of nanotubes. 20% of the Zaragoza material sedimented out of solution resulting in a reduction of the nanotube concentration from the original 0.5 wt% to a value of 0.4 wt%. Lower losses of 16% and 14% were observed for the DWNT and SWNT,

respectively. This was as expected since these tubes had been supplied in a purified form. While only 1% of material was determined to have fallen out of the Arc_MWNT composite solution by the UV-Vis method, TGA experiments suggest a more realistic loss of 60%. It is concluded that the UV-Vis method, while useful to compare the absorption intensity of one nanotube/polymer solution to another, does not accurately establish the nanotube concentration. However, the technique is useful to determine an upper limit for nanotube mass fraction: the real nanotube content is expected to be significantly lower than the value determined by UV-Vis spectroscopy.

In summary the data indicates that the upper bound for the nanotube mass fraction is 0.4 wt% for each of the stock solutions. 0.4 wt% transforms to 0.3 vol% using Equation 4-1. These stock concentrations were then blended with pure PVOH solution to create a range of volume fractions where each sample had 50% less than its predecessor. Thus the concentrations studied were 0.3, 0.15, 0.08, 0.04, 0.02 vol%. It should be noted that the "divide by two" blending procedure rapidly tends towards lower nanotube concentrations which are of interest based on the results of Chapter 5.

6.3 TEM characterisation

The quality of dispersion after 15 min sonication with the tip has already been imaged for ThickMWNT and DWNT in Chapter 5. Figure 6-2(a) verifies the high purity of the pristine SWNT nanotubes while (b) shows the image obtained for the 0.3 vol% SWNT composite.

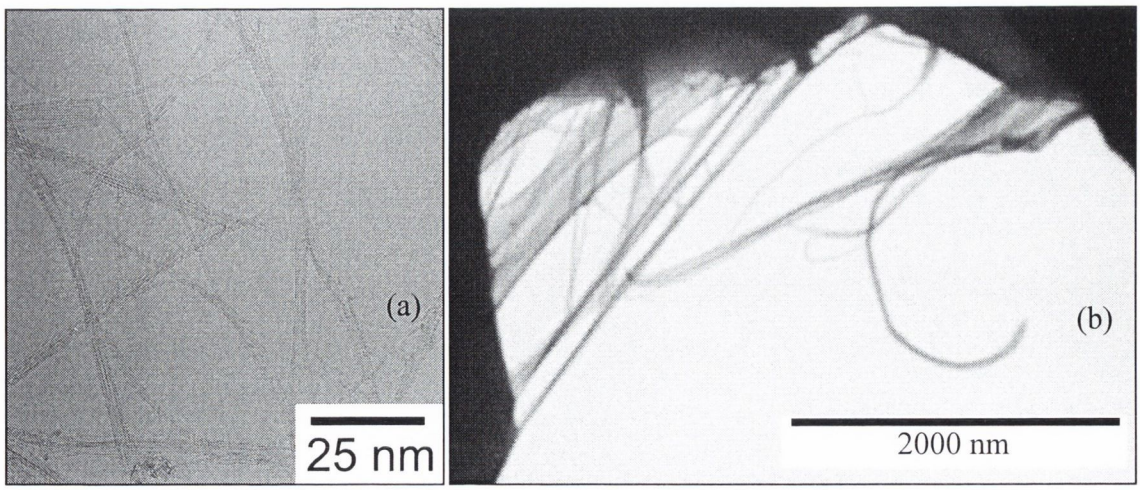

Figure 6-2(a): *Pristine SWNT (image supplied by Elicarb).* ***(b)*** *0.3 vol% SWNT/PVOH composite.*

Polymer coated SWNT bundles can be seen bridging the rough edge of the film. The typical length of bundles extends to almost 10 μm, as demonstrated by Figure 6-3(a) which has been compiled using three TEM images captured at the edge of the 0.3 vol% SWNT composite film.

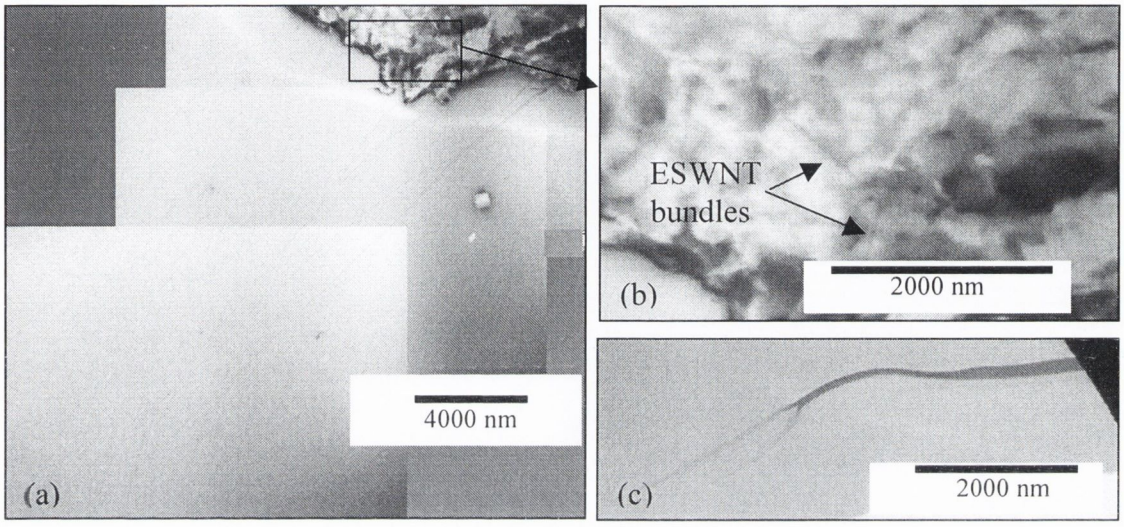

Figure 6-3(a): *Long tubes protruding from edge of 0.3 vol% SWNT/PVOH composite* ***(b)*** *well-defined structures appear to be SWNT bundles embedded in body of film* ***(c)*** *Bundle recoil and separation with TEM induced polymer melting indicating polymer intercalation between aggregates of SWNT bundles.*

Figure 6-3(b) suggests that the body of the composite film contains well-dispersed SWNT bundles rather than individual SWNT while Figure 6-3(c) has captured a polymer coated structure recoiling and separating due to TEM induced polymer melting. It would appear from the dimensions of the structure that it comprises of a number of SWNT bundles which were bound together via a polymer coating. The separation of the bundles upon melting of the polymer is highly significant as it suggests polymer intercalation between the bundles. It is not possible from this image to determine if there is additional polymer intercalation within the individual bundles.

6.4 SEM characterisation

A previous paper published by our group[1] used SEM to measure the fracture surface of PVOH/Thin MWNT after tensile tests. Upon examination Thin MWNT were observed to protrude from the fracture surface. In order to study composite morphology in the absence of tensile effects, the composite films in this work were fractured by dipping the composite strip half way into a flask of liquid Nitrogen and immediately snapped in two.

SEM is especially useful as the images will reflect the final composite structure after the multi-layer deposition sequence and drying has been completed. This is in contrast to TEM which measures an entirely different system where the nanotubes protrude at the edges of a thin polymer film. The SEM images of these films are shown in Figure 6-4.

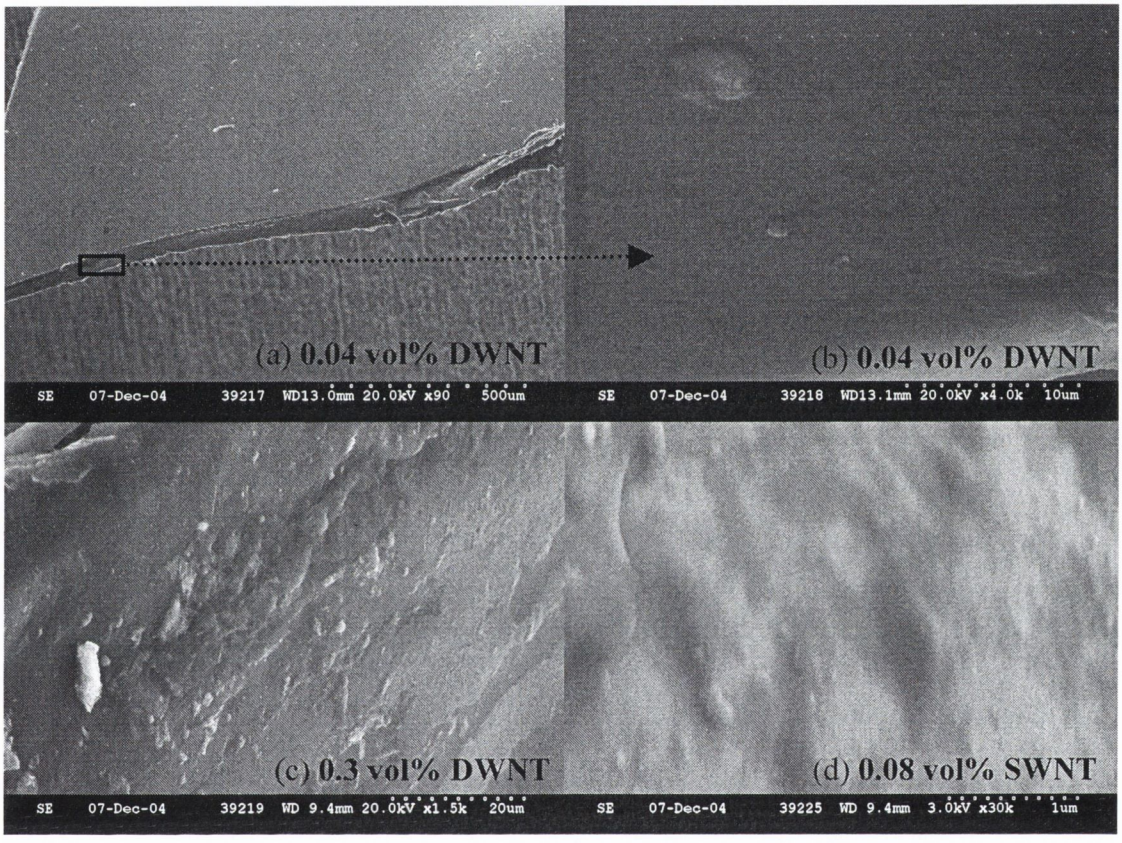

Figure 6-4(a): *Image of 0.04 vol% DWNT film strip* ***(b)*** *Fracture surface of (a)* ***(c)*** *0.3 vol% DWNT, many nanotube bundles/aggregates protrude from the fracture surface* ***(d)*** *0.08 vol% SWNT (note the smaller scale bar (1μm) relative to other images) SWNT bundles are observed to protrude from the fracture surface. Blurring occurs due to SEM induced melting of the polymer.*

Comparing the image of the 0.04 vol% DWNT film, Figure 6-4(b), to that of the sample which contains 8 times the quantity of nanotubes, 0.3 vol% DWNT as shown in Figure 6-4(c), is it is clear that the number and dimensions of the bright features is related to the nanotube concentration. It is difficult to specify exactly what material is present in each of these features. It is possible that they are nanotubes that have aggregated or polymer coated nanotubes that have aggregated together. DSC measurements of strips of the same film will be presented in Section 6-5 to identify the polymer crystallinity within these films. Apart from two large features, the 0.04 vol% DWNT film has well dispersed small aggregates ranging from 150-300 nm. The formation of these small aggregates is unsurprising given the efforts that were required to eliminate large-scale aggregation, a

study of which was presented in Chapter 5. In addition, studies by Strawhecker et al[2] that have extensively described crystal formation in drop cast films of PVOH/sodium montmorillonite composite. These films are initially mostly amorphous and crystallites initiate predominately in the final drying stages. Crystallisation proceeds slowly during drying, aided by the ambient humidity. If the ambient humidity is too low or absent, the drying polymer becomes glassy, and crystal growth becomes arrested before extended crystallites can develop. Figure 6-4(c) of the 0.3 vol% DWNT shows the dominance of larger circular crystallites that ranging from 200 nm to 700 nm in diameter. A small number of larger features are also present, the largest being 3 μm wide. The variation in the dimensions and number of features per unit area suggests that the nanotubes do not remain perfectly dispersed as the cast solution slowly dries. Some level of aggregation is expected given the fluid dynamics and air currents within the fan-assisted oven that are not easily controlled. SEM therefore shows that the composite films are comprised of a polymer matrix embedded with features that increase with nanotube content. These features therefore contain nanotubes or polymer-coated nanotubes. Higher magnification images of the films could not be obtained due to heating effects which resulted in melting of the polymer matrix. Figure 6-4(c) demonstrates the effect of heating on the 0.08 vol% SWNT sample where the melting polymer moves during the exposure time producing a blurred image. DSC will now investigate the exact nature of the polymer morphology within the films and determine how the polymer morphology is altered in the presence of carbon nanotubes.

6.5 DSC characterisation of PVOH/Nanocyl DWNT composites

Crystallinity measurements were carried out on strips of the same films as imaged using TEM and SEM. The goal of this work was to specify the effect of carbon nanotubes on polymer morphology as a function of diameter. At this point it is useful to recall the importance of the first heat run of the DSC heat-cool-heat cycle. As discussed for PmPV in Chapter 4, the first heat run is usually disregarded as a thermal history elimination procedure. However, for the experiments in this thesis, the first heat run is valid as it measures the morphology induced by controlled evaporation of solvent from the drop cast films. In PVOH the first heat run is crucial as degradation effects induced by the first heating step often compromise the second heating data[3,4,5]. For this reason the upper temperature limit used for DSC heating was 220 °C (the end of the melting transition) for all PVOH measurements presented in this thesis.

To understand these composite systems it is useful to further clarify exactly what constitutes a "crystallinity increase". An increase in crystallinity can occur in two ways. Firstly, consider the melt peak characteristic of a polymer – the shape and peak temperature of this curve are reflective of the crystallites that form during drying in the absence of a filler material. Upon addition of carbon nanotubes the polymer peak may increase in area without a shift in melt temperature indicating the crystallite conformation has not changed but there exists a greater number of crystals exhibiting the structure that is inherent to PVOH. This constitutes an increase in crystallinity. The polymer peak may also exhibit an increase in melt temperature (T_m). A higher T_m implies that more thermal energy is required to destroy the crystals and that these crystallites have greater intermolecular bonding, reflecting a more perfect crystalline structure which can be termed an increase in crystallinity. Thus the sharpening, broadening or shift in temperature of a melt peak reflects different information about information the quantity and structure of polymer crystals. The full width half maximum (fwhm) of the peak can be used to determine the range of crystallite sizes present in a system while the peak temperature indicates the degree of order.

In this thesis the samples exhibiting a low fwhm will be referred to as having well-defined crystallinity. Samples containing crystals with high T_m values will be referred to as having a more perfect structure. In summary, an increase in crystallinity for a polymeric material may refer to an increase in the number of crystals of a specific conformation and/or an increase in the number of more perfect crystals. The DSC results of Figure 6-5 are from the first heat run of the PVOH/DWNT composites and illustrate the distinction between the two types of crystallinity enhancement.

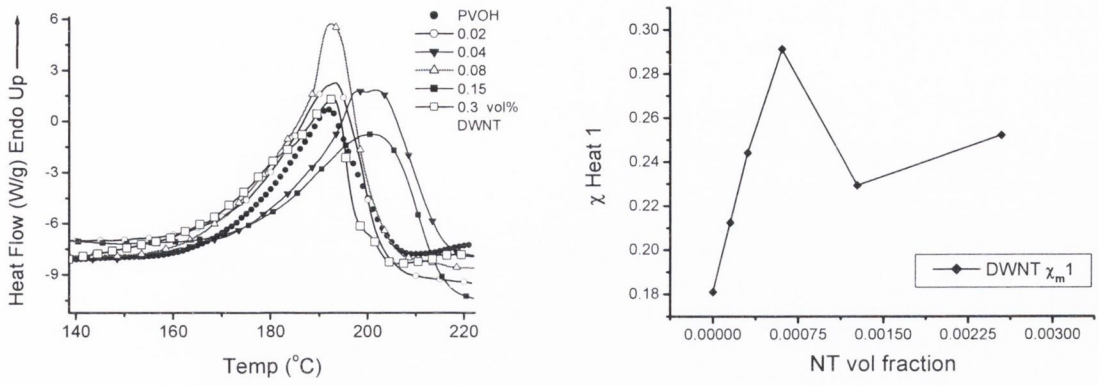

Figure 6-5(a): *DSC first heat run data for the PVOH/DWNT composites* ***(b)*** *Crystalline fraction, χ, as a function of nanotube volume fraction for the DWNT samples.*

The 0.08 vol% DWNT film was calculated to be the most crystalline using the equations and techniques introduced in Chapters 4 and 5 for DSC analysis. The crystalline fraction, χ, is plotted as a function of volume fraction in Figure 6-5(b). The sharp peak observed for the 0.08 vol% DWNT sample in Figure 6-5(a) and the high χ value, shown in Figure 6-5(b), confirms a well-defined crystal structure. Bhattacharyya et al[6] observed a similar sharpening of the melting peak for a 0.8 wt% SWNT/ polypropylene (PP) composite relative to neat PP and suggested this indicated a narrow crystallite size distribution in the PP/SWNT composite.

In our data, an 8 °C increase in T_m is observed for 0.04 vol% and 0.15 vol% DWNT composites which is also characteristic of a change in crystal structure relative to the neat polymer. In addition, the fwhm of those 0.04 vol% and 0.15 vol% DWNT samples is approximately 7 °C more than that of the 0.08 vol% DWNT sample indicating that a range of more perfect crystallite conformations exist within the 0.04 vol% and 0.15 vol% DWNT films. However, upon increasing the volume fraction further a decrease in crystallinity results with the 0.3 vol% melt peak decreasing back to that associated with the neat PVOH. To investigate if a trend existed for crystallinity as a function of nanotube volume fraction the melting temperature data for the other nanotube types was plotted as shown in Figure 6-6.

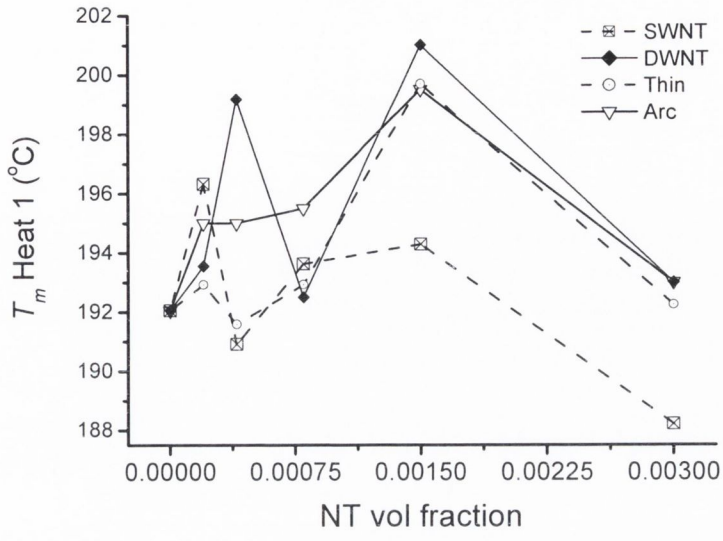

Figure 6-6: *Composite melting temperature as a function of nanotube volume fraction.*

Given the number of data sets obtained for each of the nanotube types the explicit DSC data will be shown for the DWNT composites while only the pertinent enthalpy and peak temperature data will be plotted for the remaining nanotube types.

T_m was generally observed to increase with nanotube loading up to a threshold value that was approximately the same for all nanotube types (0.15 vol% in each case). Above the threshold the crystallinity dramatically decreased to approximately that of the pure polymer. This is unsurprising since the range of nanotube concentrations was carefully engineered based on the results of Chapter 5 where high nanotube concentrations were shown to have poor mechanical properties.

Since an increase in T_m was observed for the 0.04 vol% and 0.15 vol% DWNT samples but <u>not</u> the 0.08 vol% it must be concluded that the crystal structure of the 0.08 vol% sample deviates slightly compared to the adjacent volume fraction. It is too great a leap, based on the number of data points plotted in Figure 6-6, to assume that at 0.08 vol% the nanotube concentration was just perfect for inducing a well-defined crystal structure that had a lower T_m than the adjacent concentrations. Therefore, a processing or drying anomaly may be the root cause of this change in crystal structure. Although the cause cannot be confirmed for the drop in T_m, the sample is still the most crystalline since it has

the crystalline fraction, χ. Tensile data that will now be introduced to show that the 0.08 vol% sample, in addition to being the most crystalline, was found to exhibit the best mechanical properties.

6.6 Tensile testing of PVOH/Nanocyl DWNT composites

Tensile measurements were carried out to evaluate the relationship between composite morphology and mechanical performance. The data was used to calculate Young's modulus (Y), tensile strength (σ_T) and toughness (T) values. Figure 6-7 shows that the σ_T and Y were maximised for 0.08 vol% DWNT sample. This was an excellent result as it confirmed the preliminary results of Chapter 5 that determined reinforcement should be maximised at low nanotube concentrations.

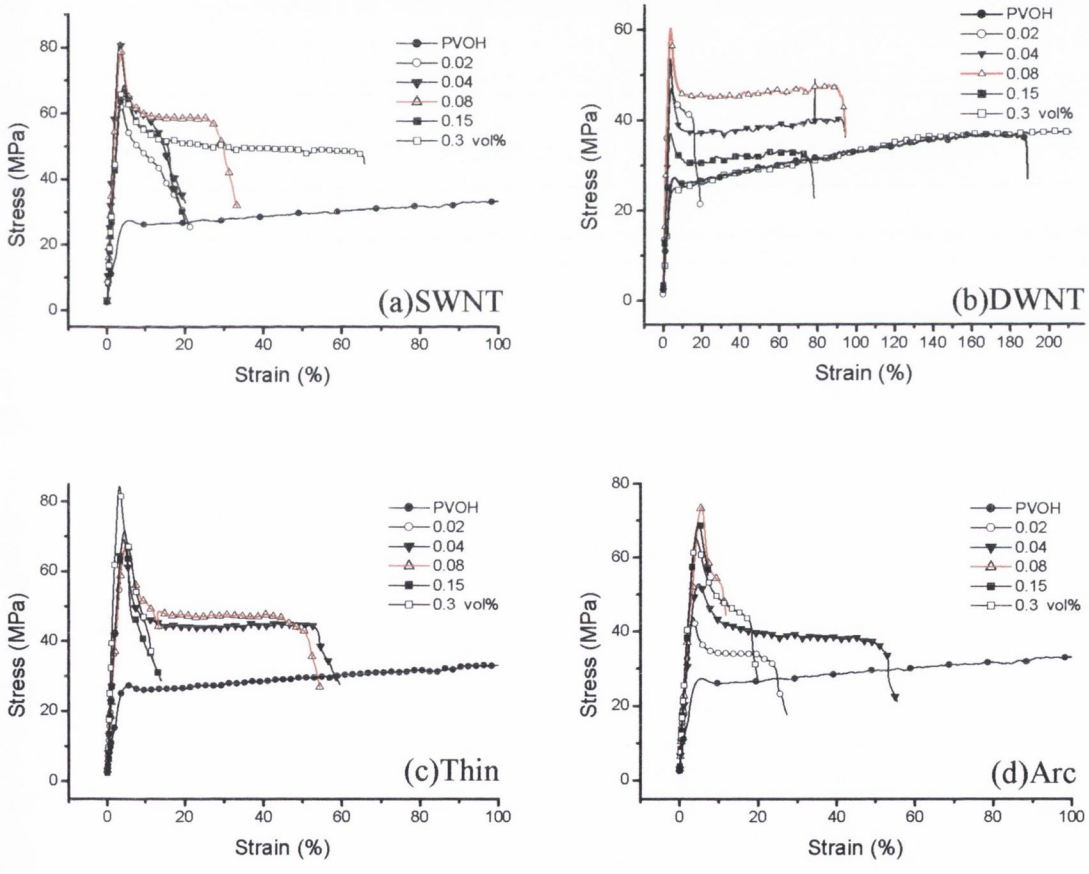

Figure 6-7: *Tensile data for PVOH and (a)SWNT (b)DWNT (c) ThinMWNT (d)Arc nanotube composites.*

It is emphasised that the sample with the well-defined crystalline structure, 0.08 vol% DWNT, exhibited the greatest reinforcement followed by the samples that display a range of more perfect crystals. This suggests that is a well-defined crystal structure that gives rise to the most effective reinforcement rather than the level of crystal perfection. The

ultimate reinforcement would be expected if crystal perfection could be attained without loss of definition: a DSC trace for this scenario would be a sharp peak at a higher T_m relative to the neat polymer curve.

A graph of Y and crystalline fraction (χ) against absolute volume fraction for DWNT is shown in Figure 6-8 verifying the remarkable agreement between these two characteristics – maximum crystallinity occurs at low volume fractions and the best mechanical performance is observed for maximum crystallinity.

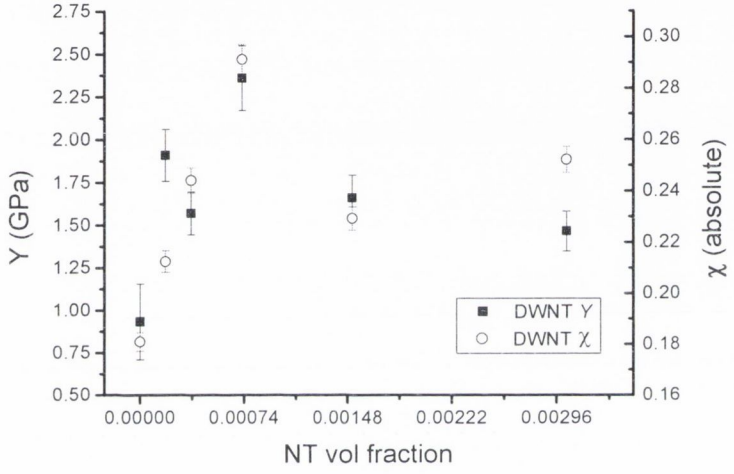

Figure 6-8: *Plot of Y and χ v's nanotube volume fraction.*

Enhancing the crystallinity of a polymer is widely acknowledged to improve its mechanical properties[7]. This is because alignment of the chains and reduction of chain movement, characteristic of crystallisation, increases the stiffness of the material. The melting point of the material also increases with the increased intermolecular forces that can be associated with the reduced interchain separation achieved by crystallisation. Nanotube/polymer composites have therefore been the subject of many recent crystallisation studies. The polypropylene (PP)/SWNT experiments discussed previously in Chapter 5 are mentioned again here with respect to their interesting melting endotherms. The relevant graph and caption are reproduced from Grady et al[8] in Figure 6-9.

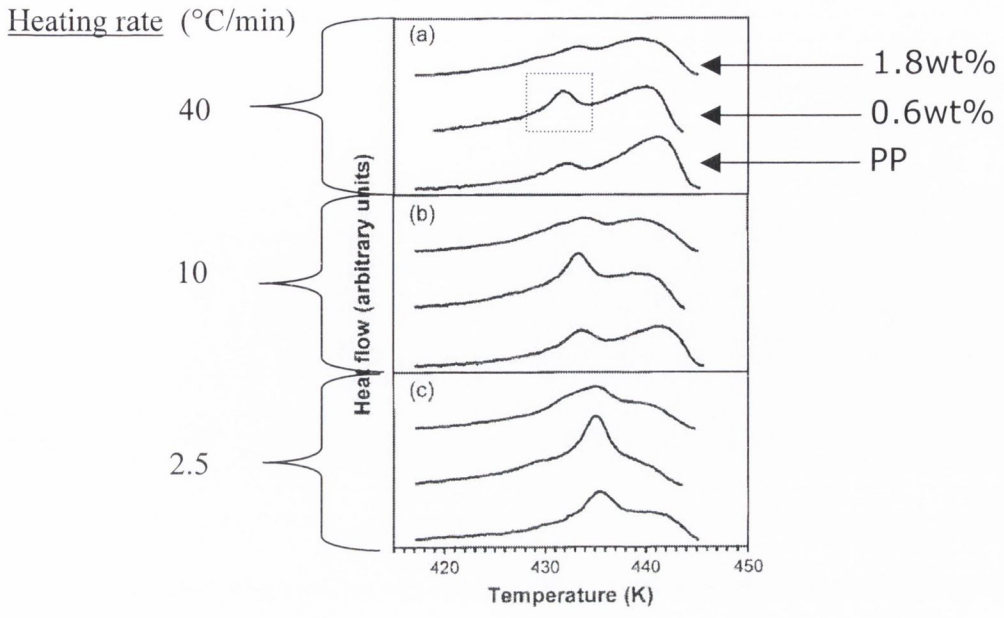

Figure 6-9: *DSC melting curves for Polypropylene/SWNT composites (0, 0.6, 1.8 wt%). In each graph the lower curve is that of PP, the highest is the 1.8 wt% and 0.6 wt% is in between. Heating rate is* ***(a)*** *40 °C/min* ***(b)*** *10 °C/min* ***(c)*** *2.5 °C/min. Data reproduced from Grady et al*[8]

Figure 6-9(a) is of most interest since the heating rate is identical to that used for the PVOH work presented in this thesis. It is clear that the PP alpha phase peak, highlighted by the dashed rectangle in Figure 6-9(a), has a smaller range of crystallite sizes in the 0.6 wt% than in the 1.8 wt%. Thus the 0.6 wt% has more well defined crystallinity than the higher 1.8 wt% composite. This is further evidence of a threshold for nanotube loading above which crystallinity decreases.

Tensile and DSC data plots, similar to those for DWNT shown above, were obtained for SWNT, ThinMWNT and Arc_MWNT. All results were compiled and plotted together allowing direct comparison of their performance. The results show that for all nanotube types Y was maximised at nanotube fractions values below 0.1 vol%. The samples shown to have the highest Y and strength (σ_T) using tensile testing were also the most crystalline proving a link between nanotube induced polymer morphology and mechanical performance. Figure 6-10(a) clearly shows the initial increase in crystallinity followed by a decrease with higher nanotube loading.

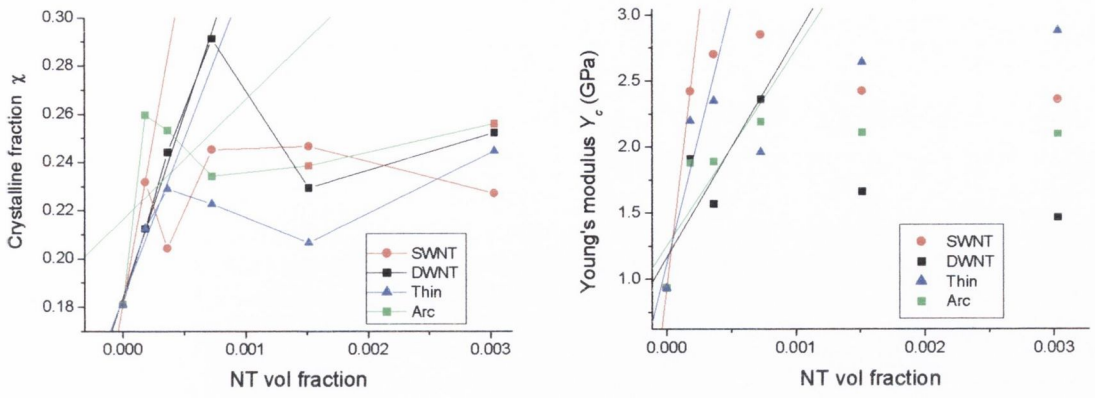

Figure 6-10(a): *Crystalline fraction, χ, against nanotube volume fraction* ***(b)*** *Young's modulus, Y, against nanotube volume fraction for all nanotube types.*

Inspite of scatter in the data of Figure 6-10, there is clearly a trend towards a linear increase in both crystallinity, χ, and modulus, Y, at low nanotube volume fractions (<0.1 vol%). The scatter in the data arises from the permeability of the PVOH matrix to atmospheric moisture although, as discussed in Chapter 5, a number of experimental controls were implemented in order to limit water absorption. The most direct route to assess the relationship between crystallinity and modulus is to plot χ against Y, a plot which is expected to be linear based on the DWNT composite results presented in Figure 6-8. The plot of χ against Y is shown in Figure 6-11.

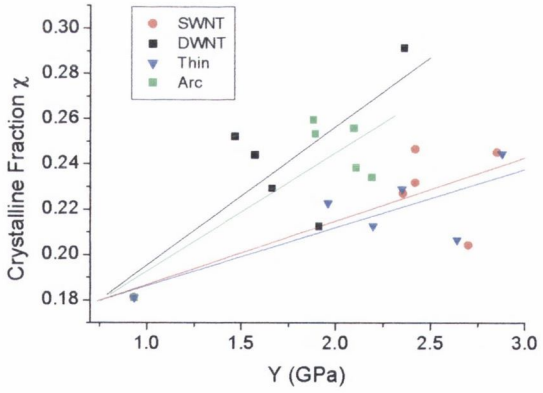

Figure 6-11: *Crystalline fraction, χ, against Young's modulus,* Y, *for all nanotube types.*

A linear fit agrees well for the SWNT and Thin MWNT. However, the DWNT and Arc data exhibit scatter about the fits. The goal of this analysis was to use the slopes of these fits to evaluate if a preferential nanotube diameter exists for polymer reinforcement at low fractions. An alternative approach is to apply a linear fit to the low nanotube

concentration data of Figure 6-10. This averages over the data points and any data points that deviate from linearity are accounted for in the error of the fit. A plot of dY_c/dv_f against $d\chi/dv_f$ should be linear if the statement that maximum reinforcement is observed for maximum crystallinity is true. Figure 6-12 proves this is indeed the case and the large error bars reflect the scatter in the data observed above in Figure 6-11 for the plot of χ against Y.

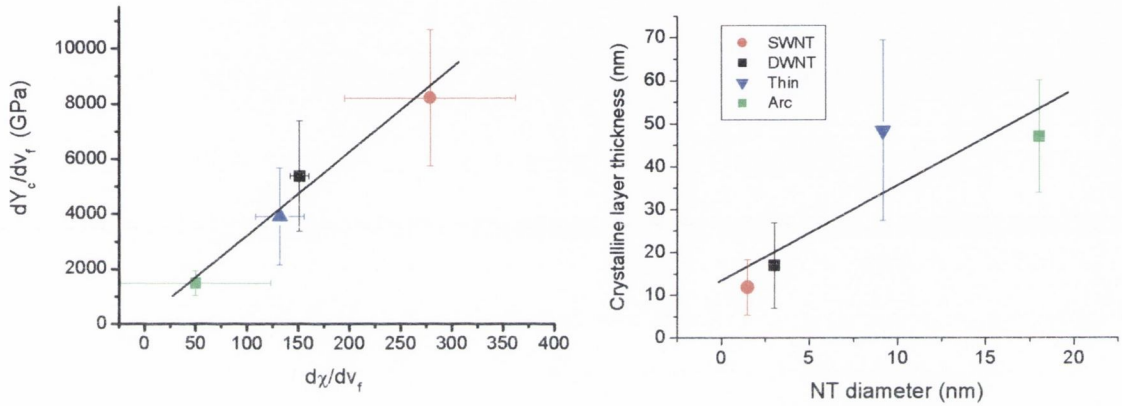

Figure 6-12(a): *Plot of dY/dv_f versus $d\chi/dv_f$* ***(b)*** *Crystalline layer thickness, b, as a function of nanotube diameter. Identical legend for both graphs.*

Equation 6-1 is now recalled from Chapter 4.

$$\frac{d\chi}{dv_f} \cong 2\frac{b}{r_{nt}} + \left(\frac{b}{r_{nt}}\right)^2 \qquad \textit{Equation 6-1}$$

This equation allows calculation of the thickness, b, of a crystalline coating around the carbon nanotube based on a model of the semi-crystalline polymer/nanotube interface. The calculated thicknesses are plotted as a function of nanotube diameter in Figure 6-12(b). TEM images of the pristine thin MWNT, such as that shown in Figure 6-13, were supplied by the Zaragoza group and used to determine an average thin MWNT diameter of 9 ± 3 nm.

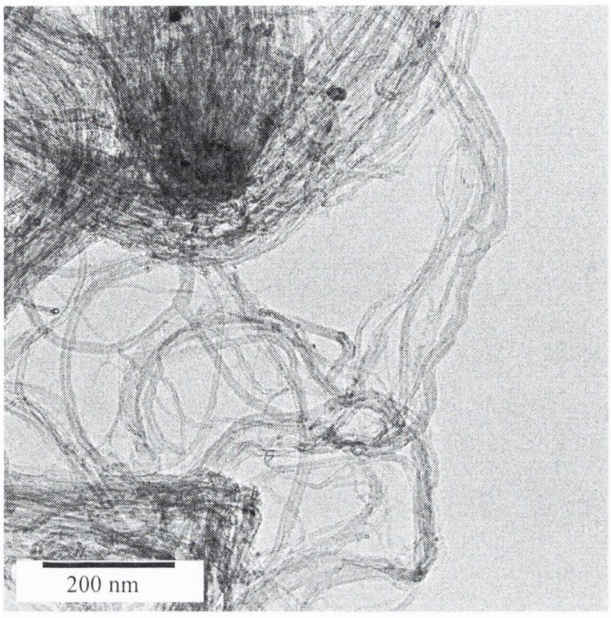

Figure 6-13: *TEM image of thin MWNT (Z_thin) supplied by the University of Zaragoza.*

6.7 Analysis of reinforcement: Short fibre theory

Krenchel's expression for short carbon fibre composites[7,9,10,11], as shown in Equation 6-2, was used to calculate the nanotube moduli, Y_{nt}, based on the measured composite moduli, Y_c, previously shown in Figure 6-10(b).

$$Y_c = Y_p(1 - v_f) + \eta_l \eta_0 Y_{nt} v_f \qquad \textit{Equation 6-2}$$

$$\eta_l = \left(1 - \frac{\tanh\left(\frac{\beta l_{eff}}{2}\right)}{\left(\frac{\beta l_{eff}}{2}\right)} \right) \qquad \beta = \sqrt{\frac{-4G}{r_{nt}^{\,2} Y_{nt} \ln\left(v_f\right)}} \qquad G = \frac{Y_p}{2(1+\upsilon)}$$

$$\eta_0 = \sum_n a_{fn} \cos^4 \alpha_n \,/\, \sum_n a_{fn}, \; where \sum_n a_{fn} = 1$$

Y_{nt} is the nanotube modulus, l_{eff} is the effective nanotube length, v_f is the volume fraction, r_{nt} the nanotube radius. G is the polymer shear modulus which is calculated from the expression $G=Y_p/2(1+v)$ where v is the Poisson's ratio and Y_p is the polymer modulus. η_l represents the fibre length correlation factor and η_0 is the Krenchel orientation efficiency

factor. Random planar arrangement has been assumed for the PVOH/Carbon nanotube composites implying a theoretical orientation factor of 0.38[12]. Studies of PVOH/Carbon nanotube composites by Shaffer et al[13] used X-ray analysis to measure a η_0 value of 0.33 validating the assumption of random planar configuration.

For the η_l term, the Poisson's ratio, ν, of 1/3 is substituted for PVOH into the G term so that the two remaining variables are l_{eff} and Y_{nt}. Therefore to fit Equation 6-2 to the Young's modulus data of Figure 6-10(b) l_{eff} and Y_{nt} ideally should be left as free parameters. However, it was found that these two parameters are highly correlated to one another[1] and therefore could not be reliably determined from a fitting procedure to the data set when both are variable - a larger data set would be required to enable confident determination of the fibre length correlation factor, η_l. As an alternative approach, an effective modulus for the nanotube was defined as $Y_{eff} = \eta_l Y_{nt}$. Therefore, the effective nanotube modulus will be a low estimate of the true nanotube modulus, Y_{nt}, since η_l will be less than unity. Substituting into Equation 6-2 gives:

$$Y_{eff} = \frac{\frac{dY_c}{dv_f} + Y_p}{\eta_o} \qquad \textit{Equation 6-3}$$

Y_p has been measured as 0.9 ± 0.2 GPa, η_0 = 0.38 for random planar orientation[12] and dY_c/dv_f can be calculated by a linear fit as shown in Figure 6-10(b). Effective nanotube moduli have therefore been calculated as 14 ± 7 TPa (SWNT), 14 ± 7 TPa (DWNT), 10 ± 5 TPa (ThinMWNT) and 4 ± 1.5 TPa (Arc). These values do not agree well with recently reported elastic moduli values for carbon nanotubes[14]. The values are for the CVD nanotube are at least an order of magnitude too high since the expected values range from about 300 GPa to 900 GPa depending on the defect concentration of the nanotube. The ArcMWNT modulus is also too high given the literature value of 850±410 GPa[14] for well-graphitized Arc MWNT. This disagreement between theoretical and experimental Y_{nt} values implies that Krenchel's rule does not apply and the assumption for the rule is not true for the PVOH/Nanotube composites: Krenchel assumed that polymer morphology is not significantly altered by the filler material. DSC analysis has already shown that the morphology of PVOH is altered in the composite and the failure of the Krenchel

expression confirms this. A model which takes account of the crystallinity observed in the data above will now be introduced. This strongly suggests that nucleation of crystallinity by the nanotubes is responsible for at least some of the reinforcement observed.

Coleman and Ferreira[15] have derived a simple equation to describe the modulus of a polymer/nanotube composite in the presence of nanotube-nucleated crystallinity. This equation is derived by using the rule of mixtures to determine the modulus of a crystalline polymer coated nanotube as a weighted sum of the nanotube and crystalline polymer moduli which are denoted Y_{nt} and Y_{χ}, respectively. The nanotube is of radius r_{nt} with a polymer coating of thickness b. The modulus of a coated nanotube is then substituted into the rule of mixtures resulting in:

$$Y_c = v_f \eta_l \eta_0 \; Y_{nt} + (1 - v_f) Y_p + \left(\frac{b^2 + 2 r_{nt} b}{r_{nt}^{\;2}} \right) v_f \left(Y_{\chi} - Y_p \right) \qquad \textit{Equation 6-4}$$

Differentiating with respect to v_f gives

$$\frac{dY_c}{dv_f} = \eta_l \eta_0 \; Y_{nt} - Y_p + \left(\frac{b^2 + 2 r_{nt} b}{r_{nt}^{\;2}} \right) \left(Y_{\chi} - Y_p \right) \qquad \textit{Equation 6-5}$$

Using Equation 6-1 we can substitute for $(b^2+2r_{nt}b)/ r_{nt}^{\;2}$ to give

$$\frac{dY_c}{dv_f} = \left(\eta_l \eta_0 \; Y_{nt} - Y_p \right) + \frac{d\chi}{dv_f} \left(Y_{\chi} - Y_p \right) \qquad \textit{Equation 6-6}$$

predicting that dY_c/dv_f is proportional to $d\chi/dv_f$. This is exactly what we have seen in Figure 6-11(a). Equation 6-6 is of the form $y=c+mx$ where only the Y_{χ} and $\eta_l \eta_0 Y_{nt}$ are unknown and therefore the slope of Figure 6-11(a) can be used to calculate a modulus of 30 ± 3.5 GPa for the crystalline coating Y_{χ}. The intercept can be used in conjunction with a η_0 value of 0.38 to calculate the product $\eta_l Y_{nt}$ = 710 ± 606 GPa. While there is a large error associated with this value, arising from the scatter in the raw data and difficulty in accurately measuring nanotube diameters, the value does fall within the range of moduli expected for carbon nanotubes[14]. The fact this model calculates a more realistic value for the nanotube modulus compared to the Krenchel expression, success of this model,

highlights the role of nanotube-induced crystallinity in the reinforcement of the polymer/nanotube composite.

6.8 Tensile strength data

Ultimate tensile strength, σ_T, and toughness, T, values are plotted as a function of volume fraction in Figure 6-14(a) and (b), respectively. The erratic nature of the toughness data makes analysis impossible although a peak in toughness is observed at relatively low volume fractions for all nanotube types. Fluctuation in toughness data is typical of PVOH composites due to their extreme sensitivity to atmospheric moisture[1]. A small quantity of absorbed water produces a small increase in strain which produces a dramatic increase in area under the curve from which the toughness is calculated.

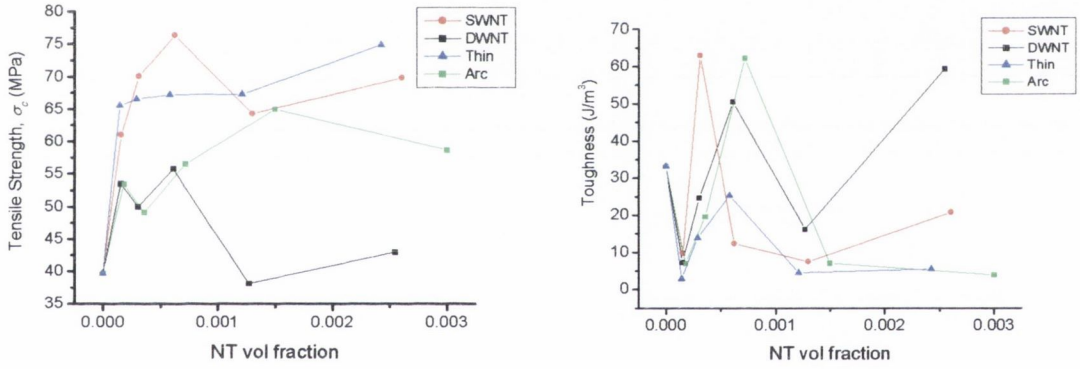

Figure 6-14(a): *Tensile strength,* σ_T, *and* ***(b)*** *toughness,* T, *values plotted as a function of nanotube volume fraction.*

For a homogenous matrix, that is one without crystalline domains, the tensile strength of a composite, σ_c, can be derived under the assumption that the composite has two fracture components. One in the bulk polymer and the other at the polymer/nanotube interface. The assumption of a fracture component at the polymer/nanotube interface implies that that no stress transfer occurs from the matrix to the nanotube. This assumption is only true for short fibres: When the matrix is under stress, the stress transferred to the fibre is described by the interfacial stress transfer, τ. The stress transferred scales with fibre length, l, so that at some critical length, l_c, the stress transferred is large enough to break the fibre. For a hollow cylinder, this critical length is given by

$$l_c = \frac{\sigma_f d}{2\tau}\left[1 - \frac{d_i^2}{d^2}\right] \qquad \textit{Equation 6-7}$$

where σ_f is the fibre strength, d and d_i are the fibre external and internal diameters respectively[16]. In effect, the stress transferred to the fibre builds up to its maximum value (σ_f, that which causes breakage) over a distance l_c from the end of the fibre. This means that short fibres carry load less efficiently than long fibres meaning that they can be thought of as having a lower effective modulus for reinforcement purposes. The tensile strength for such a composite, σ_c, can be expressed as[11]:

$$\sigma_c = \left(\frac{l_{nt}\tau}{2r_{nt}} - \sigma_p\right)v_f + \sigma_p \qquad \textit{Equation 6-8}$$

where l_{nt} is the nanotube length, r_{nt} is the nanotube radius, v_f is the nanotube volume fraction and σ_p is the ultimate tensile strength of the neat polymer film (39.7 MPa). The interfacial stress transfer, τ, can therefore be calculated from a plot of σ_T against v_f. Before applying this model an alternative model will be introduced after which the two models will be applied to decide which describes the PVOH/Nanotube composites.

The second model was developed from the homogenous system by Coleman et al[1] and describes a heterogenous matrix system where a crystalline polymer coating exists in addition to the bulk polymer:

$$\sigma_c = \left(1 + \frac{b}{r_{nt}}\right)\left[\frac{l_{nt}}{2r_{nt}}\sigma_{shear} - \left(1 + \frac{b}{r_{nt}}\right)\sigma_p\right]v_f + \sigma_p \qquad \textit{Equation 6-9}$$

where σ_{shear} is the polymer shear modulus.

If a crystalline layer exists at the nanotube surface then Equation 6-8 will give acceptable values for the shear modulus of the crystalline polymer. If no crystalline layer exists then Equation 6-9 will apply and yield realistic values for the interfacial stress transfer to the nanotube. Table 6-1 summarizes the results.

Table 6-1: *Tensile analysis results.*

Nanotube	Avg. radius r_{nt} (nm)	Coating b (nm)	$d\sigma_c/dv_f$ (GPa)	τ (MPa) Homogenous matrix	σ_{shear} (MPa) Crystalline coating
SWNT	0.75±1	12±6.5	97.0	146±193	10±30
DWNT	1.5±2	17.0±0.5	34	101±136	10±31
ThinMWNT	4.6±1.5	48±5	178	1630±413	145±67
Arc	9±4	47±13	26	472±261	80±93

In all cases l_{nt} , the nanotube length, was set at 1 μm. This decision was based on the sonication/TEM study of Chapter 5 where CVD nanotubes typically are imaged to fracture to lengths of approximately 1 μm. The Arc_MWNT produced in house are short with typical lengths of 1 μm. Note that a factor of two increase in nanotube length would correspond to a 50% drop for both τ and σ_{shear} for all nanotube types. It is the error in the length, that results in the large σ_{shear} value for the ThinMWNT nanotubes which are particularly difficult to measure due to the entanglement shown in Figure 6-12.

The values for stress transfer, calculated using the homogenous model, are unrealistically high and have unavoidably large errors due to the uncertainty associated with measurement of nanotube radii. The calculated values are significantly larger than the predicted values of 10 MPa[17] for non-covalently bonded polymer/nanotube interfaces. However, the heterogenous model produces shear strength values that are of the correct order of magnitude although these values have the same problem of large experimental error. Therefore, while the heterogenous model is consistent with the data, the associated errors imply the result must be viewed with caution. The crystallinity data supports the decision to fit this model as the polymer volume associated with the heterogenous crystalline regions would account for the increase in crystallinity observed by DSC.

Furthermore, Cadek et al[18] have imaged the crystalline coating at the PVOH-nanotube interface. In that case, TEM was used to observe a MWNT that had fractured out of a PVOH matrix due to film shrinkage. The nanotube emerged with its polymer coating intact indicating that fracture occurred at the amorphous/crystalline polymer interface

rather than at the nanotube surface. This proved that the crystalline PVOH coating had adhered well to the nanotube and is significantly stronger than the amorphous polymer domains that are present in the "bulk" polymer.

This agreement between the crystalline coating model and experimental data for tensile strength is yet more evidence that the nanotubes are nucleating polymer crystallinity in the composites and this crystalline polymer exists as a coating at the polymer/nanotube interface. DSC crystallisation data will now be discussed to assess the ability of the various nanotube types to nucleate crystallinity from a polymer/nanotube melt as opposed to a composite solution.

6.9 Nanotube induced "solid-state" crystallisation

In addition to the analysis presented above for the crystallinity induced during film drying, and subsequent enhancement of strength, valuable information regarding the crystal nucleation behaviour of the various carbon nanotube types can be extracted from the DSC curves obtained by controlled cooling. It is clear from the variation in the crystallisation curves shown in Figure 6-15 that each nanotube induces unique polymer crystallisation behaviour.

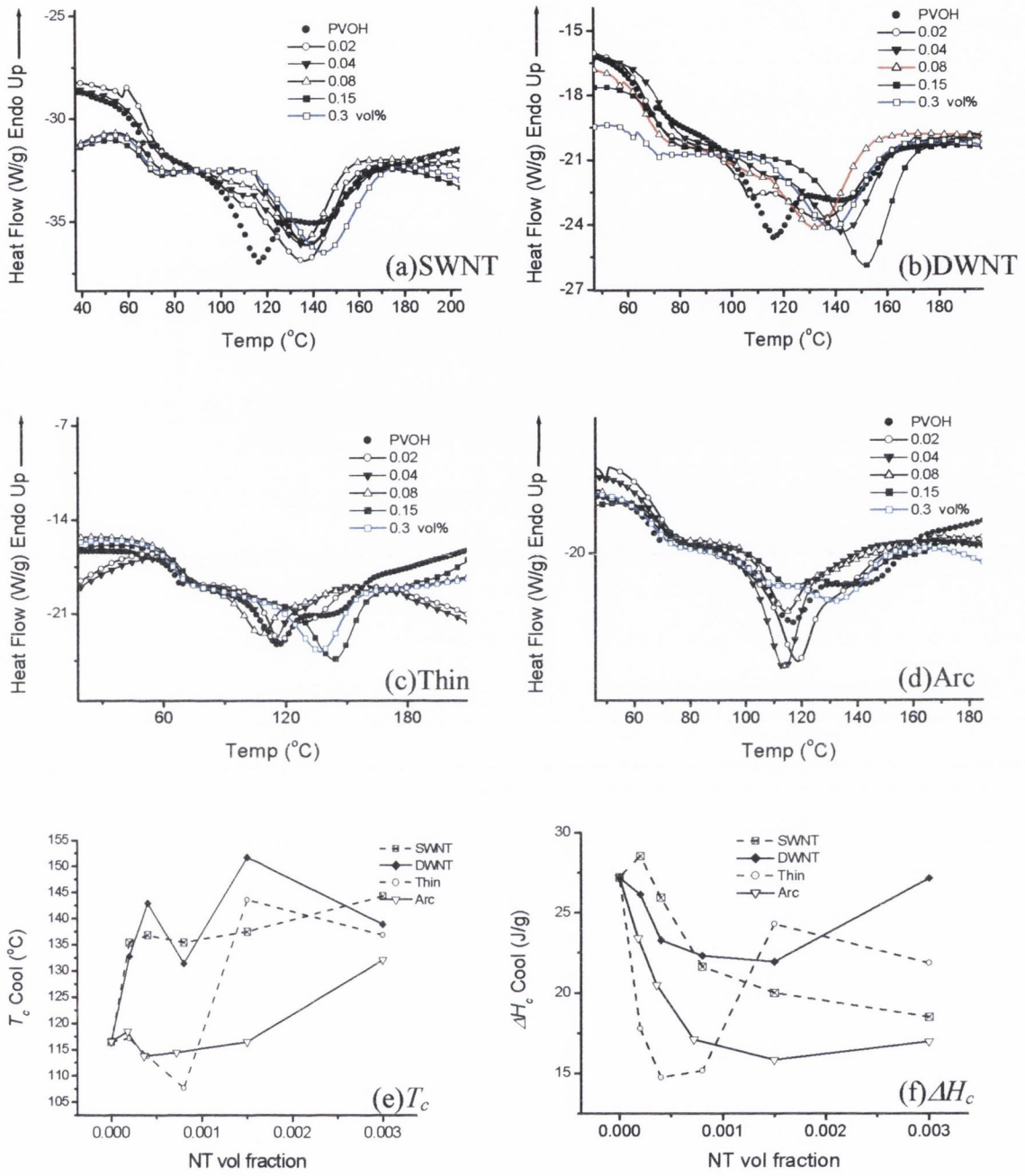

Figure 6-15(a): *Crystallisation data for SWNT* ***(b)*** *DWNT* ***(c)*** *ThinMWNT* ***(d)*** *Arc composites* ***(e)*** *Crystallisation peak temperatures,* T_c, *and* ***(f)*** *Enthalpy of crystallisation,* ΔH_c, *as a function of nanotube volume fraction for all nanotube types.*

Given the complicated crystallisation curve associated with the neat PVOH film it is not possible to use a fwhm approach – it is more useful to display the explicit data where the distinct differences for each composite can be easily observed. The three transitions for the neat PVOH film are (i) onset of crystallisation at 166 °C (ii) crystallisation peak, T_c, at 116.5 °C with crystallisation terminating at 92.5 °C (iii) glass transition at approximately

60 °C. Given the cooling rate of 40 °C/min this implies crystallisation is completed in approximately 110 seconds. It is useful for analysis to consider the initial crystallisation onset as phase 1 and the well-defined peak as phase 2. Upon introduction of the SWNT nanotubes, phase 1 becomes dominant, as shown in Figure 6-15(a). T_c is plotted as a function of nanotube volume fraction in Figure 6-15(e), verifying that the neat polymer crystallisation peak increases by 19 °C upon introduction of nanotubes. This increase in T_c arises because the nanotubes are inducing a more ordered crystalline form of PVOH. However, further addition of nanotubes only produces an additional increase of 8.8 °C at the highest loading. The blue curve in each data set of Figure 6-15 represents the highest loading fraction. Nanotube induced increases in T_c of 18.3 °C have been reported by Valentini et al in polypropylene reinforced with 20 wt% of SWNT[19].

The variation in T_c within the set of composites for each nanotube type can be used to specify the deviation in crystallisation temperature in the nanotube concentration range. This in turn reflects the improvement in crystallinity relative to the polymer film. A large variation in T_c for a given nanotube type implies that each volume fraction of that nanotube type has a different crystallisation temperature and therefore has a distinctly different crystal size. A small variation in T_c reflects a well-defined crystal structure that is present in each volume fraction. T_c for the SWNT samples was determined to be 137.9 ± 3.7 °C while Figure 6-15(b) and (e) shows that T_c for the DWNT samples is 139.5 ± 8.2 °C. Comparing these values, it can be concluded that nanocyl DWNT nucleate more highly ordered crystals (increase in average T_c) while the SWNT samples have a similar crystallite conformation (low variation in T_c).

For the larger diameter ThinMWNT and Arc composites the crystallisation curves are extremely interesting. In both cases phase 2, the lower temperature component of crystallisation, dominates the low loading fractions. In other words these composite peaks overlap the pure polymer peaks. This suggests that samples such as the 0.04 vol% Arc film contain crystallites that are identical in conformation to those of the pure polymer. The average T_c and deviation of the ThinMWNT composites is 119.1 ± 7.5 °C and 123.8 ± 15.3 °C for the arc samples. Therefore, it can be concluded that large diameter nanotubes are less effective at nucleating highly ordered PVOH crystals than the smaller

diameter SWNT and DWNT nanotubes. The excellent performance of DWNT agrees well with the previous reports of Cadek et al[20].

A paper by Sandler et al[21], in collaboration with a number of universities including our group at Trinity, measured polyamide fibres doped with a range of carbon nanotubes and nanofibres. The crystallisation peak temperature (T_c) for a composite fibre comprised of arc grown carbon nanotubes (AGNT) and a polyamide-12 (PA-12) matrix was found to increase up to a loading of approximately 2 wt%, as reproduced in Figure 6-16.

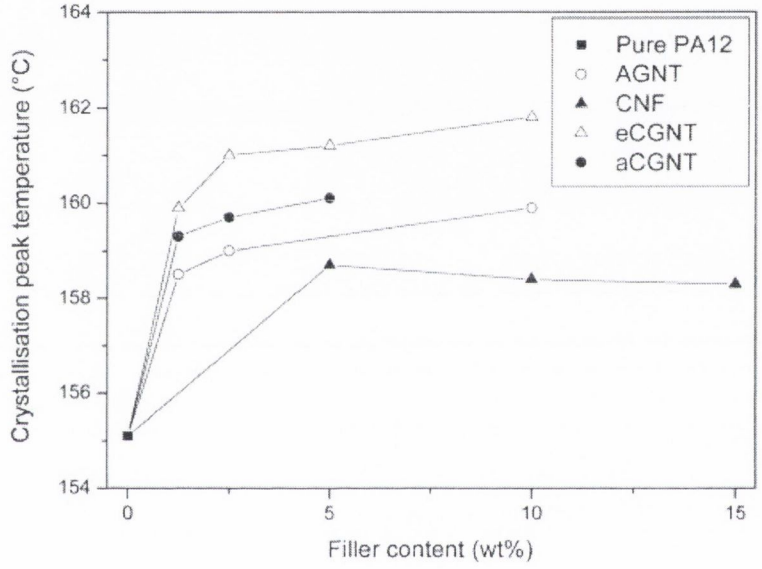

Figure 6-16: *Plot of crystallisation peak as a function of filler content. Data reproduced from Sandler et al[40].*

Above 2 wt% T_c began to plateau. Similarly, the crystallisation peak temperature (T_c) for a carbon fibre (CNF)/polyamide-12 (PA-12) composite fibre was found to increase dramatically up to a loading of approximately 5 wt% of nanotubes. Above 5 wt% T_c began to marginally decrease. The paper concluded that the plateau effect is influenced in part by nanotube enhancement of the matrix thermal conductivity in addition to another unidentified mechanism. While there is undoubtedly a thermal conductivity component to the increase in T_c, in light of the dispersion studies undertaken in this thesis coupled with the crystallinity and mechanical data it is suggested here that at low volume fractions the fillers were better dispersed thus exposing greater nanofibre surface area for crystallisation resulting in rapid increase for T_c. As the filler content is increased, isolation of individual nanofibres or nanotubes becomes more difficult and there is less filler

separation. This reduces the exposed surface area for crystal nucleation and also will affect the morphology of crystal growth as overlap of crystalline domains associated with filler elements is inevitable due to their close proximity. Images of composite fibre with filler concentrations of 5 wt%, included in the paper by Sandler et al[21], show inter-filler interaction despite the fact the filler material is excellently dispersed. Therefore, T_c begins to stabilise and may, as in the case of the carbon nanofibre data of Figure 6-16, decrease.

In addition to the large diameter CNF [155 nm] and arc-grown nanotubes (AGNT) [15 nm], aligned catalytically-grown nanotubes (aCGNT) [43 nm] and entangled catalytically-grown nanotubes (eCGNT) [10 nm] were studied as PA-12 dopants. As can be seen in Figure 6-16, the highest T_c was observed for the smallest diameter catalytically grown nanotubes. This is in excellent agreement with the PVOH composites studied in this thesis where the smallest diameter nanotubes again produced the largest T_c values.

6.10 DSC data for second heat run of PVOH/nanotube composites.

The DSC data from the second heat run can be analysed to assess the crystals formed during the controlled cooling of the PVOH/composite so that a comparison of solution phase and "solid-state" phase crystallisation can be made using the data from the first and second heat runs, respectively. The data is presented in Figure 6-17.

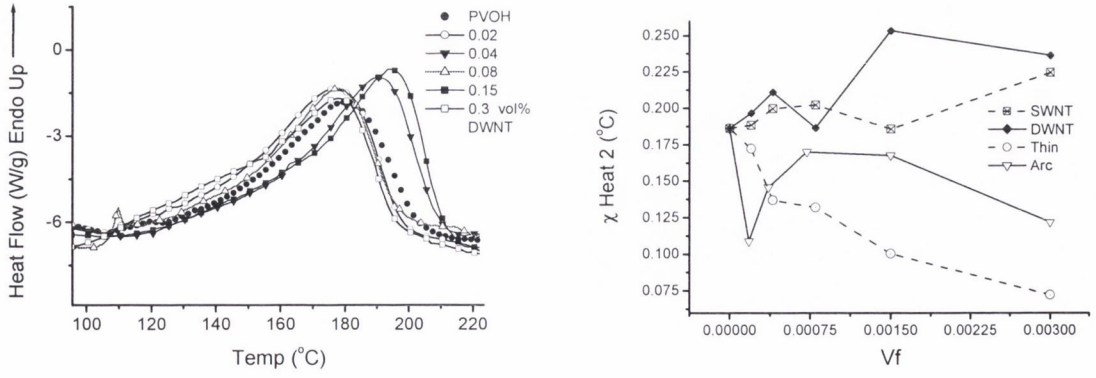

Figure 6-17(a): *Second heat run DSC curves for DWNT composites* ***(b)*** *Crystalline fraction, χ, as a function of nanotube volume fraction, v_f, and* ***(c)*** *Melting temperature determined from second heat run, T_{m2} data for all nanotube types.*

The crystals melted during the second heat run have been formed during the controlled cooling stage of the heat-cool-heat DSC cycle. The crystalline fraction values as a function of nanotube volume fraction are plotted in Figure 6-17(b) and verify that the small diameter nanotubes yield the highest crystalline fractions.

Comparing the first heat run data, discussed in Section 6-5 above, with the second heat run data reveals a decrease in melt temperature is observed for all samples implying smaller crystallite structures are melted in the second heat run. This T_{m2} data is shown in Figure 6-17(c). The smaller crystallite size is expected given the slow rate of crystallisation during the solution casting process relative to the fast "solid-state" crystallisation at 40 °C/min in the DSC chamber[3].

6.11 DMTA of Nanocyl DWNT

DMTA measurements were used to confirm the mechanical properties of the DWNT composites. Figure 6-18 shows the storage modulus (E') and *Tan* δ data obtained for the DWNT composites. There is an increase in E' with increasing nanotube content up to a peak at 0.15 vol% DWNT before a fall in modulus for the 0.3 vol% DWNT sample. The peak in modulus at 0.15 vol% agrees reasonably well with that observed at 0.08 vol% using the tensile tester. The most useful aspect of the DMTA data is the identification of a decrease in T_g with increasing nanotube fraction as demonstrated by the decrease in the *Tan* δ peak temperature. This was measured much more accurately using DMTA than could be achieved using DSC.

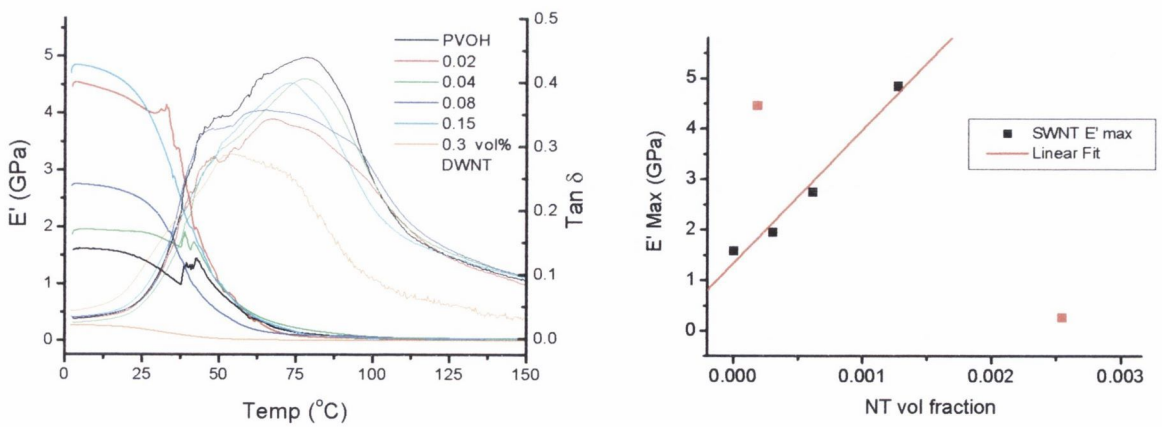

Figure 6-18: *DMTA data for DWNT samples.*

A plot of the maximum storage moduli as a function of nanotube volume fraction is shown in Figure 6-18(b). As with all of the preceeding analysis a linear fit is fitted to the lower nanotube fractions and dE'/dv_f is substituted into Equation 6-3 for analysis by the Krenchel expression. The lowest DWNT/PVOH volume fraction is omitted from the fit – some deviation in the experimental parameters or sample configuration may be responsible for the error which results in the anomalous data point. The highest nanotube volume fraction is also omitted as at this concentration the reinforcement breaks down. This trend has already been observed in the tensile and crystallinity data analysed in Sections 6-5 and 6-6, respectively. Applying the Krenchel expression yields an effective nanotube modulus of 7 ± 1 TPa. As discussed earlier, these values are too high for CVD nanotubes and show that the Krenchel expression does not apply to our system where nanotubes alter the polymer morphology.

6.12 XRD of N_DWNT

The wide angle X-Ray scattering (WAXS) of the pristine polymer and the 0.08 vol% DWNT composite thin films in the 2θ range of 2° to 10° are plotted in Figure 6-19.

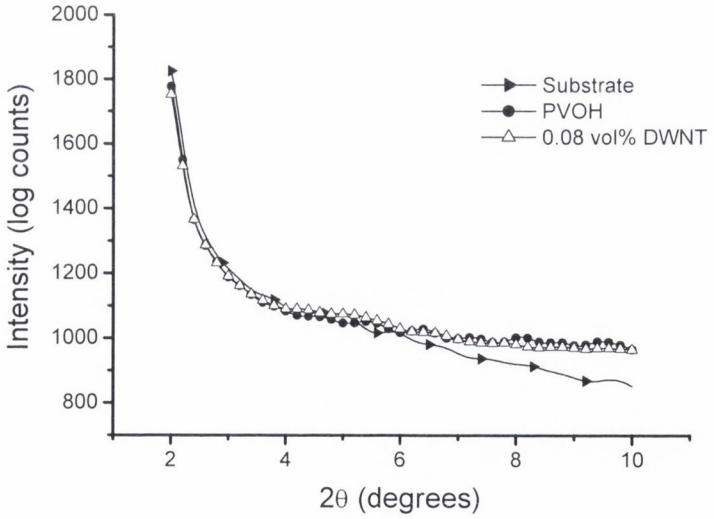

Figure 6-19: *2° to 10° WAXS of substrate, PVOH and 0.08 vol% DWNT composite.*

No sharp peaks are observed but deviation from the substrate curve shows the amorphous scatter by the polymer above 6°. There is no discernable difference between the polymer

only and the composite films. The PVOH WAXS data from 10° to 30° are plotted in Figure 6-20 and exhibit polymer peaks at 19.52° and 21.92°. These agree well with the two most intense peaks of four observed by Strawhecker et al 16.0°, 19.4°, 20.1°, and 22.7° and which he assigned to 100, 101, 101, and 200 crystalline reflections respectively[22].

As discussed in Chapter 4, the penetration depth of the X-Rays is several millimeters even a small angles. This implies that the 60 μm thin film specimens and the substrate are fully probed by the X-Ray beam. Therefore it should be irrelevant which side of the film is in contact with the substrate as all layers of the film will be measured in either case and we expect an almost identical scattering curve. In order to investigate this both sides of the composite film were scanned. Figure 6-19 shows that the two curves are very similar although the intensity of one curve is marginally less than the other. This can be explained by the fact that when the film was turned over the location on the substrate would have changed slightly resulting in a marginally different substrate contribution which adds to the scattering of the sample itself.

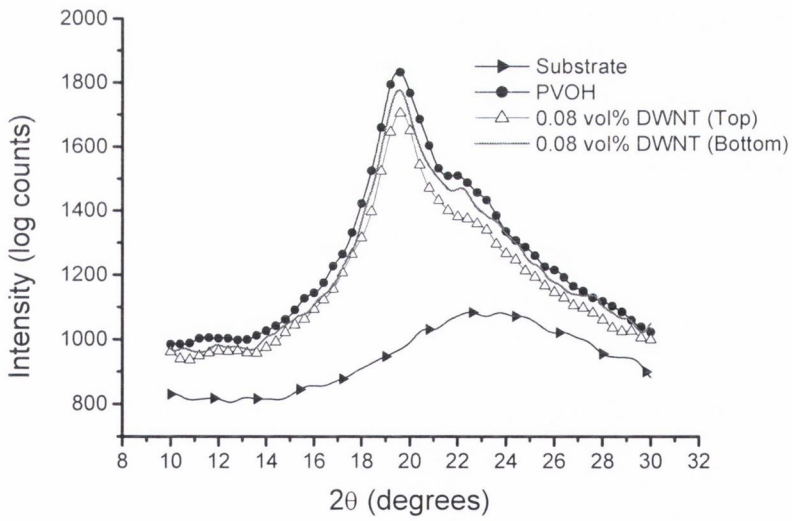

Figure 6-20: *10° to 30° WAXS of substrate, PVOH, 0.08 vol% top and bottom.*

As with the PmPV experiments of Chapter 4, no new peaks appear with the addition of nanotubes to PVOH. DSC measurements presented above have identified an 11% increase in crystallinity for the same 0.08 vol% DWNT sample probed using WAXS. In addition, the much improved mechanical properties of that composite relative to pure

PVOH leaves no doubt that a different morphology is present in the composite. Therefore the failure of WAXS to identify a new phase may be attributable to the film thickness concerns raised in Section 4.4 of Chapter 4.

6.13 Mechanism of reinforcement

The proportionality between the crystallinity and mechanical performance prompted further literature research to assess if crystallinity alone could be the reinforcing mechanism of the PVOH/Carbon nanotube composites. When the high moduli of carbon nanotubes are considered, in particular the well-graphitized ArcMWNT[23,24], one would expect much higher increases in Y than the maximum 5-fold increase observed in Chapter 5. The only explanation for the low increases observed in composites that use non-covalent bonding is a lack of stress transfer to the nanotube. It is suggested here that nanotubes are acting as a crystallisation surface thus increasing the crystallinity that results in low magnitude reinforcement. So then, the question emerges why not use other, more inexpensive fillers to nucleate crystallinity? The key advantage to nanotubes is their extremely high aspect ratio. This ensures a large surface area that extends longitudinally and is effective at promoting long-range crystalline domains at extremely low volume fractions. This is under the proviso that the tubes are well separated, the importance of which has been demonstrated in Chapter 5. Another filler often studied in composites is sodium montmorillonite nanoclay. A study of taken from the literature will now briefly compare the properties of a sodium montmorillonite/PVOH composite to those of a carbon nanotube/PVOH composite.

Sodium montmorillonite has been successfully used as a filler in a PVOH matrix by Strawhecker et al[22] achieving a 3-fold increase in Young's modulus at a loading of 4 wt%. Little change was observed in the maximum stress at break and toughness values for the composite. Further increase of the nanoclay content to 10 wt% only produces a further 10% increase in modulus suggesting a threshold for efficient reinforcement. Extensive DSC and XRD studies showed the introduction of the nanoclay significantly changes the polymer morphology. A new crystalline phase appears in the composite at the expense of the PVOH peak and scales linearly with nanoclay loading. Unlike our carbon nanotube/PVOH composite system where polymer crystallinity is increased, the overall PVOH crystallinity decreases in the nanoclay composites. In order to elucidate the

reinforcing mechanism it is worth considering two points. Firstly, nanoclays consist of platelets that separate into layers with a controllable spacing, *d*, when the appropriate chemistry is applied – this separation is termed exfoliation. XRD is used to measured the inter-layer spacing and deduce the degree of exfoliation. Secondly, it has been shown in Chapter 5 that a 3-fold increase in PVOH modulus can be produced by removal of water. Both these points suggest that the 4 wt% of nanoclay exfoliates within the matrix or induces a small volume of a new more well-defined crystalline phase: both of these scenarios would reduce the free volume for water molecules and reduce polymer chain movement arising in reinforcement. It is concluded that a similar mechanism may be at work in the PVOH/Carbon nanotube composites with crystallisation as the dominant process.

6.14 Nanotube functionalisation

6.14.1 OH functionalisation experiment

An experimental procedure was outlined in Chapter 3 with the aim of crosslinking the residual OH groups of the acid purified carbon nanotubes with the OH groups of the polymer matrix. Tensile testing was used to assess the mechanical properties of these films. One pristine polymer film was cast from the usual neutral polymer/deionised water solution and another from acidic polymer/deionised solution made by the addition *p*-toluenesulfonic acid. These films provide the reference values for the Young's modulus and tensile strength of PVOH with and without acid. Annealed Thin MWNT (free of OH groups) were then added to PVOH solutions with and without acid. Thin MWNT without annealing (should contain OH groups) were also added to PVOH solutions with and without acid. If the crosslinking reaction worked, the mechanical performance of the un-annealed Thin MWNT should be greater than that of the annealed samples. Figure 6-21 shows that the presence of acid did not enhance or compromise the reinforcement that is typical of any CVD nanotube/PVOH composite. However, it is noted that the neat polymer film doped with acid exhibits over a two-fold increase in modulus and strength over the pristine PVOH film.

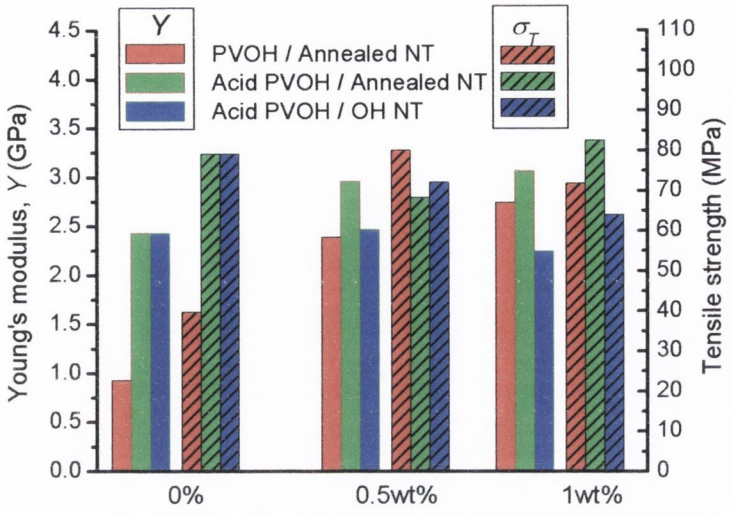

Figure 6-21: *Bar chart showing the tensile moduli and strengths for composite films cast from neutral and acidic solutions.*

The failure of this simple approach proves that the more complex reactions reported in the literature to enable nanotube/matrix bonding are very necessary. The following section will outline the progress in this area to date.

6.14.2 Literature

As we have seen, despite reasonable increases in strength observed in our polymer/nanotube composites the true strength of carbon nanotubes cannot be realized simply by mixing with a polymeric matrix. The crystallisation interaction we have identified as the reinforcing mechanism in the PVOH composites does not provide sufficient stress transfer to make use of the mechanical properties inherent to the nanotube. To achieve a factor of ten increase and beyond, an alternative approach involving nanotube functionalisation will be required and in the last four years significant progress has been made on this front. In 2001, Czerw et al[25] successfully grafted propionylethylenimine-*co*-ethylenimine (PPEI-EI) to SWNT. This was achieved via an amidation reaction between the PPEI-EI of the polymer and acyl chlorides on the nanotubes. The acyl chlorides were derived from the carboxylic acids inherent to carbon nanotubes after acid purification. Scanning tunnelling microscopy (STM) was used to investigate the PPEI-EI/carbon nanotube composites and found that the nanotube acted

like a template for the polymer chains which crystallised onto the nanotube surface. This is yet another example of nanotube induced polymer crystallisation with the added benefit that the polymer chains are guaranteed to exist at the nanotube surface since one end of the chain is anchored by virtue of the functionalisation reaction.

In 2002, Shaffer et al[26] successfully grafted polystyrene (PS) to MWNT. Given that carbon nanotubes have been reported to reinforce PS[27,28], the use of PS grafted tubes may result in a matrix/functionalised nanotube interface that improves upon the more simple matrix/nanotube interface. In 2003, Eitan et al[29] reported the chemical modification of multiwalled carbon nanotubes (MWNT) by means of epoxide-based functional groups. FTIR spectroscopy and TGA were used for characterisation but no mechanical data was included as part of that epoxy study.

More recent experiments by Blake et al[30,1] have focused on producing a system where long polymer chains orthogonally extend into the matrix from their anchor point on the nanotube surface. Butyllithium-functionalised MWNT were further reacted with chlorinated polypropylene (CPP) to produce a covalent bond. The CPP functionalised nanotubes were then embedded in a CPP matrix and subjected to tensile testing. A 3-fold increase in Young's modulus was accompanied by a 4-fold increase in both ultimate tensile strength and toughness.

Many of the results of this thesis are directly relevant to nanotube functionalisation reactions. Firstly, it has been shown that nanotubes must be effectively isolated within a polymer matrix for maximum reinforcement. This information transfers to chemical reactions where best results are expected when the entire nanotube surface area is exposed to functionalisation. Furthermore, inter-nanotube reactions are undesirable since the nanotubes need to be completely separated after they have been harvested from the functionalisation reaction for embedding in a suitable matrix. In this way, the entire surface area of the functionalised nanotube will be exposed to a surrounding volume of polymer. If nanotubes have been accidentally functionalised together to form aggregates then reinforcement will be compromised.

6.15 Conclusions

In Chapter 5, preliminary experiments suggested that a threshold existed for nanotube loading above which reinforcement of PVOH/Carbon nanotube composites ceased. To confirm this, composites were fabricated using carbon nanotubes with a range of diameters dispersed in a PVOH matrix. Chapter 6 correlates crystallinity studies with tensile measurement of the composites verifying that both crystallinity and Young's modulus were enhanced at volume fractions below 0.1 vol% but tended to decrease with additional nanotube loading. Furthermore, a relationship between crystallinity and the magnitude of reinforcement was identified for all composites.

Drop cast films of PVOH and composites with up to 0.3 vol% of carbon nanotubes were subjected to DSC crystallinity measurements. The highest increase in crystallinity was observed for volume fractions below 0.1 vol%. The 0.07 vol% DWNT composite was found to exhibit the highest increase of all composites tested and was 61% more crystalline than the reference PVOH film. Furthermore, within each of the four sets of nanotube concentrations that were produced using four different nanotube diameters, one concentration had the highest crystallinity. In each of the four cases this sample with the highest crystallinity either possessed, or had values extremely close to, the most impressive increase in Young's modulus and tensile strength. Thus for a given nanotube diameter there is no doubt that crystallinity governs the reinforcement. The situation became a little more complicated when the sets of data were compared for the two best performing nanotube diameters: the DWNT and SWNT. It may be recalled from above that the DWNT composite was found to exhibit the highest crystallinity increase of all composites tested. The Young's modulus of this composite was 154% greater than that of a pure polymer film while the tensile strength was 40% greater. If crystallinity were the only factor determining the reinforcement, then the mechanical properties of this DWNT composite should best all the other samples. In fact the 0.07 vol% SWNT composite was found to exhibit the most impressive mechanical properties of all the composites tested with a Young's modulus 206% greater than that of a pure polymer film while the tensile strength was 92% greater. This implies that the smaller nanotube diameter interacts more effectively with the crystalline polymer so even though a smaller fraction of crystalline polymer has been nucleated in the matrix, the polymer/nanotube interaction is such that the composite mechanically outperforms a DWNT composite where the DWNT have induced a higher crystallinity.

The Krenchel's form of the simple rule of mixtures, which is applicable to composite systems where the polymer matrix morphology is unchanged by the filler, was fitted to the Young's modulus data. The Krenchel analysis yielded very high values for the Young's modulus of each nanotube and therefore does not describe our composite system. This is further evidence that polymer morphology is altered by the nanotubes present in the nanotube/PVOH composite. A new model, which assumes a crystalline coating around each nanotube was applied to the system and produced a more realistic effective nanotube modulus of 710 ± 606 GPa. The large error on this value is noted but is unavoidable due to the difficulty associated with measuring nanotube diameters.

The crystallisation data was analysed for all composites. It was observed that polymer crystallisation varied significantly as a function of nanotube diameter. The DWNT samples exhibited the most impressive increase in crystallinity with an increase in of 35 °C in T_c relative to a neat polymer film.

This prompted a review of some recent papers to determine if crystallisation could be the reinforcing mechanism rather than stress transfer to the nanotube. The results of many publications reporting on the crystallisation behaviour and/or mechanical data for carbon nanotubes/polymeric matrices could be explained in terms of a nanotube loading threshold. A decrease in polymer crystallinity, or rapid drop in the rate of increase as a function of nanotube concentration, can be observed if the number of nanotubes exceeds this threshold.

6.16 References

[1] J.N. Coleman, M. Cadek, R. Blake, V. Nicolosi, K.P. Ryan, C. Belton, A. Fonseca, J.B. Nagy, Y. Gun'ko, W.J. Blau; "High performance nanotube reinforced plastics: The mechanism of strength increase", *Adv. Funct. Mat.* **14**, 791 (2004)

[2] K.E. Strawhecker, E. Manias; "AFM of poly(vinyl alcohol) crystals next to an inorganic surface", *Macromolecules* **34**, 8475 (2001)

[3] O. Probst, E.M. Moore, D.E. Resasco, B.P. Grady; "Nucleation of polyvinyl alcohol crystallization by single-walled carbon nanotubes", *Polymer* **45**, 4437 (2004)

[4] R. Endo, S. Amiya, M.J. Hikosaka; "Conditions for Melt Crystallization Without Thermal Degradation and Equilibrium Melting Temperature of Atactic Poly(Vinyl Alcohol)", *Macromol. Sci. Part B-Phys* **B42**, 793 (2003)

[5] J.W. Gillman, D.L. VanderHart, T. Kashiwagi; "Thermal decomposition chemistry of poly(vinyl alcohol)", *Fire and Polymers II: Materials and test for hazard prevention* **ACS 599**, 161 (1994)

[6] A.R. Bhattacharyya, T.V. Sreekumar, T. Liu, S. Kumar, L.M. Ericson, R.H. Hauge, R.E. Smalley; *Polymer* **44**, 2373 (2003)

[7] D.W. Clegg, A.A. Collyer; "Mechanical properties of reinforced thermoplastics", *Elsevier Applied Science*, Essex (1986)

[8] B.P. Grady, F. Pompeo, R.L. Shambaugh, D.E. Resasco; "Nucleation of Polypropylene Crystallization by Single-Walled Carbon Nanotubes", *J. Phys. Chem. B* **106**, 5852 (2002)

[9] H.L. Cox; "The elasticity and strength of paper and other fibrous materials", *Brit. J. Appl. Phys.* **3,** 72 (1952)

[10] M. O'Regan, D.F. Akay, B. Meenan; "A comparison of Young's modulus predictions in fibre-reinforced-polyamide injection mouldings", *Compos. Sci. Technol.* **59,** 419 (1999)

[11] W.D. Callister; "Materials Science and Engineering: An introduction", *John Wiley and Sons*, 6th ed., New York (2003)

[12] H. Krenchel; "Fibre Reinforcement", Akademisk Forlag, Copenhagen (1964)

[13] M.S.P. Shaffer, A.H. Windle; "Fabrication and characterization of carbon nanotube/poly(vinyl alcohol) composites.", *Adv. Mat.* **11**, 937 (1999)

[14] J.P. Salvetat, A.J. Kulik, J.M. Bonard, G. Andrew, D. Briggs, T. Stockli, K. Metenier, S. Bonnamy, F. Beguin, N.A. Burnham, L. Forró; "Elastic Modulus of Ordered and Disordered Multiwalled Carbon Nanotubes", *Adv. Mat.* **11**, 161 (1999)

[15] J.N. Coleman, M. Ferreira; Unpublished

[16] A. Kelly, W.R. Tyson; *J. Mech. Phys. Solids* **13**, 329 (1965)

[17] A.H. Barber, S.R. Cohen, H.D. Wagner; "Measurement of carbon nanotube-polymer interfacial strength", *Appl. Phys. Lett.* **82**, 4140 (2003)

[18] M. Cadek, J.N. Coleman, V. Barron, K. Hedicke, W.J. Blau; "Morphological and mechanical properties of carbon-nanotube-reinforced semicrystalline and amorphous polymer composites", *Appl. Phys. Lett.* **81**, 5123 (2002)

[19] L. Valentini, J. Biagiotti, J.M. Kenny, S. Santucci; "Morphological characterization of single-walled carbon nanotubes-PP composites", *Composites Science and Technology* **63**,1149 (2003)

[20] M. Cadek, J.N. Coleman, K.P. Ryan, V. Nicolosi, G. Bister, A. Fonseca, J.B. Nagy, K. Szostak, F. Béguin, W.J. Blau; "Reinforcement of polymers with carbon nanotubes: The role of nanotube surface area", *Nanolett.* **2**, 353 (2004)

[21] J.K.W. Sandler, S. Pegela, M. Cadek, F. Gojny, M. van Es, J. Lohmar, W.J. Blau, K. Schulte, A.H. Windle, M.S.P. Shaffer; "A comparative study of melt spun polyamide-12 fibres reinforced with carbon nanotubes and nanofibres" *Polymer* **45**, 2001 (2004)

[22] K.E. Strawhecker, E. Manias; "Structure and properties of poly(vinyl alcohol)/Na^+ montmorillonite nanocomposites", *Chem. Mater.* **12**, 2943 (2000)

[23] M.F. Yu, O. Lourie, M.J. Dyer, K. Moloni, T.F. Kelly, R.S. Ruoff; "Strength and breaking mechanism of multiwalled carbon nanotubes under tensile load", *Science* **287**, 637 (2000)

[24] J.P. Salvetat, A.J. Kulik, J.M. Bonard, G. Andrew, D. Briggs, T. Stockli, K. Metenier, S. Bonnamy, F. Beguin, N.A. Burnham, L. Forró; "Elastic modulus of ordered and disordered multiwalled carbon nanotubes", *Adv. Mat.* **11**, 161 (1999)

[25] R. Czerw, Z. Guo, P.M. Ajayan, Y-P. Sun, D.L. Carroll; "Organization of polymers onto carbon nanotubes: A route to nanoscale assembly", *Nanolett.* **1**, 423 (2001)

[26] M.S.P. Shaffer, K. Koziol; "Polystyrene grafted multi-walled carbon nanotubes", *Chem. Comm.* **18**, 2074 (2002)

[27] H.J. Barraza, F. Pompeo, E.A. O'Rear, D.E. Resasco; "SWNT-Filled thermoplastic and elastomeric composites prepared by miniemulsion polymerization", *Nanolett.* **2**, 797 (2002)

[28] D. Qian, E.C. Dickey, R. Andrews, T. Rantell; "Load transfer and deformation mechanisms in carbon nanotube-polystyrene composites", *Appl. Phys. Lett.* **76**, 2868 (2000)

[29] A. Eitan, K. Jiang, D. Dukes, R. Andrews, L.S. Schadler; "Surface modification of multiwalled carbon nanotubes: Toward the tailoring of the interface in polymer composites", *Chem. Mater.* **15**, 3198 (2003)

[30] R. Blake, Y.K. Gun'ko, J. Coleman, M. Cadek, A. Fonseca, J.B. Nagy, W.J. Blau; "A generic organometallic approach toward ultra-strong carbon nanotube polymer composites", *J. Am. Chem. Soc.* **126**, 10226 (2004)

CHAPTER SEVEN: CONCLUSIONS AND FUTURE WORK

7.1 PmPV

Two semi-crystalline polymers, poly(m-phenylenevinylene-co-2,5-dioctyloxy-p-phenylenevinylene) (PmPV) and poly(vinyl alcohol) (PVOH), have been independently doped with carbon nanotubes for the research project presented in this thesis. In the case of PmPV, well-graphitised arc discharge multi-walled nanotubes (ArcMWNT) were used as the filler material. Thermogravimetric analysis (TGA) was carried out in air to record the decomposition peaks of the polymer and nanotube structures. The ArcMWNT content was calculated from the nanotube decomposition peak. A reduction in the decomposition temperature of the phenyl group of the polymer backbone occurred upon addition of carbon nanotubes to the polymer matrix. This suggested a change in polymer backbone conformation such as that which would occur if the flexible sidechains were constrained or interacted with the sidechains of adjacent polymer strands. To assess the change in polymer morphology indicated by the TGA data crystallinity measurements were performed as follows.

Dynamic differential scanning calorimetry of thin composite films (~60 μm) detected a linear increase in polymer crystallinity up to 2.8 times that of the pure polymer at an ArcMWNT loading of 3 vol%. This provided direct evidence of a nanotube nucleated change in polymer morphology. A basic model of the system was proposed where a crystalline polymer layer coated each nanotube. The measured increase in film crystallinity can be attributed to the sum of the crystalline coatings allowing the thickness of the coating on each nanotube to be deduced. Fitting this model to the data gives a thickness of 25 ± 10 nm for the crystalline region adjacent to the nanotube. This value is in excellent agreement with previously published TEM images of polymer-coated nanotubes from where an average coating thickness of 25 nm was observed. Although the polymer diffraction peaks were recorded using X-Ray diffraction (XRD), the technique did not detect nanotube-induced changes in polymer morphology. Given the increase in crystallinity identified using DSC, it is suspected that the films used for XRD were too thin and therefore only a limited number of planes were present to contribute to the scattering signal thus reducing the sensitivity of the technique. The thin films also gave rise to substrate scattering and the broad scattering component of the glass may also be responsible for obscuring some of changes in polymer morphology in the XRD scans.

In addition, photoluminescence measurements found that the photoluminescence quantum yield in PmPV/ArcMWNT composites decreases with increasing nanotube content. This reduction in photoluminescence efficiency agrees with the calorimetry results since a decrease in polymer interchain separation is associated with an increase in crystallinity. This decrease in polymer interchain separation increases the number of non-radiative quenching sites increases and promotes the formation of non-emissive species. The model presented for the DSC data was further refined to describe the photoluminescence behaviour. It was assumed that the PL is at a maximum in the bulk polymer away from the nanotubes but begins to decreases linearly from the amorphous/crystalline boundary to zero at the polymer/nanotube interface, where crystallinity is expected to be maximised. The model fits the data extremely well, justifying the assumption of a linear decrease in PL as the distance from the nanotube decreases. The PL model yields a thickness value of 32 nm for the crystalline region. This is in reasonable agreement with the value of 25 ± 10 nm calculated by calorimetry and the coating observed using TEM. FTIR data provided additional evidence for nanotube-induced alteration of polymer conformation with an increase in the 669 cm^{-1} peak in the fingerprint region with the addition of carbon nanotubes. Mechanical measurements, conducted using a Zwick tensile tester and a DMTA, showed an increase of up to 30% in Young's modulus with the addition of 4.7 vol% of ArcMWNT. However, strength and toughness are compromised with a decrease of 35% and 70%, respectively.

All of the PmPV/ArcMWNT data strongly suggest that nanotube induced polymer crystallisation has occurred at the polymer/nanotube interface. It is probable that this crystallisation interaction is the mechanism that enables the suspension of MWNT, which is crucial to the non-destructive purification method. The interesting results of the PmPV/ArcMWNT composite encouraged further research on another semi-crystalline polymer, PVOH, that had previously been shown to coat carbon nanotubes[1]. The results obtained for the PVOH/Carbon nanotube composite material will now be summarised.

7.2 PVOH

Following the initial PmPV work, Poly (vinyl alcohol) was doped with nanotubes of various diameters. The nanotubes had been produced using both the arc and chemical vapour deposition techniques. PVOH was adopted over PmPV because it is inherently

more crystalline than PmPV. This superior crystallisation results in a larger enthalpy of melting so the crystalline fraction is measured with less error than that associated with PmPV. 120 W of sonic energy was applied for 15 min was found to break carbon nanotubes to an average length of 2 ± 1.5 μm. The degree of nanotube dispersion within the polymer matrix was monitored by an aggregation studied that employed both optical and electron microscopy. Increasing the sonication time to 60 min produced no further shortening of the nanotubes. This suggests that the CVD produced nanotubes fracture at defect sites during the initial 15 min sonication after which they are resistant to further shortening. It was also noted that re-aggregation of nanotubes may occur in solutions stored for extended periods of time. For this reason composites stored for more than five days before casting should be re-sonicated before film fabrication. To eliminate this complication the experiments presented in Chapter 6 were carefully planned so that film casting was carried out immediately after the settling/decantation procedure.

TEM images of copper grids that had been dipped in the composite showed that the Nanocyl Thick MWNT were isolated in the PVOH after the longest sonication time of 45 minutes was used. The Nanocyl DWNT, which are smaller in diameter relative to the Thick MWNT, were found to exist as a mixture of individual and bundled DWNT. Elicarb SWNT existed as bundles even after intensive sonication. SEM images showed that the 4 layer drop cast composite films contained features that increased in number as a function of nanotube content. The exact nature of these features could not be ascertained: either nanotubes had aggregated and become surrounded by polymer or polymer-coated nanotubes had grouped together.

Initial tensile measurements proved that carbon nanotubes mixed with PVOH, according to a specific procedure, exhibited a 3 to 5-fold increase in Young's modulus relative to a neat polymer film. The 3-fold increase was observed for films doped with 0.5 wt% Nanocyl DWNT (ND) while a 1 wt% Nanocyl Thick MWNT composite produced the 5-fold increase. It should be noted that a 5 wt% Nanocyl Thick MWNT composite showed no reinforcement so that a decision was made to focus on concentrations below 1 wt% in subsequent experiments. DSC measurements of the 0.5 wt% ND/PVOH composite showed a 1.5% increase in polymer crystallinity and the initial link between reinforcement and crystallinity was suggested. Furthermore, an upward shift of 13 °C in the crystallisation temperature, T_c, verified crystal nucleation by the nanotubes during

cooling from the melt. These results proved that the small increase in crystallinity, nucleated by the addition of carbon nanotubes, was sufficient to produce a significant increase in mechanical properties with the presence of nanotubes. TEM results provide conclusive evidence of a reinforcing web of nanotube bundles in the case of the DWNT and of well-dispersed individual nanotubes in the case of the Thick MWNT. The fact that the sample with the isolated nanotubes (Thick MWNT composite) exhibits the best reinforcement is logical in that isolated tubes should expose the greatest surface area for polymer crystallisation. To further develop the promising results observed in these preliminary experiments a comprehensive study was devised using identical concentrations of four different nanotube diameters and applying significant sonication to promote nanotube isolation. The results of that study will now be summarised.

Drop cast films of PVOH and composites with up to 0.3 vol% of carbon nanotubes were subjected to DSC crystallinity measurements. The maximum increase in crystallinity was observed for volume fractions below 0.1 vol%. The 0.07 vol% DWNT composite was found to exhibit the highest increase of all composites tested and was 61% more crystalline than the reference PVOH film. The maximum increase in crystallinity for each nanotube type was observed in the films with low nanotube concentration which were observed by SEM to contain well-dispersed small aggregates. The high volume fraction composites were found to be less crystalline and large aggregate structures were observed in the SEM images: these aggregates imply poor dispersion at high volume fractions and as a consequence the nanotubes are less effective at nucleating crystallinity. It is concluded that while the nanotubes can be well dispersed in a solution, as evidenced by the TEM studies of dipped copper grids, upon drop casting some re-aggregation may occur, especially at high volume fractions. Therefore, the moment when the solution is initially drop cast on the Teflon disc is the precursor stage to crystallisation, which takes place as the solvent is slowly evaporated. Thus, nanotube dispersion in solution is crucial as there will be a direct correlation between the degree of nanotube isolation during the precursor stage and the final crystallite size. Shortening of the tube into sections does not reduce the nanotube surface area exposed for crystallisation, and consequently does not reduce the mechanical performance. It is more favourable to have isolated short tubes than aggregated long tubes.

It is worth restating that many composite preparation techniques use melt-blending and extrusion to produce composites as opposed to the drop cast system that enables the slow drying of our composite films: it is this slow drying that promotes the crystallisation that has been detected by DSC which in turn is responsible for the observed reinforcement. Rather than discarding the first heating stage of DSC, the thermal history has been identical for all samples so that the first heating step represents the crystals formed during the slow drying process. The use of water as a solvent is useful for controlling the rate of crystallisation since it has a high boiling point relative to solvents such as toluene and chloroform. As in the case of the PmPV/ArcMWNT composites discussed in the first part of this thesis, crystallinity data was consistent with a crystalline coating at the PVOH/nanotube interface. Analysis of the crystallinity data showed that the thickness of the crystalline layer increases as a function of nanotube diameter.

Furthermore, within each of the four sets of nanotube concentrations that were produced using four different nanotube diameters, one concentration had the highest crystallinity. In each of the four cases this sample with the highest crystallinity either possessed, or had values extremely close to, the most impressive increase in Young's modulus and tensile strength. Thus for a given nanotube diameter there is no doubt that crystallinity governs the reinforcement. The situation becomes a little more complicated when the sets of data are compared for the two best performing nanotube diameters: the DWNT and SWNT. It may be recalled from above that the 0.07 vol% DWNT composite was found to exhibit the highest crystallinity increase of all composites tested. The Young's modulus of this composite was 154% greater than that of a pure polymer film while the tensile strength was 40% greater. If crystallinity were the only factor determining the reinforcement, then the mechanical properties of the DWNT composite should best all the other samples. In fact the 0.07 vol% SWNT composite was found to exhibit the most impressive mechanical properties of all the composites tested with a Young's modulus 206% greater than that of a pure polymer film while the tensile strength was 92% greater. This implies that the smaller nanotube diameter interacts more effectively with the crystalline polymer so even though a smaller fraction of crystalline polymer has been nucleated in the matrix, the polymer/nanotube interaction is such that the composite mechanically outperforms a DWNT composite where the DWNT have induced a higher crystallinity.

The final part of the project analysed the crystallisation data for all composites. For the ND/PVOH composites, a maximum increase in T_c of 35 °C relative to the 13 °C increase previously observed for the preliminary un-optimised samples. This suggests that the degree of polymer crystallinity can be controlled through the volume of nanotubes added coupled with the quality of their dispersion. The importance of nanotube diameter is further emphasized by the fact that the Elicarb SWNT samples, which were observed by SEM to have the best dispersion, exhibit the most impressive mechanical properties. This is interesting as it demonstrates that, in the case of single wall nanotubes, dispersing and reducing bundle size is sufficient to improve the crystallinity and the associated mechanical properties without actually separating the tubes from the bundles observed in the TEM images.

Analysis of the Young's modulus data using Krenchel's rule of mixtures found this model unsuitable for describing the composite system, thus proving that polymer morphology is altered in the composite. However, a new form of the rule of mixtures that assumes a crystalline coating exists around the nanotube was fitted to the data and yielded a more realistic effective nanotube modulus of 710 ± 606 GPa. This value is in good agreement with literature values and suggests that the increase in crystalline polymer, as measured by DSC, exists as a coating around each nanotube which reinforces the polymer matrix. The modulus of this crystalline coating was calculated to be significantly greater than that of amorphous polymer domains. The modulus of an amorphous polymer domain is unknown but what is known is that an 18% crystalline polymer reference film gives a Young's modulus of just under 1 GPa while the crystalline coating has a theoretically calculated modulus of 30 GPa. Analysis of the tensile strength data found that a model, which incorporates the crystalline polymeric coating at the nanotube surface, fits the data with reasonable values for the polymer shear modulus.

7.3 Implications for the plastics industry

It has been shown that at extremely low volume fractions (<0.1 vol%) of carbon nanotubes significantly raise the crystallisation temperature of PVOH. This reduces the time taken to crystallise a polymer from the melt and may therefore have applications in reducing the processing times for plastics. However, even though the loading fraction required is quite low, nanotubes would need to continue to reduce in price before the time

saved by the addition of nanotubes would justify the cost involved. The more realistic application will be the reinforcement of polymer matrices through excellent nanotube dispersion. For this to be adopted by industry, an increase with factor of 10 in mechanical performance would be required accompanied by a move away from solution based processing towards more industrial techniques. This is a major challenge given the difficulty in achieving dispersion, even in polymer solutions with low nanotube concentrations. Based on the results of this thesis, it is suggested that nanotube dispersion must be coupled with functionalisation or in-situ polymerisation to fully optimise stress transfer to the nanotube.

Another interesting point is that the vast majority of papers that report increases in polymer crystallinity, or crystalline coating of carbon nanotubes, are using semi-crystalline polymer matrices. This presents the possibility that nanotubes have the correct geometry to aid crystallisation of any semi-crystalline polymer. Table 7-1 shows the properties of the semi-crystalline polymers we have used alongside two other polymers that are routinely doped with carbon nanotubes.

Table 7-1: *A comparison of the crystalline properties of carbon nanotubes composites based on both semi-crystalline and amorphous polymers.*

Polymer	*Crystallinity*	T_g *(°C)*	T_m *(°C)*	*Reference*
PmPV	*Semi-crystalline*	Undetectable	*20-100*	[2]
PVOH	*Semi-crystalline*	*60*	*170-200*	[1]
PP	*Semi-crystalline*	*-5*	*175*	[3]
Polycarbonate	*Semi-crystalline*	*150*	*235*	[4]

7.4 Looking to the future

The next step in the development of this research should entail a comprehensive test for a nanotube loading threshold effect on the crystallinity/reinforcement of other semi-crystalline polymers. Given the range of papers previously introduced that provide some evidence for the existence of a threshold for a wide range of semi-crystalline matrices, it is possible that the threshold concept applies to all polymer/nanotube composites.

In addition to the dispersion techniques, functionalisation must be incorporated in future composites for optimum stress transfer. Work is already underway on this field through a collaboration with the Gounko group at the Chemistry Dept. at Trinity.

The relationship between crystallinity and mechanical performance has been established above. In addition to this, a study of the electrical properties corresponding to a given composite morphology would be useful to aid the design and understanding of the full functionality of the materials introduced here.

An interesting development has recently been published by Masuda et al[5] where carbon nanotubes of well-defined shapes have been fabricated by controlling the pore shape in porous alumina templates[6]. Triangular and square nanotubes have been successfully synthesised. Use of these tubes to probe nucleation of crystallinity would provide a valuable insight into the role of surface geometry in the crystallisation process. Furthermore, mechanical measurements on composites using these specifically shaped nanotubes may yield tailoring of mechanical properties as a function of filler geometry.

7.5 References

---

[1] M. Cadek, J.N. Coleman, K.P. Ryan, V. Nicolosi, G. Bister, A. Fonseca, J.B. Nagy, K. Szostak, F. Béguin, W.J. Blau; "Reinforcement of polymers with carbon nanotubes: The role of nanotube surface area", *Nanolett.* **2**, 353 (2004)

[2] K.P. Ryan, S.M. Lipson, A. Drury, M. Cadek, M. Rüther, S.M. O' Flaherty, V. Barron, B. McCarthy, H.J. Byrne, W.J. Blau, J.N. Coleman; "Carbon Nanotube Nucleated Crystallinity in a Conjugated Polymer Composite", *Chem. Phys. Lett.* **391**, 329 (2004)

[3] B.P. Grady, F. Pompeo, R.L. Shambaugh, D.E. Resasco; "Nucleation of Polypropylene Crystallization by Single-Walled Carbon Nanotubes", *J. Phys. Chem. B* **106**, 5852 (2002)

[4] W. Ding, A. Eitan, F.T. Fisher, X. Chen, D.A. Dikin, R. Andrews, L.C. Brinson, L.S. Schadler, R.S. Ruoff; "Direct observation of polymer sheathing in carbon nanotube-polycarbonate composites", *Nanolett.* **3**, 1593 (2003)

[5] H. Masuda, F. Matsumoto, K. Nishio; "Fabrication of functional devices based on highly ordered anodic porous alumina", *Electrochemistry* **6**, 389 (2004)

[6] M-K. Li, M. Lu, L-B. Kong, X-Y. Guo, H-L. Li; "The synthesis of MWNTs/SWNTs multiple phase nanowire arrays in porous anodic aluminium oxide templates", *Mat. Sci. and Eng.* **A354**, 92 (2003)

APPENDIX A: LITERATURE REVIEW

Literature related to carbon nanotubes, polymers and their composites is listed here in table form. The table is structured to allow comparison of results for identical, or very similar, materials obtained by independent research groups. Papers are allocated into one of the following groups:

- Theoretical papers and experimental papers that have investigated the mechanical, thermal or electrical properties of pristine carbon nanotubes.
- Papers that identify and characterise polymeric coating of carbon nanotubes.
- Theoretical modelling for the polymer wrapping of carbon nanotubes.
- A list of various carbon nanotube based composites and their properties.
- Properties of functionalised carbon nanotube/polymer composites.

Where the information on nanotube production was available, the following abbreviations could be used for classification:
AMWNT – Arc discharge produced multi-walled carbon nanotubes
CMWNT – CVD produced multi-walled carbon nanotubes
LMWNT – Laser ablation multi-walled carbon nanotubes
Y represents Young's modulus
S represents tensile strength

Material	Reference	Techniques	Conclusions
Simulation of nanotube mechanics	B.I. Yakobsen Phys. Rev. Lett. **76**, 2511 (1996)	Theoretical	Simulation shows that nanotube may deform elastically by up to 40% without failure.
Simulation of SWNT modulus	N. Yao J. Appl. Phys. **84**, 1939 (1998)	Theoretical	Simulation shows how modulus will be affected by torsional strain in the hexagaonal carbon lattice. Torsional strain and therefore modulus, increases with decreasing tube diameter.
AMWNT	M.M.J. Treacy Nature **381**, 678 1996	TEM	Nanotubes attached to edge of a hole in a nickel substrate - acts like clamp, other end of tubes protrude over hole and free to vibrate: blurring observed. Y calculated to be 1.8TPa

AMWNT & Nanorods	E.W. Wong Science **277**, 1971 (1997)	AFM	AFM used to measure the bending force as a function of NT displacement. Max bending strength = 28.5GPa. Avg =14.2GPa
LSWNT	Krishnan Phys. Rev. B. **58**, 14013 (1998)	TEM	Same technique as above applied to the thinner SWNT: diameter range 1-1.5nm, measured Y=1.25GPa
LSWNT/Epoxy AMWNT/Epoxy	O. Lourie J. Mater. Res. **13**, 2418 (1998)	Raman	Raman monitors cooling induced compressive deformation of NT in epoxy matrix. Concentric cylinder model for thermal stresses applied to D*-band shift: Y calculated at ~3TPa for SWNT and 2TPa for MWNT
AMWNT	P. Poncharal Science **283**, 1513 (1999)	TEM	Same technique as above. Observed that elastic bending modulus decreases sharply with increasing NT diameter.
A&CMWNT	J.P. Salvetat Adv. Mat. **11**, 161 (1999)	AFM	TEM shows different morphology of Arc and CVD MWNT. NT dropped on a membrane giving clamping effect at pore edges. Load applied to NT at center of pore producing measurable deflection. Arc tubes significantly stronger than CVD. Y=810GPa and 50GPa respectively.
CMWNT	R. Gao Phys. Rev. Lett. **85**, 622 (2000)	SEM TEM	Similar technique to Treacy et al. Bending modulus of NT determined 30GPa. Also calculated mass of individual tube at 23fg – agrees well with theoretical 17fg. Suggest sensitive balance application.
SWNT	M.F. Yu Phys. Rev. Lett. **84**, 5552 (2000)	SEM AFM	AFM used as a nanoscale tensile tester – applied load can be recorded. Average Y = 320 to 1470GPa
Thermal conductivity of single MWNT	P. Kim Phys. Rev. Lett. **87**, 215502 (2001)	SEM Microdevice	Nanotube suspended across two islands, heated by a Pt thin film resistor. Resistance changes with temp. Thermal conductivity of 3000 W/mK
Proteins/ AMWNT	F. Balavoine Ang. Chem. Int. Ed. **38**, 1912 (1999)	TEM Modelling	Proteins Streptavidin and HupR shown to helically coat MWNT
Synthetic lipids/ SWNT and MWNT	C. Richard Science **300**, 775 (2003)	TEM	Templating: Images show self organisation of SDS molecules and lipids on nanotube lattice.

DNA/SWNT	K. Keren Science **302**, 1380 (2003)	Self assembly	Streptavidin functionalised SWNT guided to "address" on DNA scaffold. Demonstrates progress from 1999 paper above.
PEI/PEG coated MWNT	A. Star Nanolett. **3**, 459 (2003)	AFM IV	FET device made using a polymer coated nanotube. The device was then biotinylated by submersion. Streptavidin binds to biotin changing device characteristic: sensor
PPV/CMWNT	H. Ago Phys. Rev. B. **61**, 2286 (2000)	PL PIA	PL blue shift with nanotubes. No significant NT absorption in visible region.
PmPV/SWNT	A. Star Macromolecules **35**, 7516 (2002)	AFM GPC	Images show the vast majority of nanotubes are isolated with only a few bundles present.
PmPV/SWNT PpyPV/SWNT	D.W. Steuerman, J. Phys. Chem. B. **106**, 3124 (2002)	UV-vis SEM Electrical	Wrapped tubes are probed electronically using microscale electrode system. Wrapped tubes exhibit photogating effect.
PS/CMWNT	D. Qian Appl. Phys. Lett. **76**, 2868 (2000)	TEM Tensile	PS modulus of 1.19GPa increases to 1.69GPa with 1wt% MWNT of 50μm avg length. If shorter tubes of length 15 μm are used then the modulus decreases marginally to 1.62GPa
PS/SWNT	H.J. Barraza Nanolett. **2**, 797 (2002)	TEM Raman	PS coating observed on nanotube bundles at 8.5wt% NT
Polycarbonate/ CMWNT	W. Ding Nanolett. **3**, 1593 (2003)	AFM SEM TEM	Images clearly show polymer sheathing around tubes.
Polycarbonate/ CMWNT	P. Pötschke Polymer **44**, 5023 (2003)	AC conductivity	Percolation threshold determined to be between 1 and 1.5%
Ordering of PE polymer chains on SWNT	C. Wei Nanolett. 4, 1949 (2004)	Theoretical	Radial distribution function calculated for chains around the carbon nanotube. Demonstrates that many polymer chains are in the vicinity of the interface.
Modelling of PPV, PmPV, PPA, PHAE, PMMA binding to SWNT	V. Lordi J. Mater. Res. **15**, 2770 (2000)	Theoretical	Find that binding energy and frictional forces play only a minor role in interface strength but helical conformations are essential.
Modelling of polyacetylene and PmPV binding to NT	J.N. Coleman Appl. Phys. Lett. **84**, 798 (2004)	Theoretical	Energetically favourable coiling angles imposed by geometric constraints are identified. This geometric constraint is shown to outweigh binding energy.

Thermal conductivity of SWNT/matrix interface	C. Nan Appl. Phys. Lett. **85**, 3549 (2004)	Theoretical	Large interfacial thermal resistance predicted between SWNT and polymer matrix.
Effect of NT length on mech. Props.	G.M. Odegard Am. Inst. of Aeronautics and Astronautics **1427,** (2002)	Theoretical	Shows that for short nanotubes, volume fraction must exceed 10% for stiffness enhancement. However for long nanotubes the stiffness v's vol fraction is linear.
$BMIBF_4$ / CSWNT (1-butyl-3-methylimidazolium tetrafluoroborate)	T. Fukushima Science **300**, 2072 2003	DSC XRD	Crystallinity of gel matrix increased with nanotubes (ΔH_c increase). Dramatic change in XRD shows ability of very low **0.5wt%** to order the matrix.
P3OT/ASWNT (poly3-octylthiophene)	L. Valentini Diamond and Related Materials **12**, 1601(2003)	DSC Electrical	**1wt%** SWNT composite has 3°C higher T_c and ΔH_c than polymer - nucleation of crystal growth. No 1st heat data shown: used to destroy thermal history. Isothermal and dynamic DSC.
PmPV/AMWNT PVA/AMWNT	B.E. Kilbride J. Appl. Phys. **92,** 4024 (2002)	Electrical	Shows percolation occurs at 0.055wt% Agrees with mechanical and crystalline properties in this thesis where very low NT concentration induces large matrix effects.
Epoxy/CMWNT	J.K.W. Sandler Polymer **44**, 5893 (2003)	Electrical	Percolation threshold determined to be 0.0025wt%.
Polyamide/ AMWNT and CMWNT	J.K.W. Sandler Polymer **45**, 2001 (2004)	SEM/XRD Raman TGA/DSC Tensile	Loading fractions up to 10wt%. Nucleation effect most prominent for the fractions lower than 5% - plateau effect after 1wt%.
Epoxy /AMWNT	O. Lourie Phys. Rev. Lett. **81**, 1638 (1998)	TEM	Imaging of nanotubes bending under stress induced during polymer drying/TEM induced heat-displacement measured and compared to theoretical predictions. Lower bound for NT compressive strength 60 GPa
PMMA/ CMWNT	Z. Jia Materials Science and Engineering **A271**, 395 (1999)	TEM FTIR Tensile	Composites of PMMA with untreated NT and tubes treated with Nitric acid. AIBN initiator used in polymerisation. Treated composites exhibit 31% increase in Tensile strength @ 7wt% NT. However reinforcement fails above this as shown by 10wt% sample.
Petroleum Pitch/SWNT	R. Andrews Appl. Phys. Lett. **75**, 1329 (1999)	Fiber spinning Tensile tests Resistivity	5wt% NT: **S +90%** **Y +150%** Conductivity +340%

PP/SWNT	B.P. Grady J. Phys. Chem. B. **106**, 5852 (2002)	DMA DSC	1.8wt% NT: **Y +15%** at Room Temp. Increase in T_c shows NT nucleate crystal growth but little difference between 0.6wt% and 1.8wt% - low loading levels effective. No increase in enthalpy of melting.
PP/MWNT	E. Assouline J. Poly. Sci. Part B: Polymer Physics **41**, 520 (2003)	DSC XRD TEM	TEM of protruding NT. Coating does not continue along length of nanotube. XRD shows crystal structure unchanged. Consistent with DSC which shows no change in melt. Isothermal DSC shows onset of crystallisation 6°C higher for composite (1wt%). ΔH_c decreases.
PP/SWNT	L. Valentini Comp. Sci. Tech. **63**, 1449 (2003)	DSC Raman	High loading of PP: 5-20wt%. T_c increase >15°C with NT but ΔH_c decreases. Implies nanotubes increase the rate of nucleation but not the volume.
PP/SWNT	A.R. Bhattacharyya Polymer **44**, 2373 (2003)	DSC XRD Raman Tensile	Isothermal DSC shows crystallisation rate increase by order of magnitude with 0.8wt% NT. T_c increases with NT as does T_m. Enthalpy increases from 93 to 100 J/g: χ +4.8%. XRD shows this increase is in the form of typical α-form PP crystals. No change in mechanical properties relative to pure PP.
PVOH/CMWNT	M.S.P. Shaffer Adv. Mat. **11**, 937 (1999)	Electrical DMA	First reports of PVOH/ NT composite.
PVOH/various CNT	M. Cadek Nanolett. **2**, 353 (2004)	TEM DSC Tensile	Best reinforcement observed for nanocyl DWNT (Y=x2). Arc MWNT observed to be less effective.
PVOH/SWNT/ surfactant	B. Vigolo, Science **290**, 1331 (2000)	Fibre spinning Tensile	Gel fibres produced by coagulation based carbon nanotube spinning method yield Y=15GPa .
PVOH/SWNT/ surfactant	A.B. Dalton Nature **423**, 703 (2003)	Fibre spinning Tensile	Gel fibres produced by coagulation based carbon nanotube spinning method yield Y=80GPa . This is twice that of Steel wire when normalised for density.
PVOH/CSWNT PVP/CSWNT PS/CSWNT	J.N. Coleman Appl. Phys. Lett. **82**, 1682 (2003)	Tensile SEM Raman DSC	Three polymers are shown to intercalate into SWNT sheets. PS composite is the best, PVP second and PVA/SWNT third with Y=6.9GPa (compared to SWNT sheet at 2.3GPa: 3 fold increase)
PVOH/PVP/ SWNT/SDS composite	X. Zhang Nanolett. **3**, 1285 (2003)	UV-vis Tensile Raman DSC	PVA ref Y=1.9GPa. Increases to 4GPa (+110%) @ 5wt% SWNT. DSC determined that composite is 13% less crystalline than PVA ref.

PVOH/SWNT	O. Probst Polymer **45**, 4437 (2004)	DSC	T_c of 0.1 & 1wt% NT studied.
PBT/CSWNT	A. Nogales Macromolecules **37**, 7669 (2004)	Conductivity WAXS SAXS	Percolation threshold at 0.2wt% WAXS: shows PBT crystals unchanged by NT. However NT peak appears at 1.6nm^{-1} as expected.
PEI/CMWNT Multilayer system	M. Olek Nanolett. **4**, 1889 (2004)	TEM SEM/AFM Tensile	Very intricate multilayer composite process. Modulus of 4.5 GPa.
MWNT/ polymer coating	H.D. Wagner Appl. Phys. Lett. **72**, 188 (1998)	TEM	Composite samples were tensile tested (Y=2GPa) and then microtomed for TEM- progressive fragmentation is observed. Calculations of the interfacial shear strength show stress transfer ability of 500MPa, an order of magnitude greater than fiber based composites.
Elastomer/ SWNT	M.D. Frogley Comp. Sci. Tech. **63**, 1647 (2003)	Tensile	200% increase in modulus with 1wt% SWNT. However ultimate tensile strength and toughness are lower.
Epoxy/ NDWNT	F.H. Gojny Comp. Sci. Tech. **64**, 2363 (2004)	TEM Tensile	Negligible increase in mechanical properties @ 0.1wt% NT (Y +0.2 Gpa)
Industrial epoxy/SWNT	M.J. Biercuk Appl. Phys. Lett. **80**, 2767 (2002)	Thermal conductivity Vickers hardness	Thermal conductivity plateau at 0.5wt%. Composites at 1wt% NT showed 125% increase in thermal conductivity at RT. Hardness increased by factor of 3.5 at 2wt% NT
Modelling of functionalised nanotubes	S. Namilae Chem. Phys. Lett. **387**, 247 (2004)	Simulation	Predicts functionalised tubes have marginally higher stiffness values. These values increase with the number of attachments.
PVOH/ PVOH functionalised ASWNT and CMWNT/ surfactant	Y. Lin Macromolecules **36**, 7199 (2003)	TEM HRTEM UV-vis NMR Raman	Images very similar to our elicarb SWNT bundles – SW not isolated HRTEM shows coating. Triton X used.
PVOH/ PVOH functionalised ASWNT and CMWNT	M.C. Paiva Carbon **42**, 2849 (2004)	Tensile Raman	PVOH ref Y=4GPa. For 5wt% funct. SWNT Y=6.2GPa. Note: Our observations suggest that values close to these can be achieved for unfunctionalised composites if PVOH is intensively dried.

Epoxy/ASWNT (functionalised)	X. Li Nanotechnology **15**, 1416 (2004)	Nanoindenter AFM SEM (fracture surfaces)	SWNT were functionalised. 5wt% composite showed 75%+ in elastic modulus and 30%+ in hardness. Fracture surface SEM showed SWNT bundles at fracture sites.
PPEI-EI/ SWNT & PPEI-EI/ MWNT (functionalised)	R. Czerw D.L. Carroll Nanolett. **1**, 423 (2001)	STM	Carboxylic acids on NT were converted to acyl chlorides. These functionalised tubes were then reacted to attach the matrix polymer. STM shows polymer coating on nanotubes.
Epoxy/MWNT (functionalised)	A. Eitan Chem. Mater. **15**, 3198 (2003)	DSC	MWNT were functionalised and reacted to attach covalently with the epoxide resin. DSC shows amorphous nature of the composite.
Cl-PP/MWNT (functionalised)	J.N. Coleman Adv. Funct. Mat. **14**, 791 (2004)	DSC Tensile SEM	Y=x3.1, S=x3.9, T=x4.4. Functionalisation modeled to extend into matrix. Acts like crystalline coating of PVOH. Reinforcing mechanism.

APPENDIX B: PUBLICATION LIST

First author journal paper

1. "Carbon Nanotube Nucleated Crystallinity in a Conjugated Polymer Composite" **K.P. Ryan**, S.M. Lipson, A. Drury, M. Cadek, M. Ruether, S.M. O' Flaherty, V. Barron, B. McCarthy, H.J. Byrne, W.J. Blau, J.N. Coleman; *Chem. Phys. Lett.* **391**, 329 (2004)

2. "Multiwalled Carbon Nanotube Nucleated Crystallisation and Reinforcement in Poly (vinyl alcohol) Composites" **K.P. Ryan**, M. Cadek, V. Nicolosi, S. Walker, M. Ruether, A. Fonseca, J.B. Nagy, W.J. Blau, J.N. Coleman; *Synth. Met.* (submitted)

Co-author journal paper

1. "High performance nanotube reinforced plastics: The mechanism of strength increase" J.N. Coleman, M. Cadek, R. Blake, V. Nicolosi, K.P. Ryan, F. Liégeois, A. Fonseca, J.B. Nagy, Y. Gounko, W.J. Blau; *Adv. Funct. Mater.* **14,** 791 (2004)

2. "Reinforcement of polymers with carbon nanotubes: The role of nanotube surface area" M. Cadek, J.N. Coleman, K.P. Ryan, V. Nicolosi, G. Bister, A. Fonseca, J.B. Nagy, K. Szostak, F. Béguin, W.J. Blau; *Nano Lett.* **4**, 353 (2004)

3. "Biomolecules as Selective Dispersants for Carbon Nanotubes" S.E. Moulton, A.I. Minett, R. Murphy, K.P. Ryan, D. McCarthy, J.N. Coleman, W.J. Blau, G.G. Wallace; *Carbon* **43**, 1879 (2005)

First author conference proceedings

1. "Photoluminence quenching and degradation studies to determine the effect of Nanotube Inclusions on Polymer Morphology in conjugated polymer-carbon nanotube composites" K.P. Ryan, S.M. Lipson, S.M. O'Flaherty, V. Barron, M. Cadek, A. Drury, H.J. Byrne, R.P. Wool, W.J. Blau, J.N. Coleman; *Conference Proceedings of SPIE OptoIreland Galway* **4876**, (2002)

Co-author conference proceedings

1. "Effect of Nanotube Inclusions on Polymer Morphology in Composite Systems" J.N. Coleman, K.P. Ryan, S.M. Lipson, A. Drury, M. Cadek, M. in het Panhuis, R.P. Wool, V. Barron, W.J. Blau; *AIP Conference Proceedings* **633**, 557 (2002)